

Correlation of the Atomic Structure and Photoluminescence of the Same Colloidal  
Quantum Dot

By

Noah Jeremiah Orfield

Dissertation

Submitted to the Faculty of the  
Graduate School of Vanderbilt University  
in partial fulfillment of the requirements

for the degree of

DOCTOR OF PHILOSOPHY

in

Chemistry

December, 2015

Nashville, Tennessee

Approved:

Date:

\_\_\_\_\_  
Sandra J. Rosenthal

\_\_\_\_\_  
Richard F. Haglund

\_\_\_\_\_  
Timothy P. Hanusa

\_\_\_\_\_  
Janet E. Macdonald

\_\_\_\_\_  
John A. McLean

*to my family*

## Acknowledgments

My first thanks go out to my parents. You taught me how to think independently. You taught me to respect others. You taught me to value knowledge, and to never waver in seeking the truth. It is your inspiration that led me to become a scientist.

To my very best friends (Josh, Sarah, and Anna)—I am constantly amazed by your accomplishments. Thank you for walking through life with me, listening to me rant and complain, and being a constant source of encouragement to me.

To Dr. Sandra Rosenthal—I am forever appreciative of the opportunity that you have provided for me to work in your lab. These last five years have simultaneously been the most mentally challenging and the most professionally rewarding of my life. The independence and freedom you gave me to pursue the results in this dissertation are mind boggling—I hope that I have demonstrated that I was deserving of the trust and patience that you exercised in mentoring me.

The members of my committee have provided invaluable expertise in providing suggestions for my research. Dr. Haglund—thank you for not yet failing me due to my lack of knowledge of physics. I have learned so much from your class, suggested reading material, and feedback during my examinations. Every one of my abstracts has been written with your guidelines in mind. Your recommendation of Fox's *Quantum Optics* led me down a path that resulted in most of the work shown in Chapter 4. Dr. Hanusa—I wish I could have had more conversations with you about science. Your categorical knowledge of and enthusiasm for inorganic chemistry is inspiring. Dr. Macdonald—watching you develop your lab and your family with such aplomb in the few years I have been at Vanderbilt has made me feel unproductive. Thank you for taking the time to serve on my committee. Dr. McLean—I always enjoy your input during exams. I suspect I will utilize your recommendations about instrumentation development and grant writing in the near future in my career.

Stunningly, my co-PI, my research mentor, my running “coach,” and the electron microscopist who took all of the pictures shown in this dissertation are one and the same person—Dr. James McBride. None of this work would have occurred without your in-depth knowledge, research acumen, and project ideas. Thank you for keeping me on track throughout my time in the Rosenthal lab. Your even-keel approach and humility despite great accomplishments is a wonderful model that I will work hard to follow. Your author-like vigor in developing each of my manuscripts has not gone unnoticed.

Dr. James G. Eberhart, your undergraduate course on Physical Chemistry inspired in me a desire to teach Chemistry at the undergraduate level, starting me on the path that led to completion of this dissertation. Your perspectives on faith and science were unique—thank you for sharing them with me.

Dr. Albert Dukes and Dr. Lloyd Davis, thank you for setting me up for success with your prior work building the fluorescence microscope. Dr. Joe Keene—I could not have picked a better person to share time in the laser lab with. The fact that you played golf with me more than once shows that you are an incredibly patient person. In the lab, your focus, attention to detail, and organizational skills kept me on my toes. You made a monumental contribution to this dissertation through your hard work maintaining the laser setup, and through your incisive comments during discussion of research. Nathaniel and Kemar, good luck in the laser lab! Kemar—training for (and completing!) the marathon with you was a great experience. Your resolve and willpower will serve you well in the Rosenthal lab. I have learned so much from your ability to ask pointed questions and carefully analyze problems that are set before you.

To the rest of the Rosenthal lab—Amy, Teresa, Ian, Danielle, Jerry, Melissa, Sarah, Scott, Talitha, Toshia, Xochitl—the lab has been a great environment to work in, largely due to your presence and the unique characteristics each of you bring to work with you every day. Thanks for putting up with me.

Emily and Oleg, it will please you both very much when I place in print that your

advice is always correct. I am not sure where I would be without the mental and emotional support that you both have offered, but I most certainly would not be writing my dissertation document. Thank you for always being willing to listen.

Bryson, Kylie, Laura, Mike, Drew, and countless others—I am so glad to have been able to spend time with you. If your friendship had been the only thing I gained while in Nashville, I would be happy.

I was very fortunate to be funded by an NSF research grant (# 1213758). I also would like to thank Vanderbilt University for a University Graduate Fellowship, and Vanderbilt Institute of Nanoscale Science and Engineering for a Research Fellowship.

Dan—much unnecessary administration would have been saved if the portion of my salary paid by the above grant numbers could have been diverted directly to The Flying Saucer. Thanks for being a “bad” influence.

Much of the research performed in Chapter 4 was done as a user at Los Alamos National Laboratory Center for Integrated Nanotechnologies. I would like to thank my sponsors, Dr. Jennifer Hollingsworth and Dr. Han Htoon, for allowing me to perform this work.

## Contents

	Page
Acknowledgments . . . . .	iii
List of Tables . . . . .	ix
List of Figures . . . . .	x
List of Abbreviations . . . . .	xii
Chapter 1 Introduction . . . . .	1
1.1 Foreword . . . . .	1
1.2 Overview . . . . .	2
1.3 Quantum dots . . . . .	4
1.3.1 Single quantum dot spectroscopy . . . . .	6
1.3.2 Time correlated single photon counting . . . . .	8
1.3.3 Quantum optics for QD characterization . . . . .	10
1.3.3.1 Photon antibunching . . . . .	10
1.3.3.2 Biexciton quantum yield measurement . . . . .	12
1.3.4 Single quantum dot high-resolution electron microscopy . . . . .	13
1.3.5 Energy-dispersive x-ray spectroscopy . . . . .	13
1.4 Instrumentation development . . . . .	14
1.4.1 Development of the single nanocrystal microscope . . . . .	14
1.4.2 Software design . . . . .	17
1.4.3 Confocal scanning of sample substrates . . . . .	17
Chapter 2 Correlation of Atomic Structure and Photoluminescence of Individual Semiconductor Nanocrystals . . . . .	21
2.1 The need for correlated interrogation of optical and structural properties of single colloidal quantum dots . . . . .	21
2.2 Previous correlation attempts by other groups . . . . .	25
2.3 Experimental methods . . . . .	26
2.3.1 Sample preparation . . . . .	26
2.3.2 Optical microscopy . . . . .	26
2.3.3 Electron microscopy . . . . .	28
2.3.4 Data analysis . . . . .	29
2.4 Selecting a suitable substrate for correlated photoluminescence microscopy and electron microscopy . . . . .	29

2.5	Needle in the hay: unambiguous correlation of photoluminescence and fine atomic structure of the same colloidal quantum dot . . . . .	33
2.6	Conclusions . . . . .	38
Chapter 3 Visualizing Nonradiative Internal and Surface Defects: The Role of Stacking Faults and Anomalous Shell Epitaxies in Nonradiative Recombination . . . . .		42
3.1	Choice of quantum dot system to study . . . . .	42
3.2	“On”-fraction heterogeneity in commercially available CdSe/CdS core/shell quantum dots . . . . .	44
3.3	The good: Ideal quantum dot structures in the high on-fraction population . . . . .	45
3.4	The bad: Stacking faults and visible surface irregularity act as nonradiative recombination centers . . . . .	47
3.5	... And the ugly: Determination of the crystal structure of single nonradiative quantum dots . . . . .	51
3.6	Other results . . . . .	53
3.6.1	Length vs. on-fraction . . . . .	53
3.6.2	Probability distributions of “on” and “off” times . . . . .	54
3.6.3	Statistical certainty of subpopulation assignment . . . . .	54
3.7	Conclusions . . . . .	55
Chapter 4 Nanocrystal-to-Nanocrystal Quantum Yield Heterogeneity and the Lack of a “Dark” Fraction in Nonblinking “Giant” Quantum Dots . . . . .		58
4.1	The need for complete correlation of single colloidal quantum dot atomic structure, spatially resolved chemical composition, and single-photon photoluminescence behavior . . . . .	59
4.2	Correlation of atomic structure and photoluminescence for g-QDs . . . . .	63
4.3	Time-correlated single photon counting for improved description of single quantum dot photoluminescence . . . . .	63
4.4	Single quantum dot energy dispersive x-ray spectroscopy . . . . .	64
4.5	Determination of single quantum dot quantum yields via high angle annular dark field imaging . . . . .	65
4.6	Quantum yield heterogeneity and the lack of a “dark” fraction . . . . .	66
4.7	Single quantum dot quantum yield “pinning” . . . . .	69
4.8	Charging as an explanation for variation of single quantum dot quantum yield . . . . .	72
4.9	Implications for measurement of biexciton quantum yield . . . . .	78
4.10	Entanglement in a “quantum heart” . . . . .	80
4.11	Conclusions . . . . .	82
4.12	Experimental methods . . . . .	83
4.12.1	Nanocrystal synthesis . . . . .	83
4.12.2	Nonblinking fraction of g-QDs . . . . .	84
4.12.3	Derivation of the two-state charging model . . . . .	84
4.12.4	Comparison of a spherical QD approximation with volume from HAADF intensity . . . . .	87

4.12.5 Physical and optical data of studied g-QDs . . . . .	87
4.12.6 Sample preparation . . . . .	87
4.12.7 Fitting of $g^{(2)}$ traces for determination of center peak to side peak ratio . . . . .	87
Chapter 5 Conclusions . . . . .	91
5.1 Overall conclusions . . . . .	91
5.1.1 Limitations of the correlation . . . . .	92
5.2 Future work . . . . .	94
5.2.1 QD development . . . . .	94
5.2.2 Non-QD development . . . . .	94
5.2.3 Ramifications of this work for colloidal quantum dot research . . . . .	94
Appendices . . . . .	96
Appendix A Structures and Photoluminescence of Commercially Available CdSe/CdS Core/Shell Quantum Dots . . . . .	96
Appendix B Full Structural and Optical Data for Studied “Giant” CdSe/CdS Core/Shell Nanocrystal Quantum Dots . . . . .	105
Appendix C Measurement of Ensemble Quantum Dot Lifetime with the Rosenthal Lab Single Quantum Dot Microscope . . . . .	130
Bibliography . . . . .	133

## List of Tables

Table	Page
1.1 Measurable correlated physical and optical properties of nanostructures . . .	3
1.2 Applications of quantum dots . . . . .	5
1.3 Commercially available quantum dots . . . . .	5
2.1 Relationship between single QD PL behavior and desired application . . . .	24
4.1 Comparison of calculation of sphere volume with calculation of volume from HAADF integrated intensity . . . . .	88
4.2 Physical and optical data of studied g-QDs . . . . .	89

## List of Figures

Figure	Page
1.1 Time Correlated Single Photon Counting Theory . . . . .	9
1.2 Photon antibunching indicates the presence of a single emitter . . . . .	11
1.3 Single Nanocrystal Fluorescence Microscope . . . . .	15
1.4 Photograph of Single Nanocrystal Fluorescence Microscope . . . . .	15
1.5 Simulated profile of the confocal collection area . . . . .	18
1.6 Measured profile of the excitation beam . . . . .	19
1.7 Confocal raster scan of single QDs . . . . .	19
1.8 Intensity vs time trace for a single QD . . . . .	20
2.1 Preparation of TEM support films for correlation . . . . .	27
2.2 Geometry for fluorescence imaging of QDs on a TEM support film . . . . .	28
2.3 Fluorescence of single QDs on a Si <sub>3</sub> N <sub>4</sub> TEM support film . . . . .	31
2.4 Photoluminescence intensity vs time trace for a single QD on a Si <sub>3</sub> N <sub>4</sub> substrate	31
2.5 Use of Si <sub>3</sub> N <sub>4</sub> as a substrate for electron microscopy . . . . .	33
2.6 The strategy for correlation of single QD photoluminescence behavior with atomic structure . . . . .	34
2.7 Correlation of optical and electron microscopy . . . . .	35
2.8 Fluorescence imaging of single QDs on a 40 nm thick SiO <sub>2</sub> substrate . . . . .	36
2.9 Support film configuration and use of PS as fiducial markers . . . . .	38
2.10 The first demonstration of unambiguous correlation of optical and electron microscopy for QDs . . . . .	39
2.11 Structures of QDs shown in the wide-field images in Figure 2.10 . . . . .	40
3.1 Correlated fluorescence and structural data for individual QDs . . . . .	43
3.2 Heterogeneity within the core/shell nanocrystal ensemble . . . . .	44
3.3 Structures of suppressed blinking QDs . . . . .	46
3.4 Stacking Faults Inhibit Single QD PL . . . . .	48
3.5 Characteristic defects for QDs with a low on-fraction . . . . .	50
3.6 Structures of nonradiative QDs . . . . .	52
3.7 Length vs on-fraction . . . . .	54
3.8 Morphologies and orientations of QDs in the high and low on-fraction pop- ulations . . . . .	56
4.1 Acquisition of optical, structural and chemical data for a single colloidal quantum dot . . . . .	61
4.2 Correlation of confocal raster scanned fluorescence and atomic structure for individual quantum dots . . . . .	64
4.3 Quantum yield heterogeneity among single nonblinking QDs . . . . .	67
4.4 Correlation of wide-field fluorescence and atomic structure . . . . .	68
4.5 Optical vs physical parameters for studied quantum dots . . . . .	70
4.6 Quantum yield “pinning” in nonblinking QDs . . . . .	71

4.7	Further analysis of the influence of charging on single-QD quantum yield . . .	73
4.8	$g^{(2)}$ fits for the QDs shown in Figure 4.7 . . . . .	74
4.9	Mechanism to describe QY heterogeneity . . . . .	76
4.10	Modeling the relationship between quantum dot quantum yield and lifetime . . . . .	77
4.11	The use of single-QD quantum yield to determine BXQY . . . . .	79
4.12	Quantum optical signature of coupling between artificial atoms in a colloidal QD heterostructure . . . . .	81
4.13	Nonblinking fraction of g-QD sample . . . . .	84
A.1	An illustration of the method used to locate and interrogate single QDs on the 8 nm SiO <sub>2</sub> support film . . . . .	98
A.2	Acquisition of Z-STEM images for the remaining ROIs shown in (A) . . . . .	99
A.3	High-resolution Z-STEM images for all of the QDs used for this study . . . . .	104
C.1	Fluorescence decay lifetime of CdSe/CdS core/shell nanorods . . . . .	132

## List of Abbreviations

AFM	Atomic Force Microscopy
BXQY	Biexciton Quantum Yield
CCD	Charge Coupled Device
CQD	Coupled Quantum Dot
EDS	Energy-dispersive X-ray Spectroscopy
FRET	Förster Resonant Energy Transfer
g-QD	“Giant” Quantum Dot
HAADF	High Angle Annular Dark Field
HOFP	High On-fraction Population
HT	Hole Trap
LED	Light-emitting Diode
LOFP	Low On-fraction Population
OD	Octadecane
ODE	1-Octadecene
OLAC	Oleic Acid
PDL	Pulsed Diode Laser
PI	Photoluminescence Intermittency
PL	Photoluminescence
PLQY	Photoluminescence Quantum Yield
PMMA	Poly(methyl methacrylate)
PS	Polystyrene Latex Spheres
QD	Quantum Dot
ROI	Region of Interest
SILAR	Successive Ionic Layer Adsorption and Reaction
SPAD	Single Photon Avalanche Diode
STEM	Scanning Transmission Electron Microscopy

SXQY	Single Exciton Quantum Yield
TCSPC	Time Correlated Single-Photon Counting
TEM	Transmission Electron Microscopy
TOP	Trioctylphosphine
TOPO	Trioctylphosphine Oxide
Z-STEM	Atomic Number Contrast Scanning Transmission Electron Microscopy

## Chapter 1

### Introduction

#### 1.1 Foreword

Miniaturization has arguably been the key theme of technological culture in the past two decades. Since the advent of and ubiquitization of the personal computer—a miniature device in its own right—the drive to continue reducing the size of personal electronic devices has driven demand in the consumer electronics industry. When you look around, it is difficult not to see the manifestation of this drive: ultrathin laptop computers, televisions, and highly advanced cell phones continue to become sleeker, lighter, and more powerful.

Even so, there remains a desire to develop devices that are paper-thin, flexible, and more energy-efficient. Creation of such devices will require miniaturization to the single- or few-atom scale, however. Light-emitting and sensing films need to be created on the few-nanometer thickness scales; transistors, switches and electric circuitry need to be fabricated on a single atom (or single “artificial atom”) scale.

Colloidal quantum dots have already been implemented into such devices in a proof-of-principle manner, and their excellent optical properties and robust physical structure have led to commercial availability in sensors and televisions. However, it is necessary to continue to continue fervent research into obtaining complete control over the physical properties, optical properties, ensemble charge separation, and exciton recombination properties of these revolutionary systems.

This work represents a small contribution to this worldwide academic and industrial research and development effort.

## 1.2 Overview

Characterization of synthesized compounds has long played a crucial role in development of new chemical processes. It is only *via* physical characterization that the synthetic chemist can receive feedback and learn how to modify reaction parameters to optimize syntheses. When considering syntheses of organic molecules, for example, it is standard to use a selected chromatographic method (gas-phase chromatography, liquid chromatography, etc.) to isolate a product, and also to use various optical and physical characterization methods (*e.g.* infrared spectroscopy, nuclear magnetic resonance spectroscopy, mass spectrometry) to understand the identity and purity of the products of a reaction. This information then serves as a vital part of a feedback loop to optimize and inform future syntheses.

With the advent of a “new chemistry”—synthesis of nanometer sized metal and semiconductor products—there are many added challenges to the design, synthesis, and characterization of samples. On the one hand, synthesis of an organic molecule with a chemical structure that is, by definition, rigidly defined may result in a product mixture that consists of a few byproducts and—for larger biologically relevant molecules—a racemic mixture of chiral products. A pyrolytic synthesis of nanostructures, however, results in a multitudinous array of complex “molecular” architectures. When considering a colloiddally synthesized quantum dot (QD)\*—a nanometer-sized crystal of semiconductor material containing hundreds to hundreds of thousands of atoms—the number of possible structural configurations of the atoms composing the quantum dot is perhaps even as large as the number of QDs synthesized in a single colloidal batch! This phenomenon is illustrated very well in the absorption and emission properties of colloidal QDs. Early characterization of QD batches *via* ultraviolet/visible spectrophotometry and photoluminescence emission spectroscopy demonstrated an innate broadening of the linewidth of ensemble QD emission

---

\*The terminology “quantum dot” (QD) is frequently used to refer to a number of different systems, including epitaxial quantum dots, crystal phase quantum dots, and quantum dots derived *via* colloidal synthesis. In this document, unless specified otherwise, this nomenclature is used to refer to the latter system.

Table 1.1: Measurable correlated physical and optical properties of nanostructures

<b>Nanostructure</b>	<b>Desired Application</b>	<b>Structure-dependent optical property</b>
Quantum dots	LEDs	Photoluminescence linewidth
Semiconductor nanorods	Photocatalysis	Charge separation
Gold nanocrystals	Photothermal heating	Plasmon resonance

spectra; this effect, termed “inhomogeneous broadening” is due to the variety of shapes and sizes of QDs present in a synthesized batch.<sup>1</sup>

While characterization techniques that measure the properties of millions of nanostructures at a time are highly valuable, it is important to remain aware of the structural heterogeneity that is present in nanostructures and to understand its effects on expressed physical properties. Nanostructures are typically designed for a specific function—quantum dots are being used in light-emitting devices and televisions; nanorods hold great promise for use in photocatalytic water-splitting; noble metal nanocrystals are used for photothermal applications. For each of these three examples, the desired outcome is dependent on an optical property: photoluminescence linewidths, charge separation/transfer, and plasmon resonance, respectively, as shown in Table 1.1. Further, each of these optical properties are highly dependent on the array of structures present in the ensemble sample.

As the field of nanochemistry has developed, it has become necessary to examine not only the resultant properties of millions of nanocrystals measured simultaneously, but also to visualize the properties of individual nanostructures. The increasing ubiquity of electron microscopes allowed many chemists to begin determining the atomic and crystal structures of single QDs within a batch.<sup>2</sup> This provided a great glimpse into the nature and mechanism of colloidal synthesis. Furthermore, the advent and refinement of single molecule microscopy techniques has allowed determination of the optical properties of single nanostructures.<sup>3,4</sup> It is now possible to directly measure the photoluminescence spectrum, Raman peak shift,<sup>5</sup> plasmon resonance,<sup>6</sup> and even the fine absorption spectrum for single

nanocrystals.<sup>7,8</sup>

Despite these advances, the most often-used method for single-particle characterization is uncorrelated: the structural properties of a few hundred nanocrystals are determined and, subsequently, the optical properties of a few dozen single nanocrystals are determined. Although guesses at the correlation between the observed optical and structural behaviors are well-informed, there remains a need for a characterization technique that melds the utility of these two separate techniques—high-resolution electron microscopy and single particle optical microscopy—into a simple, unambiguous, reproducible single-particle characterization methodology. The work presented in this dissertation demonstrates the development of a technique which meets these demands of the field.

The correlation technique that is demonstrated here is used for characterization of colloidal quantum dot samples, but the same method could be used to understand the interplay of optical and physical properties of a plethora of nanostructures. In this work, it is shown that using a combination of single particle fluorescence spectroscopy and electron microscopy for interrogation of the very same QD reveals a great deal of previously inaccessible information. What follows is an overview of the developed technique and its application to two problems which have been plaguing the colloidal quantum dot field. The results would not have been possible without atomic structure-photoluminescence correlation. Finally, concluding remarks address the possibility of applying this correlation technique to other known problems in the field of nanochemistry.<sup>9</sup>

### 1.3 Quantum dots

With the combined experimental work of Louis Brus and theoretical work of Alexander Efros in the 1980s, semiconductor nanocrystals with quantum-confined excitons were introduced into the scientific conscious.<sup>10</sup> Concomitant with this seminal work was the introduction of the idea of quantum size-effects into the field of chemistry—quantum confinement had previously been the realm of solid-state semiconductor physics, but structures

Table 1.2: Applications of quantum dots

<b>Leveraged property</b>	<b>Application</b>	<b>Group</b>
Photoluminescence	Light-Emitting Diodes	Bawendi <sup>12</sup>
	Biological Labeling	Rosenthal <sup>11</sup>
	QD Lasers	Klimov <sup>13</sup>
Absorption	Solar Concentrators	Malik <sup>14–16</sup>
	IR Sensors	Sargent <sup>17</sup>
	Multiplexing Spectrometers	Bawendi <sup>18</sup>
Charge separation	Photovoltaics	Sargent <sup>19</sup>

Table 1.3: Commercially available quantum dots

<b>Product</b>	<b>QD Application</b>	<b>Company</b>
Biological Labels	Imaging	LifeTech
Television	Color rendering/diffuser	QDVision
Tablet	Diffuser	Nanosys
Camera detector	Light collection	InVisage
LEDs	Light emission	QDVision / Nanosys

expressing this property could now be derived on a large scale in solution. The development of pyrolytic syntheses for creation of nanocrystals in the 0D confinement regime was accompanied by the promise of use of these “quantum dots” (QDs) as solution-processable precursors for a variety of applications. Additionally, the remarkably large extinction coefficient and incredible photostability of QDs foreshadowed their capability to replace organic fluorescent dyes in many biological labeling applications.<sup>11</sup> In the three decades since QDs were introduced to a broad scientific audience, there has been an explosion of research into and application of these unique fluorophores, both academic and industrial. A summary of some of the most important discovered applications is presented in Table 1.2.

### 1.3.1 Single quantum dot spectroscopy

Due to the inherent inhomogeneity of size, shape, and structure of colloidal QDs, it became necessary to image the optical properties of one QD at a time. The development of single-molecule fluorescence spectroscopy made this goal achievable by the Bawendi group in 1996.<sup>20</sup> In this work, it was first reported that single quantum dot fluorescence consists of discrete “on” (emissive) and “off” (non-emissive) states, which occur on timescales of approximately 0.5 seconds. When imaging single quantum dots, it was discovered that single quantum dots switched between binary states—a fluorescence “blinking” process now known as photoluminescence intermittency (PI). The relationship between the probability distribution of the length of “on” as well as “off” events with respect to time has been shown to obey a power law distribution which is temperature independent, but does depend on factors such as excitation intensity, excitation wavelength and, in the case of core / shell nanocrystals, shell composition and thickness.<sup>9,21–25</sup>

One of the first models that purported to explain blinking behavior was the charging-blinking model, which assumes that ionized nanocrystals will cease to emit photons due to interference and competition with radiative exciton recombination within QDs.<sup>9,20,25,26</sup> A number of alternative theories regarding the source of PI have been proposed since Bawendi’s foundational research. The inability of the charging-blinking model to adequately describe observed PI is well documented;<sup>27,28</sup> another theory suggests generation of multiple excitons in single nanocrystals as the source of PI.<sup>29–33</sup> Additional studies pinpoint multiple recombination centers within the nanocrystals as the source of this phenomenon.<sup>34–39</sup> More recently, Galland *et al* have shown that QD blinking is actually an expression of two types of blinking—“A” type, which arises due to charging and discharging of the QD surface, and “B” type, which is due to charge fluctuations among the surface sites of the QD.<sup>40</sup> Even this explanation, however, has recently been challenged with findings that indicate that surface oxidation must be taken into account when considering single QD PL spectra.<sup>41</sup>

In addition to PI, single QDs show many other unique optical properties on the single QD scale. For example, it is well known that the wavelength of emission of a QD is determined by its size. This results in the “inhomogeneous broadening” of the ensemble PL linewidth. However, in addition to this heterogeneity, spectral diffusion of the emission of single QDs is a well-known phenomenon that arises due to the fluctuation of charge on or around a single QD.<sup>42,43</sup> Even at low temperatures, the emission wavelength of a single QD may vary by several meV. This problem makes implementation of QDs into devices such as optical switches and single-photon routers extremely difficult despite the desirable single-photon emission from QDs, as these applications necessitate a single, steady emission wavelength.<sup>44</sup>

An extreme example of the sensitivity of single QDs to their surroundings is frequently encountered in single molecule fluorescence studies—a substantial fraction of single QDs are permanently nonradiative, or “dark.”<sup>45</sup> This is in addition to the fraction of QDs that are observed to be in the “off” state (due to PI) at any given arbitrary observation time. This fraction of “dark” QDs is deleterious to not only single QD applications, but also results in reduced PLQY on the ensemble level, reducing the possible impact of QD implementation into LEDs and other devices.

Although single QD fluorescence has been well studied since its discovery, correlation of single nanocrystal optical spectroscopy with structural information from that same QD has not been effectively demonstrated. Sequential single nanoparticle spectroscopy and atomic resolution scanning transmission electron microscopy measurements on core/shell nanocrystals of varying composition and shell thickness has added an additional component which can be examined when investigating the mechanism of expressed fluorescence behavior of single QDs. In turn, this correlation has provided a more comprehensive understanding of the mechanisms of observed photophysical behavior of QDs.

### 1.3.2 Time correlated single photon counting

To provide the time resolution necessary for collection of single-nanocrystal emission after excitation by a pulsed source, Time Correlated Single-Photon Counting (TCSPC) was added to the single nanocrystal microscope. This technique measures the time between excitation of a quantum dot and subsequent emission of single photons. Over a long period of time, many such delay times are calculated for the species being examined. These delay times can then be histogrammed to provide an accurate approximation of the lifetime of the fluorophore(s). Absolute measurement of ensemble lifetime in response to continuous wave excitation would require a dynamic response of  $\approx 20$  ps, a value uncharacteristic of most common detectors. Rather than take this approach, use of single photon detectors allows very sensitive and precise determination of emission dynamics on few-nanosecond timescales.

TCSPC uses a reference photodiode to characterize the real-time repetition rate of the excitation source. Single photon events are then detected by single photon avalanche photodiodes (SPADs) at some time  $t_1$  after the counting board detects the sync pulse. The “pump” power of the excitation beam is kept at a sufficiently low power such that the photon emission rate from the fluorophore is  $\approx 1\%$  of the pulse frequency (*e.g.* 2.5 kHz for a 250 kHz excitation repetition rate).<sup>†</sup> As a result, a large number of pulse cycles pass between detection of single emitted photons. Single photon counts are converted to a TTL pulse by the SPADs that is then read by the counting board (PicoHarp 300). The pulse that is generated due to single photon detection at a SPAD occurs at some time  $t_2$  after the sync pulse (the pulse generated upon photoexcitation of the reference photodiode). The PicoHarp 300 records each photon event and marks it with an absolute time relative to the last sync pulse (delay time).

---

<sup>†</sup>The repetition rate of the excitation source should be very carefully chosen; if it is improper the lifetime histogram will be an inaccurate reflection of the actual emission lifetime of the fluorophore. It is important to ensure that the histogram count rate at a time delay approaching the pulse spacing is  $\ll 1\%$  of the maximum histogrammed count rate. For most colloidal CdSe nanocrystals, this results in a need for pulse spacing of  $\geq 400$  ns.

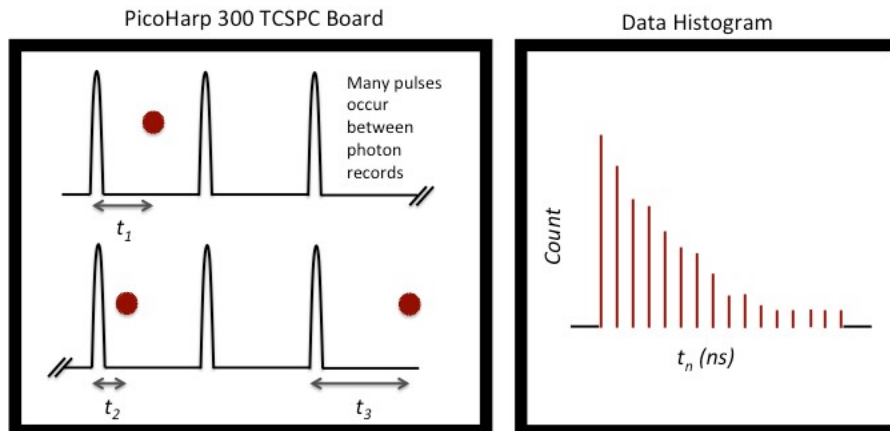


Figure 1.1: **Time Correlated Single Photon Counting Theory.** *Left*– Excitation pulses are sensed by a trigger diode and recorded by the PicoHarp 300 module to determine the repetition rate of the excitation beam. When a photon is emitted by a quantum dot, the arrival time of that photon is recorded by one of the single photon avalanche diodes measuring the fluorescence emission. Both the absolute arrival time (relative to the start of the experiment) as well as the relative arrival time (relative to the most recent excitation pulse) are recorded in the generated data file. *Right*– The delay time for each photon is recorded and used to generate a histogram of the lifetimes of single photons. This histogram can be used to determine the fluorescence lifetime of the interrogated fluorophore.

Over a significant amount of time (usually seconds to minutes) collection of a large amount of single photon records allows creation of a histogram of the measured delay times; this histogram can be analyzed to determine the lifetime of the interrogated fluorophore. The amount of time needed to collect sufficient counts to create a lifetime histogram is dependent on both the lifetime of the fluorophore and the count rate of emission. The process of collecting photons and creating lifetime histograms is illustrated in Figure 1.1.<sup>‡</sup>

<sup>‡</sup>For a comprehensive review of theory and instrumentation for TCSPC, see the PicoQuant PicoHarp 300 User Manual and Technical Data.

### 1.3.3 Quantum optics for QD characterization

#### 1.3.3.1 Photon antibunching

As the number of studies of single QD photoluminescence began to grow, it became apparent that there was a need to prove whether the QD being studied was, in fact, a single QD or an aggregate of two or more QDs. Before inorganic shelling became commonplace in procedures for QD synthesis, “off” times of single QDs could last for periods of tens of seconds to minutes—making it difficult to determine the number of QDs solely from the intensity levels of emission.<sup>20,46</sup> In 2000, Michler *et al* used photon antibunching to show that single colloidal quantum dots emit single photons at a time.<sup>47</sup> This discovery indicated that QDs could potentially be used to generate single photons on demand; this is a crucial condition for use of QDs in quantum information and quantum communication devices. Further, it was learned that discovering the key spectroscopic signature of single photon emission—“photon antibunching”—*via* Hanbury Brown & Twiss interferometry<sup>48</sup> indicates that only one QD is being investigated.

Hanbury Brown & Twiss interferometry relies on the concept that when a single emitter emits one photon at a time, the emitted photon may only proceed to one of the detectors on the other side of a 50/50 beamsplitter. Over time, a correlation of counts between the two detectors will show that, for pulsed excitation, the fluorescence counts from a single emitter are not correlated at a time delay  $\tau = 0$ . This can be described by the second order correlation function of photon counts between the two detectors:<sup>44</sup>

$$g^{(2)}(\tau) = \frac{\langle n_1(t)n_2(t+\tau) \rangle}{\langle n_1(t) \rangle \langle n_2(t+\tau) \rangle}$$

where  $n_i(t)$  is the photon count at detector  $i$  at time  $t$  and  $\tau$  is the time delay between the two SPADS. For a single emitter, as  $\tau$  approaches zero, if

$$n_1(t) \neq 0$$

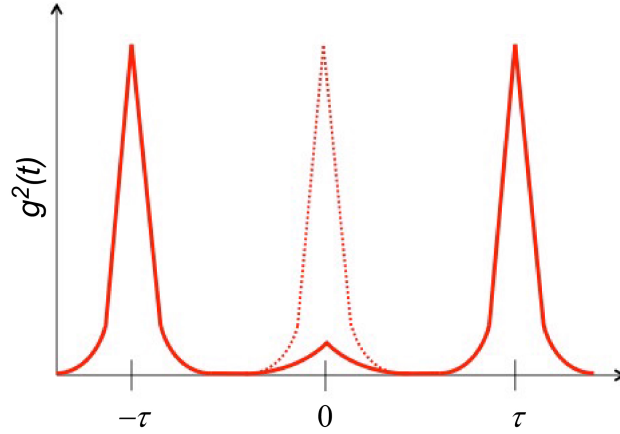


Figure 1.2: **Photon antibunching indicates the presence of a single emitter.** When a single photon emitter is being imaged, the center peak at  $\tau = 0$  has intensity close to 0. If multiple photons are being emitted for every excitation pulse, the center peak is  $> 0$ , as shown by the dashed red line. Negative time delay is possible between the two detectors because of an electrical delay which is implemented between one of the detectors and the correlation card.<sup>44</sup>

then

$$n_2(t + \tau) \approx n_2(t) = 0$$

Conversely, if

$$n_2(t + \tau) \neq 0$$

then

$$n_1(t) = 0$$

Essentially, if a single photon is emitted as a result of excitation by a single laser pulse, a single photon emitter is incapable of generating a second photon that could be registered simultaneously on a second detector. This leads to a lack of correlation counts between the two detectors at zero time delay. Therefore, as the time delay  $\tau$  approaches zero, the second order correlation result also approaches zero. This results in a time trace similar to that seen in Figure 1.2, and is used to distinguish single nanocrystals from multiple fluorescent nanocrystals.<sup>49,50</sup>

### 1.3.3.2 Biexciton quantum yield measurement

Over time, as QD syntheses became more sophisticated and resulted in PLQYs  $>80\%$ , it became apparent that the strict requirement of complete antibunching (integration of the center peak of  $g^{(2)}=0$ ) was not achievable when performing single QD spectroscopy studies. In 2012, it was shown by the Bawendi group that, even for single emitters, the ratio of center peak to side peaks in the  $g^{(2)}$  spectrum tends to be some nonzero, positive value.<sup>32</sup> This phenomenon occurs due to the high probability of formation of a biexciton within a single QD. These biexcitons typically decay nonradiatively, but some fraction of generated biexcitons undergo radiative decay. If a biexciton radiatively recombines, it produces two photons in extremely rapid succession—biexciton radiative lifetimes are typically on the order of a few nanoseconds or shorter. This effect manifests in a count at  $\tau = 0$  in the  $g^{(2)}$  spectrum, even though a single emitter is being studied.

Further, it has been shown that, in the event a single emitter was being studied, the biexciton quantum yield (BXQY) could be equated to the ratio of the center peak to any of the side peaks of the  $g^{(2)}$  trace. In QDs, Auger recombination of multiexciton states is known to lead to reduced PLQY.<sup>51</sup> Therefore, subsequent to these initial studies, measurement of BXQY became a standard means of understanding the level of Auger suppression in QD syntheses, particularly those of the commonly encountered “workhorse” heterostructures involving CdSe cores. Utilization of this characterization led to one of the key findings with regard to BXQY: there is a high level of heterogeneity in measured values of BXQY for QDs from the same sample.<sup>29</sup> The explanation for this heterogeneity was speculated to be associated with surface roughness or presence of crystalline defects in the QDs. However, a structural correlation with BXQY was still needed to confirm these hypotheses. Exploration to determine structurally-correlated BXQY was the primary motivation for the work in Chapter 4.

#### 1.3.4 Single quantum dot high-resolution electron microscopy

In the development of QDs, electron microscopy has been one of the most useful tools for analysis of the nature of synthesized QD samples. Simple transmission electron microscopy experiments are still standard for determination of the size distribution of QDs, while these measurements also provide vital information about the shape and crystal structure of single QDs within the ensemble. In 2004, the use of atomic number contrast scanning transmission electron microscopy (Z-STEM) aided in visualization of atom-resolved images of CdSe/CdS core/shell QDs.<sup>52</sup> The implementation of Z-STEM allowed a much deeper understanding of the nature of shell epitaxy on colloidal core/shell QDs. This technique has also been used to investigate termination of crystal faces on the surface of QDs, as well as allowing visualization of defects such as zinc-blende stacking faults within wurtzite heterostructures.<sup>53</sup>

#### 1.3.5 Energy-dispersive x-ray spectroscopy

Although Z-STEM is highly useful, and allows a qualitative determination of the location of the core and shell regions of a core/shell QD, the exact location of the core cannot be determined with great precision from Z-STEM micrographs. For this measurement, it becomes necessary to implement a different characterization method. An ideal method is energy-dispersive x-ray spectroscopy (EDS), which can be used to determine the chemical composition of the investigated sample, and provides useful information about regions of different chemical composition within the same nanostructure.

Vanderbilt University's acquisition of a FEI Tecnai Osiris scanning transmission electron microscope with ChemiSTEM<sup>TM</sup> technology greatly facilitated the measurement of single QD chemical composition. In the past, acquisition of elemental maps QDs would take minutes to acquire, greatly increasing the probability that the heterostructure of interest would be significantly damaged due to heating or excessive build up of charge. The

Super-X EDS silicon drift detectors in the Osiris allow for a much higher ( $\sim 50\times$  greater) signal from interrogated samples, providing a means by which high-resolution elemental mapping can be performed long before noticeable structural damage occurs to the QD sample.

## 1.4 Instrumentation development

### 1.4.1 Development of the single nanocrystal microscope

Investigation of fluorescence intermittency and related processes in single nanocrystals requires an instrument which provides single nanocrystal resolution, fluorescent lifetime measurement capability, and time resolution on an extremely short (picosecond) time scale. A diagram of the experimental setup, which was modified from that reported by Dukes *et al.*,<sup>54</sup> is shown in Figure 1.3, while a photograph of the setup is shown in Figure 1.4.

A neodymium-doped yttrium orthovanadate ( $\text{Nd:YVO}_4$ ) continuous-wave laser (Coherent<sup>TM</sup> Verdi, 532 nm, 18W) pumps a titanium sapphire ( $\text{Ti:Al}_2\text{O}_3$ ) oscillator (Coherent<sup>TM</sup> Mira, 800 nm) with a repetition rate of 76 MHz. This beam is frequency doubled in an angle-tuned beta barium borate (1 mm  $\beta$ -BBO, Altos Photonics) nonlinear mixing crystal. The result is an excitation beam with a wavelength of 400 nm, pulse width of  $<200$  fs, and a temporal pulse separation of 13.2 nanoseconds.

Alternatively, the beam from the Coherent Mira is used to pump a Coherent RegA 900 titanium sapphire ( $\text{Ti:Al}_2\text{O}_3$ ) regenerative amplifier; the energy of the 800 nm pulse from the RegA is amplified by a factor of  $\sim 10^3$ , and the repetition rate of the pulse is lowered to 250 MHz. This full setup has been illustrated previously.<sup>55</sup> The resultant beam is frequency doubled using a  $\beta$ -BBO crystal to produce a 400 nm excitation beam that can be used in the place of the beam generated after the Mira. This results in an interpulse spacing that is much more optimal for measuring QD lifetimes, as a typical decay time for colloidal QDs is on the order of several hundred nanoseconds—a pulse occurrence of once every 4

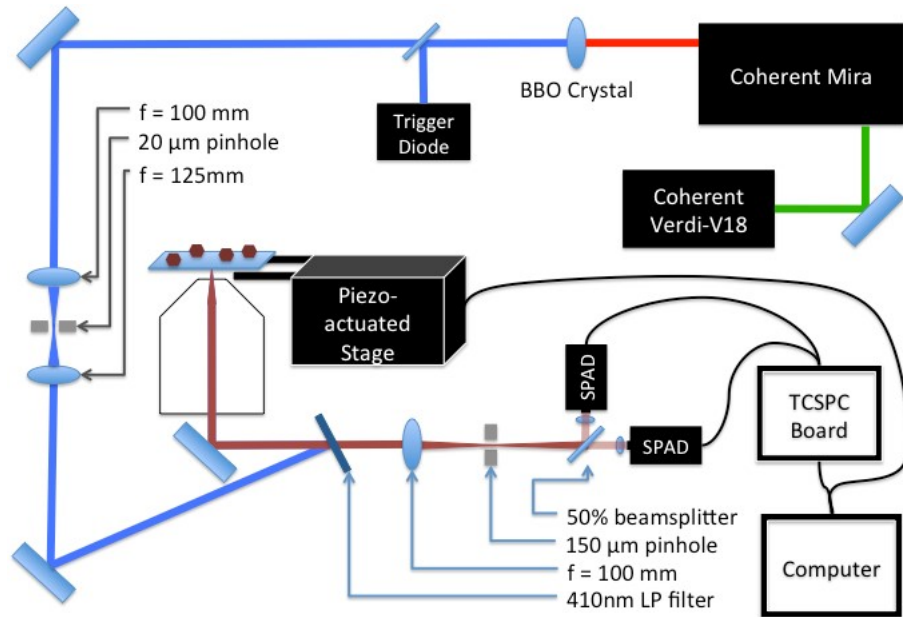


Figure 1.3: **Single Nanocrystal Fluorescence Microscope.** See text for full description of optical components. A series of lasers produces a 400 nm excitation pulse that is used to set the repetition rate at a trigger diode. The excitation beam is directed into a backfilled objective that provides illumination of QD samples on a cantilevered substrate with XYZ-positions controlled by a piezo-actuated stage. Emission of the QDs is collected through the same objective, filtered from excitation light with a 410 nm long pass filter, and imaged confocally onto a set of single photon avalanched diodes (SPADs) in a Hanbury Brown & Twiss geometry to allow for measurement of single QD antibunching.

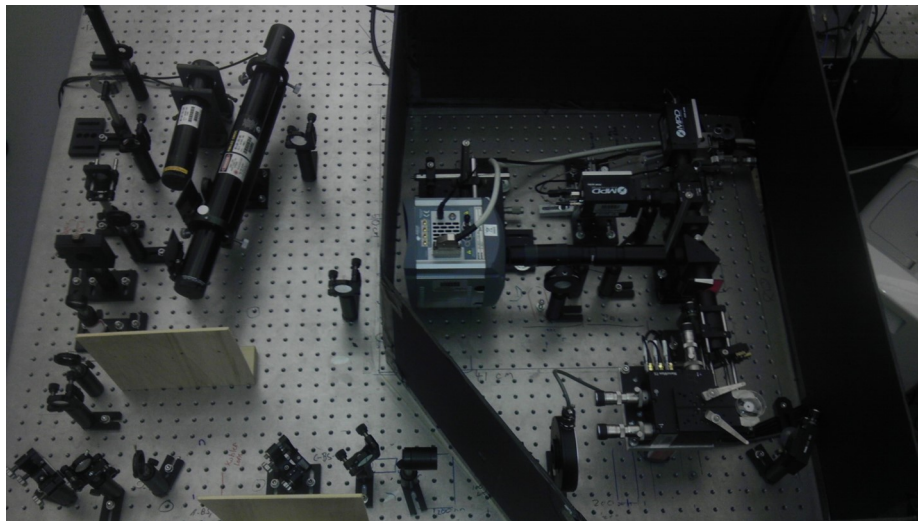


Figure 1.4: **Photograph of the Single Nanocrystal Fluorescence Microscope.** This picture shows the beam path entering the objective, the cantilevered piezostage, and the two SPADs in a Hanbury Brown & Twiss alignment. Also shown is the optional collection pathway to the CCD camera, which is used for wide-field fluorescence collection and bright-field microscopy.

$\mu\text{s}$  therefore allows the QDs to decay fully between excitation pulses.

The 400 nm excitation beam is focused through a 20  $\mu\text{m}$  pinhole and recollimated before being reflected from a 410 nm long-wavepass dichroic filter (Omega Optics, 3RD410LP) into an inverted objective (Olympus UPLSAPO apochromatic water immersion, 60x, 1.20 N.A.). The fluorescence from the focal region is collected by the objective, passes through the dichroic filter and is focused through a 150  $\mu\text{m}$  pinhole onto a 50/50 non-polarizing beamsplitter cube. Two single photon avalanche photodiodes (SPAD, Micro Photon Devices SPD-50-0TC) are positioned such that 50% of the photons collected through the pinhole strike each SPAD. A flip mirror can also be inserted into the beam path before the 150  $\mu\text{m}$  pinhole to allow for imaging onto an electron multiplying CCD camera (EM-CCD, Andor iXonEM+, model DU-897E-CSO-#BV). A variable neutral density filter can be inserted into the excitation beam path to control the flux at the single nanocrystal between  $\approx 15$  and  $1500 \text{ W}\cdot\text{cm}^{-2}$ ; these are standard values used in single nanocrystal experiments.

For wide-field excitation, a Köhler expanding lens ( $f = 100 \text{ mm}$ ) is inserted into the beam path before the dichroic filter. This lens shifts the focus of the excitation beam, allowing for imaging of a fairly large sample area (beam diameter at point of collection  $\approx 100 \mu\text{m}$ ). For optical bright-field imaging, a broadband, continuous wave halogen lamp was used to illuminate the sample and an image was collected onto the CCD camera through the same optics used for collection of fluorescence.

A PicoQuant PicoHarp 300 (PH300) picosecond histogram accumulating real-time processor board was interfaced with a PicoQuant PH403 router to allow for collection and identification of TTL signals from the two SPADs. Samples are mounted onto a cantilevered 3-axis piezoelectronically-driven stage (ThorLabs NanoMax MAX303) that is interfaced with a piezocontroller (ThorLabs BPC203); this setup provides precise position control to 5 nm.

### 1.4.2 Software design

Using the programming languages of LabView and C, software was developed to allow simultaneous raster scanning by the piezostage and collection of photon records by the PH300. The BPC203 module has been interfaced with the PH300 counting board and configured to generate TTL signals representing line-start, line-stop, and new frame. These signals result in insertion of markers within the TCSPC data stream, providing the capacity for simultaneous collection of spatially- and temporally-resolved images of a sample with a size of  $400 \mu\text{m}^2$ . The raster scans of fluorescence intensity can be analyzed either by a LabView program designed for the purpose, or by using the available PicoQuant SymPhoTime software, which computes fluorescence decay curves for each pixel in addition to an intensity-based image.

### 1.4.3 Confocal scanning of sample substrates

The  $20 \mu\text{m}$  pinhole through which the  $400 \text{ nm}$  excitation beam is focused produces a Gaussian beam profile; this beam is recollimated by and focused through the objective onto the sample area. Using the Rayleigh criterion to define the confocal region,

$$R = \frac{0.61\lambda}{N.A.}$$

where the excitation wavelength  $\lambda = 400 \text{ nm}$  and numerical aperture  $N.A. = 1.2$ , results in a Rayleigh radius of  $200 \text{ nm}$ . The calculated beam profile at the sample region is shown in Figure 1.5; this Nyquist calculation provides the size of the confocal region by taking into account the backprojected pinhole radius and the refractive index of the immersion fluid (water,  $\eta = 1.0$ ) and the substrate.<sup>56</sup> As expected for a confocal microscope using single-photon excitation, the depth of field is quite large at approximately  $8 \mu\text{m}$ .

This setup is theoretically predicted to yield a spatial resolution of  $\sim 200 \text{ nm}$ . To confirm this prediction, a measurement of the beam intensity around a single QD was

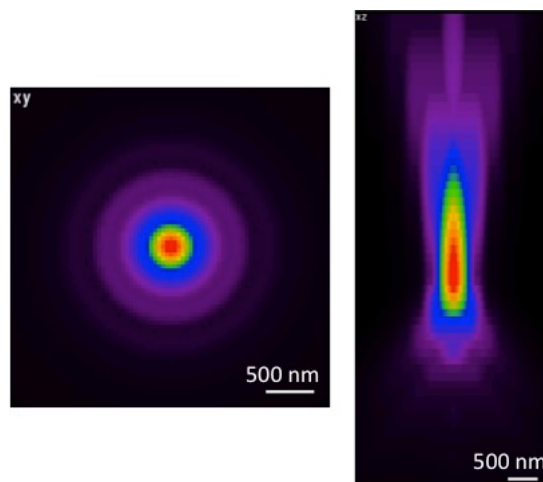


Figure 1.5: **Simulated profile of the confocal collection area.** Using measured parameters from the collected beam spot and the size of the confocal pinhole (150 $\mu\text{m}$ ), the confocal collection area was simulated

performed. This beam profile, created from the fluorescence of the QD, allows direct measurement of the beam diameter in the lateral ( $x$ - and  $y$ -) dimensions. This measurement is demonstrated in Figure 1.6. In practice, the spatial resolution of the instrument was found to be much lower than the theoretical resolution. Direct measurement of a single fluorophore yielded a resolution in both the  $x$ - and  $y$ -dimensions of  $\sim 400$  nm.

A raster scan of a spincast solution of commercial QDs (LifeTech<sup>TM</sup> QD605) recorded with the above-referenced software is shown in Figure 1.7. A sample time trace for one of the nanocrystals displayed in this image is shown in Figure 1.8. This trace was recorded with a flux of  $130 \text{ W}\cdot\text{cm}^{-2}$ , with photons subsequently placed in 100 millisecond time bins for analysis. This method of scanning, identification of single QDs, and measurement of intensity vs time traces was used to collect confocal time-resolved data for a number of representative QDs to confirm the capabilities of the single QD microscope.

The piezoresponsive scanning stage used for the confocal microscope is susceptible to thermal drift, but was typically stable enough for confocal measurement of single QDs for time periods of 5–10 minutes, as can be seen by the constant maximum intensity over a time period of 500 seconds shown in Figure 1.8.

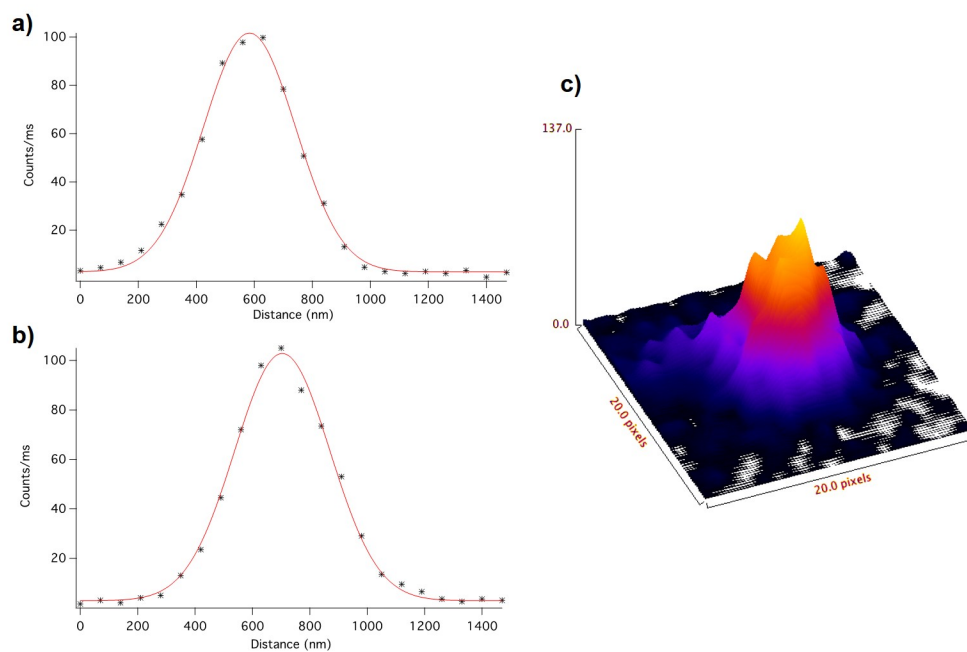


Figure 1.6: **Measured profile of the excitation beam.** The intensity of emission of a single QD under confocal excitation was measured using the Andor CCD camera. Gaussian fits to the emission intensity in the  $x$ - (a) and  $y$ - (b) directions allowed determination of the resolution of the confocal microscope. A 3D intensity profile of a single QD is shown in (c).

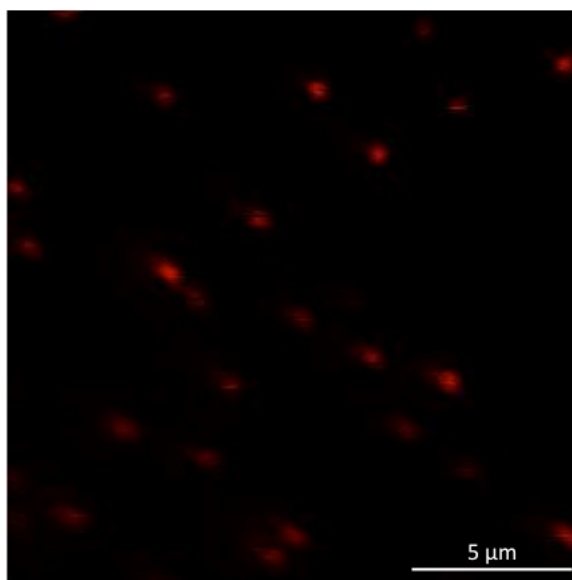


Figure 1.7: **Confocal raster scan of single QDs.** This image shows LifeTech™ QD605 QDs on glass. The sample was spincast from a  $\sim 1$  nM aqueous solution.

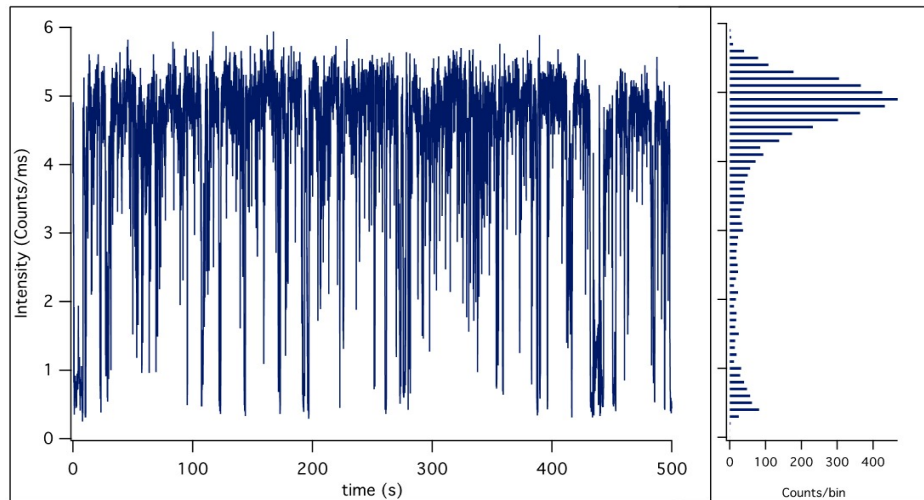


Figure 1.8: **Intensity vs time trace for a single QD.** *Left*– Photoluminescence intensity vs measurement time for one of the QDs shown in Figure 1.7. *Right*– Histogram of the binned intensity values showing the probability that the blinking QD would be observed in a high- (“on”) or low-intensity (“off”) state.

## Chapter 2

### Correlation of Atomic Structure and Photoluminescence of Individual Semiconductor Nanocrystals<sup>†</sup>

In a size regime where every atom counts, rational design and synthesis of optimal nanostructures demands direct interrogation of the effects of structural divergence of individuals on the ensemble-averaged property. To this end, we have explored the structure-function relationship of single quantum dots (QDs) *via* precise observation of the impact of atomic arrangement on QD fluorescence. Utilizing wide-field fluorescence microscopy and atomic number contrast scanning transmission electron microscopy (Z-STEM), we have achieved correlation of photoluminescence (PL) data and atomic-level structural information from individual colloidal QDs. This investigation of CdSe/CdS core/shell QDs has enabled exploration of the fine structural factors necessary to control QD PL. Additionally, we have identified specific morphological and structural anomalies, in the form of internal and surface defects, that consistently vitiate QD PL.

#### 2.1 The need for correlated interrogation of optical and structural properties of single colloidal quantum dots

Semiconductor QDs hold great promise for implementation in energy-efficient devices due to their high quantum yields, large extinction coefficients, and a high level of synthetic control over absorption, emission and electroluminescence properties.<sup>57</sup> Recent advances have resulted in realization of colloidal QD-based devices including light emitting diodes (LEDs),<sup>12,58,59</sup> flexible LED displays,<sup>60</sup> photovoltaics,<sup>19</sup> solar concentrators,<sup>16</sup> QD-lasers,<sup>61</sup> and even widespread use of QDs as a diffuser in LED displays. Further,

---

<sup>†</sup>Adapted with permission from Orfield N.J., McBride J.R., Keene J.D., Davis L.M., and Rosenthal S.J., "Correlation of Atomic Structure and Photoluminescence of the Same Quantum Dot: Pinpointing Surface and Internal Defects That Inhibit Photoluminescence" *ACS Nano* **2015** 9(1), 831-839. Copyright 2015 American Chemical Society.

QDs have reached ubiquity as molecular probes for *in vitro* fluorescence imaging because of their limited photobleaching, which enables robust fluorescence labeling and single particle tracking.<sup>62</sup> Despite their potential, colloidal QDs are plagued with charging and nonradiative recombination, phenomena which can be probed *via* time-resolved single QD spectroscopy and are manifested in the PL intermittency (PI) characteristic of single QDs.<sup>20,25,63,64</sup>

Since the first report on nanocrystal PI in 1996,<sup>20</sup> a large number of studies have investigated this phenomenon, which gives rise to an “off” time probability distribution governed by inverse power law statistics. These studies have shown that PI seems to arise due to trapping of charge carriers either within or at the surface of the QD heterostructure, and subsequent nonradiative recombinations within the charged QD.<sup>39,65</sup> Prior comprehensive studies have determined the dependency of “on”/“off” probability distributions on such factors as excitation intensity, excitation wavelength, and, when considering core/shell QDs, shell composition and thickness.<sup>9,21,22,66</sup>

There are many variations of core/shell syntheses in the literature, with variance in both the shell composition<sup>67</sup> and the level of gradation between core and shell.<sup>55</sup> Development of nonblinking QDs has been achieved by multiple groups; this blinking suppression is accomplished by encapsulating cores with many layers of shell material<sup>68</sup> and/or alloying materials to yield a smooth chemical potential between the core and shell.<sup>69,70</sup> Even these syntheses, however, produce a fraction of QDs that do not exhibit blinking suppression or are permanently dark, presumably due to structural inhomogeneity.<sup>71</sup> QD-to-QD structural variance almost certainly accounts for inhomogeneity noted in biexciton quantum yield, a parameter that must be optimized for realization of efficient QD lasers.<sup>29</sup>

Meanwhile, “nonblinking” is not the only desirable expression of QD PL intermittency behavior. When contemplating use of QDs for specific applications, a much more complex situation is encountered, as outlined in Table 2.1. In some cases, QD blinking is actually desirable—superresolution microscopy (nanoscopy) is attainable when the implemented

fluorescent species exhibits fast photoswitching, thereby facilitating localization of single fluorophores separated by nanometer distances.<sup>72,73</sup>

Blinking can be a hindrance in acquiring complete time-resolved location data for biological tracking experiments, but it can also provide useful additional information with which to identify labeled targets. Specifically labeling one target with nonblinking or controlled blinking QDs while labeling another target with blinking enhanced QDs would allow immediate identification of the distinct targets without the use of separate fluorophore colors. This would also make possible multiplexing via color and blinking behavior simultaneously, increasing the current maximum number of achievable targets manifold.

In the past, large-scale single-QD PL studies have treated all QDs as structurally identical, although some effort at correlation with structure has been attempted (see Section 2.2). Detailed investigation of the shape, size and structure of QDs, however, reveals appreciable heterogeneity among individuals from the same batch.<sup>52</sup> Indeed, inhomogeneous broadening in the PL spectra of ensemble QDs is a well-known phenomenon,<sup>74</sup> and has been attributed to the native polydispersity of colloidal QD samples.<sup>75</sup> Adding another degree of complexity, core/shell syntheses result in a complex atomic landscape with unique inorganic junctions on each QD; this landscape affects the excitation dynamics, decay dynamics, oscillator strength, and multiexciton properties,<sup>70</sup> which fluctuate with the addition of even a single atomic layer of core or shell material. In turn, the macroscopic properties of a group of these unique emitters are highly dependent on the distribution of atomic and electronic properties of QDs in the ensemble. Therefore, in order to fully comprehend the effects of atomistic structural variance on the electronic structure as a part of the ongoing effort to achieve complete control over QD fluorescence, correlation of structural information with collected PL transients for individual QDs is imperative.<sup>76–79</sup>

Table 2.1: Relationship between single QD PL behavior and desired application

<b>QD Application</b>	<b>Desired Property</b>	<b>Single QD behavior</b>
LEDs & QD televisions	High photoluminescence quantum yield	Nonblinking & no “dark” QDs
Biological labeling & Single particle tracking	Ease of localization	Nonblinking
QD lasers	High optical gain	Nonblinking & high biexciton quantum yield
Multiple target labeling	Readily differentiated QDs	Multiple types of controlled blinking
Super-resolution microscopy	Stochastic photoswitching of single fluorophores	Enhanced blinking

## 2.2 Previous correlation attempts by other groups

Previous attempts at correlating single QD structural information *via* electron microscopy with fluorescence data have been difficult. Basche *et al* reported on attempts to use carbon substrates as a TEM support film to correlate single QD structure with PL and PL polarization.<sup>80,81</sup> As described in Section 2.4, use of carbon for measuring the fluorescence properties of single QDs is likely to alter the absorption and emission dynamics of the QDs as compared to studies on SiO<sub>2</sub> or in solution.<sup>‡</sup>

One of the main problems that was encountered in the past was the ambiguity frequently present in correlation of PL and structure for single QDs. In the first published example of correlation, the authors reported recording of optical data for 65 QDs, of which 4 could be positively identified and correlated when performing TEM.<sup>80</sup> This 6% success rate, while impressive, needs to be improved upon vastly in order to provide a complete view of the different structures, morphologies, and PL expressions of single QDs. Even in the only subsequent work published to this initial paper, a deleterious high level of ambiguity was reported in the correlation method.<sup>81</sup>

Still others have used atomic force microscopy (AFM) to simultaneously correlate photoluminescence with the presence of single QDs.<sup>45</sup> This technique is very helpful for identifying “dark” QDs; however, implementation of AFM fails to provide structural insights at the atomic level.

Studies done by the Drndic lab have shown that photoluminescence time traces can be correlated with specific clusters of varying numbers of QDs.<sup>46,83</sup> These studies also stop short of allowing correlation of atomic structure and photoluminescence, however. A variety of other research has purported to identify the same QD in fluorescence and

---

<sup>‡</sup>Ours and previous studies show that use of carbon as a substrate is unlikely to allow adequate contrast for fluorescence imaging of single colloidal CdSe QDs without incredibly high excitation pump power.<sup>82</sup> The previous work on this topic may also have suffered from false positive signal acquired from aggregates, considering that the existing TEM-optical correlation studies report a high signal level for colloidal QDs with no inorganic passivation, and the authors admitted that the technique used showed a high level of ambiguity when identifying QDs in the electron microscope.

electron microscopes—due to the highly difficult nature of this correlation, however, it is key to demonstrate the methodology used to acquire such correlated images.

## 2.3 Experimental methods

### 2.3.1 Sample preparation

Samples were prepared by spincasting polystyrene latex spheres (PS, Ted Pella, 1  $\mu\text{m}$ ) from a stock aqueous solution onto transmission electron microscopy (TEM) support films (Ted Pella, PELCO 8 nm Ultra-Flat Silicon Dioxide Support Film). After spincasting, the PS naturally group into random formations that are readily identifiable in both fluorescence images and scanning transmission electron micrographs. These formations acted as fiducial markers from which single QD locations could be surmised, as illustrated in Figure 2.7. Subsequent to PS deposition, 5  $\mu\text{L}$  of a 100 pM aqueous QD solution was dropped on the support film; residual liquid was wicked away with a KimWipe. This sample preparation resulted in a density of  $\sim 0.0015$  QDs/ $\mu\text{m}^2$ ; this ensured single QDs were adequately spatially separated to avoid influence of QD–QD interactions. The sample preparation procedure is illustrated in Figure 2.1.

### 2.3.2 Optical microscopy

The optical setup is a modified version of that reported by Dukes *et al.*<sup>54</sup> A neodymium-doped yttrium orthovanadate (Nd:YVO<sub>4</sub>) continuous-wave laser (Coherent Verdi, 532 nm, 18W) pumps a titanium sapphire (Ti:Al<sub>2</sub>O<sub>3</sub>) oscillator (Coherent, Mira 900 basic, 800 nm). The oscillator seeds a regenerative amplifier (Coherent, RegA 9000) that is used to drive an optical parametric amplifier (Coherent, OPA 9400). The frequency doubled output of the OPA 9400 is used in these experiments because it provides excitation at 400 nm and a pulse separation of 4  $\mu\text{s}$ , thus ensuring that the QDs are able to fully relax between excitation events. The excitation beam passes through a neutral density filter and reflects from

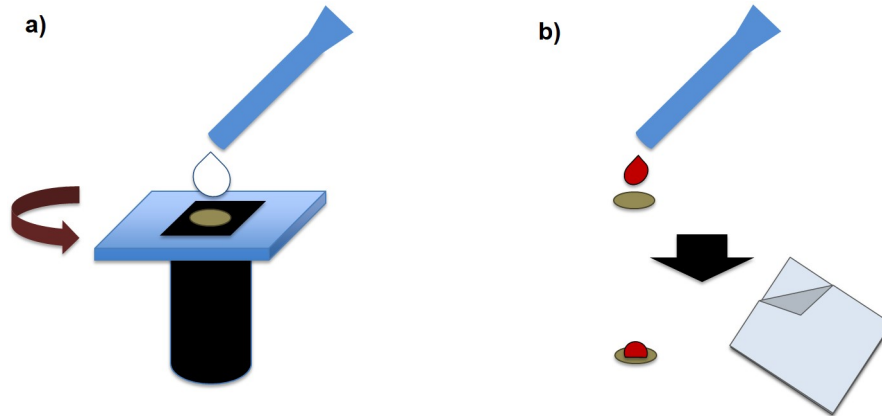


Figure 2.1: **Preparation of TEM support films for correlation.** (a) The support film is carefully placed on double-sided carbon tape on a microscope cover glass. A drop of stock aqueous polystyrene latex spheres is then spincast onto the support film. (b) Subsequent to spincasting of the polystyrene latex spheres, the support film is removed from the double-sided tape, then a dilute droplet of aqueous QD solution is dropped onto the support film and subsequently wicked away with a KimWipe. See text for full details.

a series of mirrors before being expanded  $\times 2$  and focused by a 300 mm focal length lens to provide wide-field Köhler epi-illumination within a custom-built inverted microscope. The microscope uses a water immersion objective (Olympus, UPlanSApo 60 $\times$ , 1.2 N.A.,  $\infty/0.13$ – $0.21$ , FN 26.5). The excitation beam is linearly polarized and enters the objective off a 410 nm long-pass dichroic filter (Omega Optics, 3RD410LP) set for s-polarized reflection at an incidence angle of  $\sim 10^\circ$ . A 3D piezostage (ThorLabs, MAX301) and controller box (ThorLabs, BPC203) were used to lower the sample into position above the objective. Emitted fluorescence from the excitation area, which was a disk of  $\sim 100$   $\mu\text{m}$  diameter, was collected by the objective, passed through the dichroic and a 600 nm LP filter (ThorLabs, FEL0600) and is imaged onto an EM-CCD camera (Andor, iXonEM+, DU-897e-CSO-#BV) using an achromat tube lens with focal length of 250 mm and a 1:1 relay lens system, resulting in an optical magnification of 83.3. The neutral density filter was adjusted to limit irradiance in order to prevent multiple exciton generation.

Once the sample was prepared, the TEM support film was placed, facing downward, onto a No. 0 glass coverslip. This imaging geometry is illustrated in Figure 2.2. The

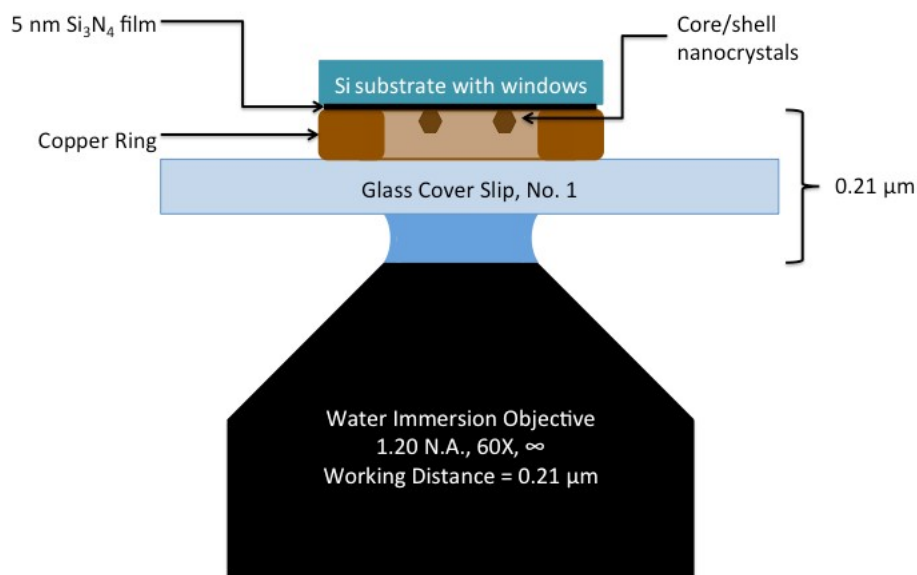


Figure 2.2: **Geometry for fluorescence imaging of QDs on a TEM support film** The copper ring can be removed for imaging if necessary. For preliminary experiments, 5 nm thick Si<sub>3</sub>N<sub>4</sub> films on Si windowed substrates were used. For later work, SiO<sub>2</sub> films were used for imaging, as described in Section 2.4.

piezostage was maneuvered to bring the image on the EMCCD camera into focus. The focus was found by removing the Köhler lens and adjusting the piezo stage so that the laser beam focused at the coverslip and partially reflected back along the incident path. Polystyrene latex beads were used in conjunction with the border of the support film to allow for recording of positional information. The EM-CCD was cooled to  $-50^{\circ}\text{C}$ , and all videos were recorded at a frame resolution of 100 ms (refresh rate 0.1027 s) for 20,000 frames (2054 s). The illuminated portion of the sample was imaged onto a section of the camera with a diameter of  $\sim 250$  pixels. Electron-multiplying gain was set to  $300\times$  and pixels were binned  $2\times 2$ , resulting in an image of  $128\times 128$  pixels with  $0.384\ \mu\text{m}/\text{pixel}$  in object space.

### 2.3.3 Electron microscopy

Scanning transmission electron microscopy images were obtained using a Tecnai Osiris operating at 200 kV, with a spot size set to 10 (to reduce charging effects) and a cam-

era length of 220 mm for HAADF imaging. STEM-HAADF imaging was chosen over HRTEM imaging since the white-on-dark-contrast for STEM greatly facilitates the location of individual quantum dots at low magnifications. Patterns of polystyrene were used to align the STEM image and distances measured from the optical microscope were used to identify regions of interest. Large area images were used to identify neighboring particles and possible dark particles.

#### 2.3.4 Data analysis

The brightest pixel in a  $2 \times 2$  pixel area in each frame was chosen and used to determine the transient for each QD. Very infrequently, STEM imaging would reveal the presence of multiple QDs in the same ROI from optical imaging. In this case, the ROI was not considered a part of the single QD population being probed. Custom LabView software was used to determine the following parameters for each QD according to the referenced literature methods: (a) on (off) times, (b) on (off) time probability distribution,<sup>64</sup> and (c) on (off) time memory parameters  $R(\text{on})$ ,  $R(\text{on})_{\log}$ ,  $R(\text{off})$ ,  $R(\text{off})_{\log}$ .<sup>84</sup>

#### 2.4 Selecting a suitable substrate for correlated photoluminescence microscopy and electron microscopy

There are numerous considerably important considerations when selecting a substrate that is well-suited to both optical microscopy and imaging with an intensely focused electron beam. Typically, when performing single QD fluorescence studies, some form of  $\text{SiO}_2$  substrate is used to support the samples,<sup>§</sup> as  $\text{SiO}_2$  is an electrically insulating material with

---

<sup>§</sup>Early reports of single QD microscopy utilized a strategy of embedding the dots in a layer of polymer—such as poly(methyl methacrylate) (PMMA)—to prevent the surface of QDs from photodegradation processes such as surface oxidation. Inorganic shelling has made this practice unnecessary for robust excitation of and detection from single QDs.

minimal fluorescence at visible wavelengths.<sup>¶</sup>

Prior experiments have reported the use of traditional graphite-on-copper support films or thin  $\text{Si}_3\text{N}_4$  on windowed silicon grids for attempts at full correlation of optical and structural data. Initial efforts to reproduce the success of Basche *et al* in the use of carbon for a support film were met with no success. Using a commercially available colloidal QD system—LifeTech<sup>TM</sup> QD605—the spincast QD density was determined to be appropriate for interrogation of single QDs *via* TEM, but no QD fluorescence was visible under optical excitation with a 400 nm excitation source. This lack of fluorescence can most likely be attributed to the conductive nature of the graphitic carbon grids.<sup>||</sup>

The lack of success with using traditional conductive support substrates that are ideal for electron microscopy led to the investigation of  $\text{Si}_3\text{N}_4$  as a possible substrate for correlated imaging. The prior study which used this support film demonstrated measurable PL and identification of clusters of QDs, although single QD imaging was not achieved.<sup>83</sup> A fluorescence scan of a section of a  $\text{Si}_3\text{N}_4$  substrate coated with QDs is shown in Figure 2.3.

The QDs on the  $\text{Si}_3\text{N}_4$  film can be seen to blink during the raster scan, as indicated by dark “striped” lines in the fluorescence image. This raster scan indicates an enhanced blinking rate of QD605 as compared to the QDs on a  $\text{SiO}_2$  substrate; this comparison can be made between Figure 2.3 and 1.7 to bring into sharp relief the difference between QDs on glass and QDs on thin  $\text{Si}_3\text{N}_4$  membranes. A fluorescence time trace of one of the QDs from Figure 2.3 (shown in Figure 2.4) illustrates this effect, in stark contrast to that shown in Figure 1.8 of a single QD on  $\text{SiO}_2$ .

Despite being a useful electron microscopy substrate that is aptly suited to measurement of single QD fluorescence, using a  $\text{Si}_3\text{N}_4$  substrate nonetheless presented a problem—

---

<sup>¶</sup>For QDs with PL emission peaks centered around or redshifted from 550 nm, a thin No. 1 glass cover slip can be used as a substrate, and collected emission can be filtered from glass fluorescence with an appropriate long-wave pass dichroic filter. For QDs with PL emission blueshifted from 550 nm, it becomes necessary to use ultrapure fused silica, which is made from sand that has had fluorescent impurities removed before flaming.

<sup>||</sup>Graphene grids were also investigated, but once again to no avail. It was soon shown in a literature report that graphene is able to participate in FRET with single QDs, thereby resulting in an observed quench of single QD PL.<sup>82</sup> This effect has also been shown with other two-dimensional materials.<sup>85</sup>

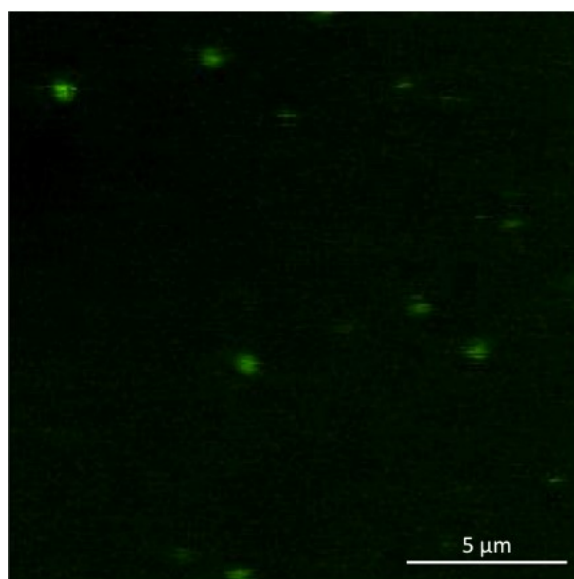


Figure 2.3: **Fluorescence of single QDs on a  $\text{Si}_3\text{N}_4$  TEM support film** Shown is a confocal raster scan of the fluorescence of QDs (LifeTech<sup>TM</sup> QD605) on a 40 nm thick  $\text{Si}_3\text{N}_4$  TEM support film inverted onto a microscope cover glass, as shown in Figure 2.2. The enhanced blinking seen here can be readily identified when comparing with the confocal raster scan of the same QDs on a  $\text{SiO}_2$  substrate seen in Figure 1.7 (page 19).

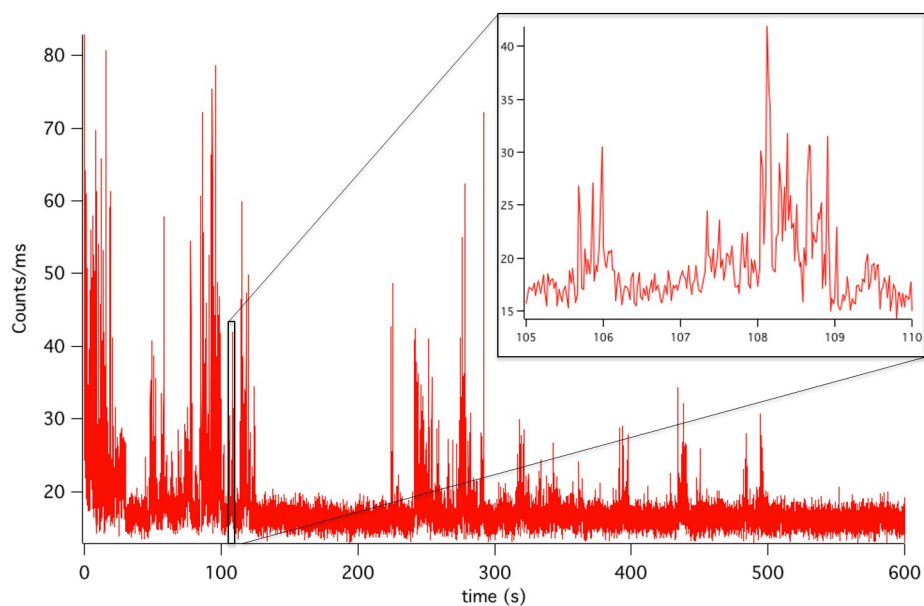


Figure 2.4: **Photoluminescence intensity vs time trace for a single QD on a  $\text{Si}_3\text{N}_4$  substrate** “Off” times of single QDs were greatly enhanced on a  $\text{Si}_3\text{N}_4$  substrate.

standardization would be difficult because prior studies have investigated single QD fluorescence on SiO<sub>2</sub>, and interaction between the substrate and the QDs would prevent direct comparison of measured results with those from existing literature studies. When considering approaching this difficult problem by replicating decades of single QD experiments on a new, non-ideal substrate for fluorescence imaging, it became apparent that an optimal imaging substrate would be the one that has been used for all previous studies—namely, SiO<sub>2</sub>.

The foreseen difficulty with using SiO<sub>2</sub> for imaging in an electron microscope is the lack of an efficient charge dissipation mechanism for this electrically insulating material. Fortunately, for the ultrathin 8 nm and 40 nm support films that are now commercially available, buildup of charge was not observed to be an inhibiting factor in obtaining lattice-resolved electron micrographs of single CdSe/CdS QDs. The remainder of the work presented in this dissertation was performed on just such commercially available substrates.

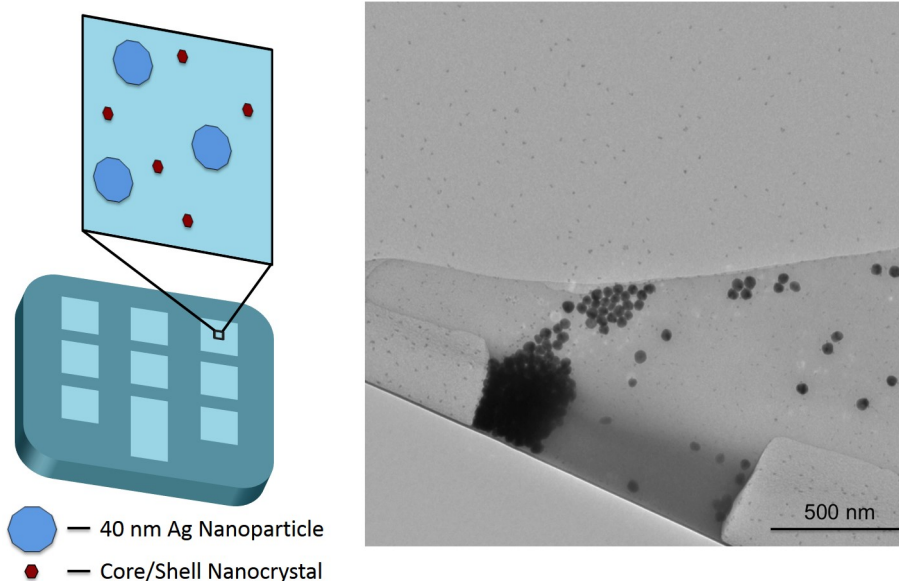


Figure 2.5: **Use of  $\text{Si}_3\text{N}_4$  as a substrate for electron microscopy.** An attempt to use silver nanoparticles as fiducial markers for correlated imaging of QDs was inhibited by the tendency of the silver to aggregate rather than disperse over the  $\text{Si}_3\text{N}_4$  film.

## 2.5 Needle in the hay: unambiguous correlation of photoluminescence and fine atomic structure of the same colloidal quantum dot

Our initial attempts at correlation aimed to implement plasmonically-active 40 nm diameter silver nanoparticles as fiducial markers to provide positional information when observing the same mesoscale substrate area on the optical and electron microscopes. An example of such an attempt can be seen in Figure 2.5, where silver nanoparticles and single QDs can be seen in the same area of the TEM grid.

Unfortunately, despite their visibility on both imaging systems, these silver nanoparticles were difficult to unambiguously identify on the TEM grid due to their small size. When selecting fiducial markers, a simple, inexpensive method was preferred over methods such as the electrodeposited silver maps used by other groups in the past.<sup>80,81</sup> This led

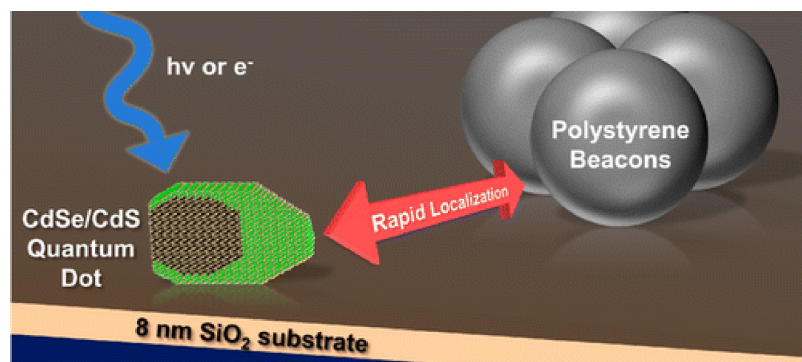


Figure 2.6: **The strategy for correlation of single QD photoluminescence behavior with atomic structure.**

to selection of readily available polystyrene latex beads (PS)\*\* as the next candidate for fiducial markers. The general strategy for correlation is pictured in Figure 2.6. The use of PS proved crucial to correlation process.

The straightforward method for collection of fluorescence and atomic structure from the same samples is illustrated in Figure 2.7. This method is ideal, because it implements only widely available instrumental components without major modifications to the optical or electron microscope. This strategy could be employed by any researcher with access to a fluorescence microscope and transmission electron microscope. In fact, as shown later in Figure 4, this method was easily employed on a separate fluorescence microscope, with no instrumental modifications necessary.

---

\*\*The beads used here are intended for use as a TEM sizing standard; spheres are synthesized at a specified volume and can be used to calibrate length scales on electron microscopes. A slightly more expensive, but more versatile option would be the use of fluorescent beads: polymer spheres embedded with dye molecules that would allow the user to select the desired emission wavelength of the fiducial marker for possible spectral separation of the marker and QD signal.

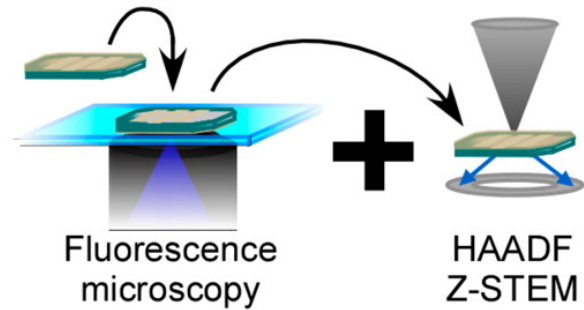


Figure 2.7: **Correlation of optical and electron microscopy.** Correlation was achieved by loading an 8 nm  $\text{SiO}_2$  support film on a windowed  $\text{Si}_3\text{N}_4$  frame with polystyrene latex spheres and QDs. The grid was placed face down onto a coverslip to allow for optical imaging, and subsequently imaged in the electron microscope.

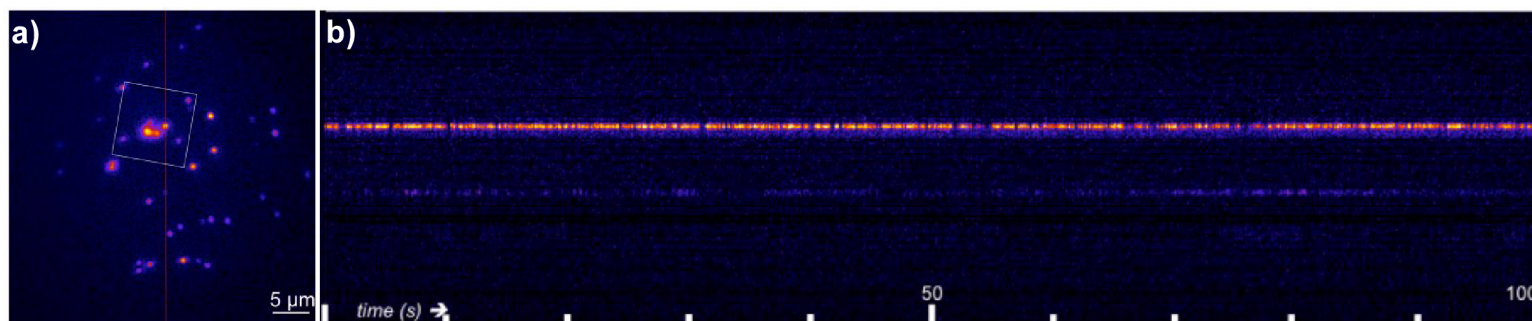


Figure 2.8: **Fluorescence imaging of single QDs on a 40 nm thick SiO<sub>2</sub> substrate.** (a) An image mapping the fluorescence maximum for each pixel over 100 s shows the location of QDs under wide-field optical excitation. In this image, brightness is indicative of a convolution of single QD fluorescence intensity and “on” time. (b) A slice showing the intensity vs time for the pixels found along the red line drawn in (a). Blinking of single QDs is visualized as bright and dark periods as a function of time.

A fluorescence image obtained under wide-field 400 nm Köhler illumination and collection with a cooled CCD array detector is shown in Figure 2.8a. The method for collection of this fluorescence image is described in full in section 2.3. Wide-field illumination and collection was found to be more useful for comprehensive imaging of all QDs on a substrate, as raster-scanning confocal methods have three major flaws: these methods (1) ignore “dark” QDs, (2) miss any QDs that are “off” during the initial scan, and (3) are subject to a great deal of user selection bias when choosing which QDs to examine. An example of the QD time trace that can be extracted from the collected time-dependent fluorescence image is shown in Figure 2.8b.

In the center of the fluorescence image shown in Figure 2.8a, two large fluorescent circles can be seen. These larger fluorescent species are the PS, and are readily distinguished from QDs due to their larger size. An illustration of the general method that allows for identification of regions of a TEM grid *via* PS bead deposition is shown in Figure 2.9. The PS formations are unique due to the variability of both the number of PS in a formation and the orientation of the resultant formation.

Figure 2.10 demonstrates the method for performing STEM on the same region of the grid for which fluorescence has already been collected (Figure 2.10a). Figure 2.10b shows an uncorrected high angle annular dark field (HAADF) STEM image of this region. When performing STEM at low magnification, QDs can be difficult to identify. Indeed, in the case of the image shown, the QD is smaller than the pixel size. However, the QDs reliably appear as single bright pixels, or 2-3 bright adjacent pixels. Typically, it is possible to identify these bright areas directly upon imaging. In order to verify the presence of QDs, however, post-processing can be performed to identify the bright pixels that correspond to QD location. Figure 2.10c shows an image that was obtained by applying a “maximum” filter to the micrograph in Figure 2.10b. In this processed image, the QDs that were previously identified *via* fluorescence imaging can be rapidly identified for high-magnification imaging. Figure 2.10d is a cartoon of the investigated region.

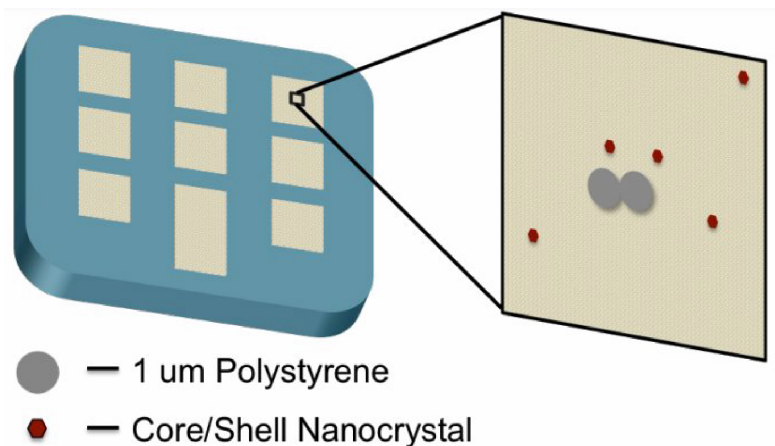


Figure 2.9: **Support film configuration and use of PS as fiducial markers.** *Left*– A SiO<sub>2</sub> support film is suspended over a windowed silicon TEM grid. Imaging is performed on the regions of suspended SiO<sub>2</sub>. *Right*– A cartoon illustrating the mapping strategy for identifying specific regions of the grid. PS group into formations that are readily identifiable due to arbitrary, unique aggregation and orientation. QDs locations relative to PS formations are recorded on the fluorescence microscope to guide the localization during electron microscopy.

Figure 2.11 demonstrates the final result—fine atomic structure of individual QDs for which the photoluminescence behavior is known. The QDs shown here correspond to the previously identified QDs in the cartoon shown in Figure 2.10. The QD labeled “NC3” is the structure which corresponds to the bright fluorescence time trace previously shown in detail in Figure 2.8.

## 2.6 Conclusions

The first technique to allow full correlation of time-resolved PL behavior and fine atomic structure of QDs has been developed. The technique shown here could theoretically be applied for a variety of metallic and semiconducting nanostructures. The universality and simplicity of the correlation method presented makes it ideal for studying heterogeneity within these systems, as well as for performing an in-depth study of the QD system shown in this chapter.

This method is also tunable for the desired application, and the non-intrusive nature of

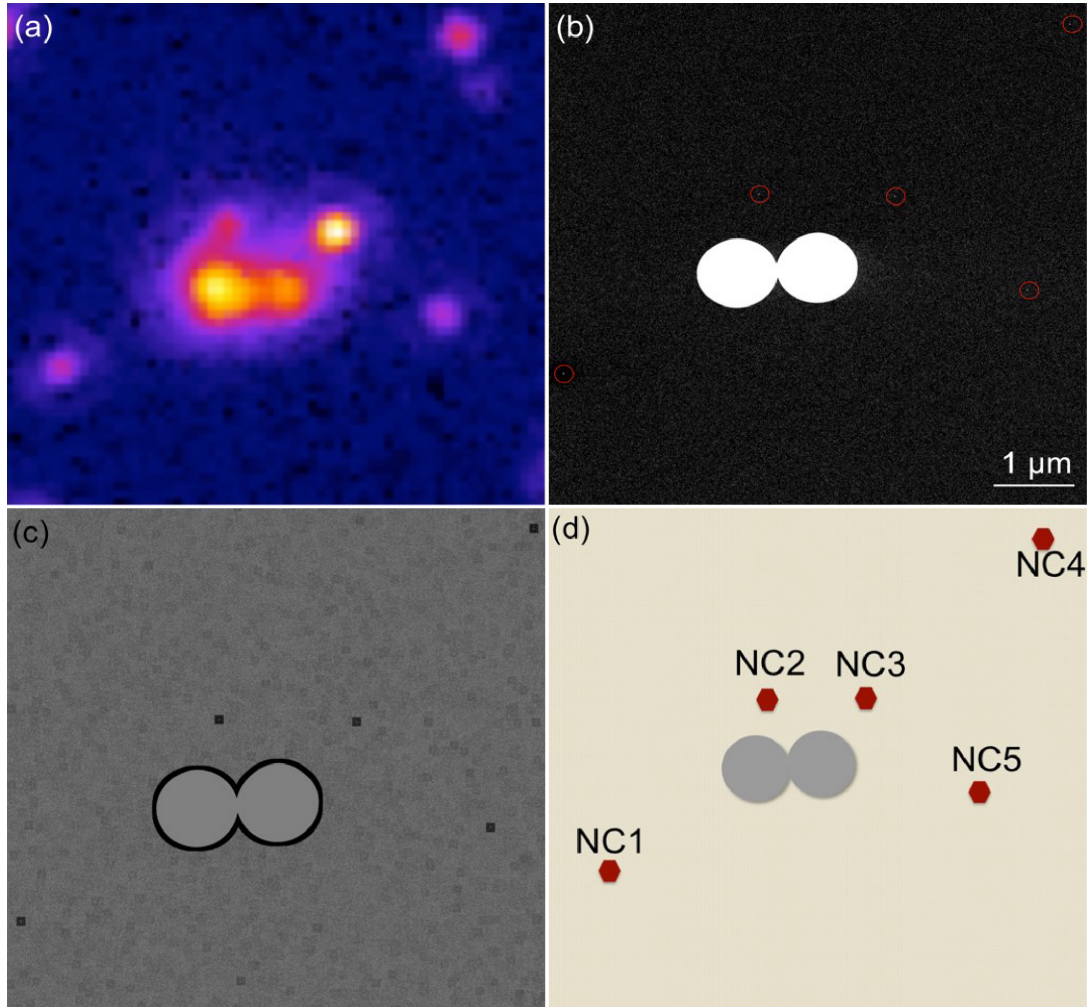


Figure 2.10: **The first demonstration of unambiguous correlation of optical and electron microscopy for QDs.** (a) An expanded view of the center region of the fluorescence image previously shown in Figure 2.8. (b) A scanning transmission electron micrograph of the same region of the SiO<sub>2</sub> TEM support film. QD locations are enclosed in red circles for clarity. (c) A maximum filter of the STEM image shown in (b), with pixel width set to 5. Post-processing allows facile identification of regions of high contrast in the STEM images that correspond to QDs. (d) A cartoon representing the location of QDs in both the STEM and fluorescence images.

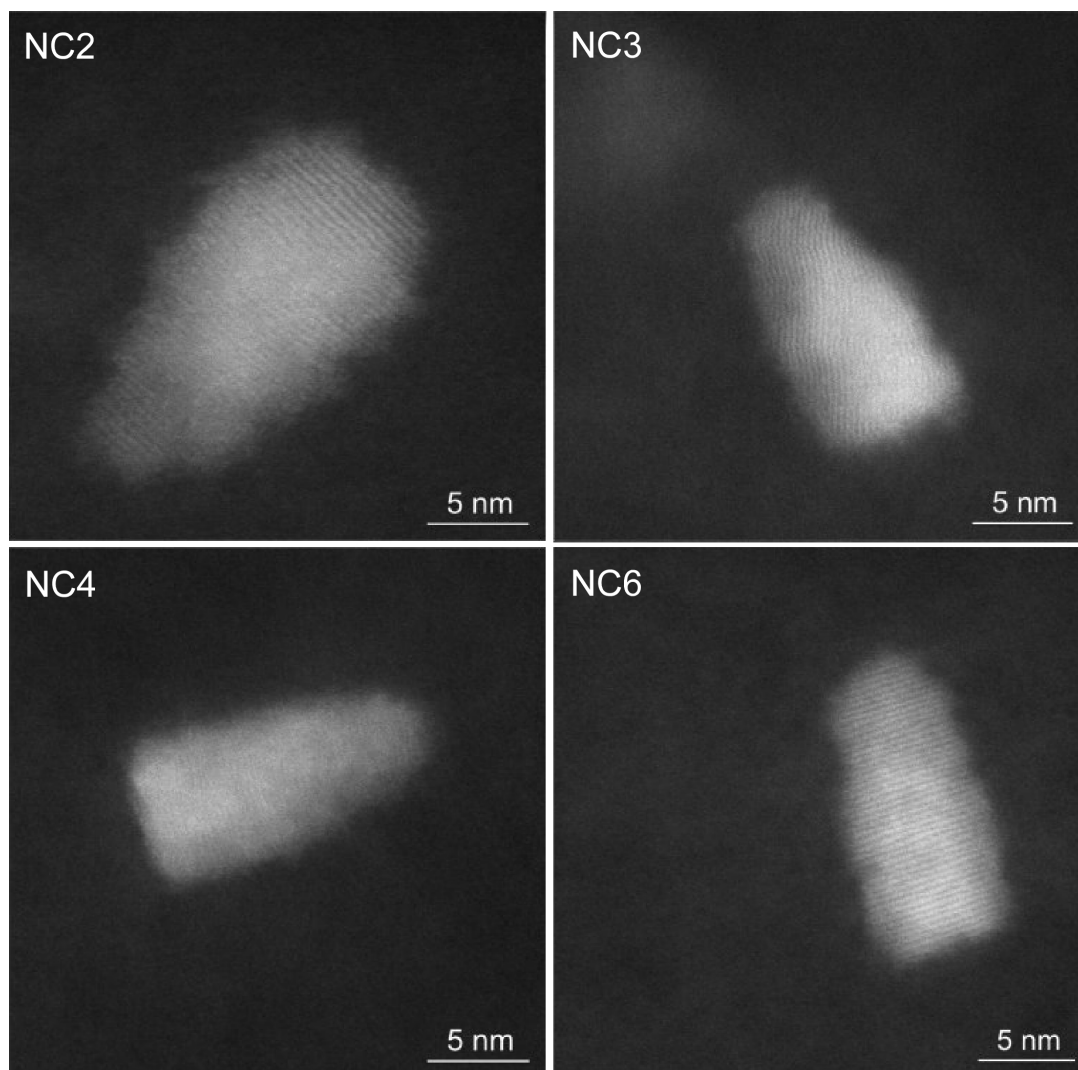


Figure 2.11: **Structures of QDs shown in the wide-field images in Figure 2.10.** High resolution scanning transmission electron micrographs of single QDs for which fluorescence had previously been collected. NC3 corresponds to the time trace shown in Figure 2.8.

the imaging setup allows for performance of this sophisticated analysis with common, commercially available tools. This method could be expanded to include a variety of optical properties other than photoluminescence—one could conceivably measure single nanos-structure Raman spectra,<sup>5</sup> plasmonic emission,<sup>6</sup> and even fine absorption spectra<sup>8</sup> and correlate these measurements with single particle structure.

The next two chapters demonstrate application of this method to QD systems to determine previously-unattainable insights into structure-dependence of PL (Chapter 3) and the nature of charging in single QDs (Chapter 4).

## Chapter 3

### Visualizing Nonradiative Internal and Surface Defects: The Role of Stacking Faults and Anomalous Shell Epitaxies in Nonradiative Recombination<sup>†</sup>

#### 3.1 Choice of quantum dot system to study

For this study, PL time traces and high angle annular dark field (HAADF), also known as atomic number contrast scanning transmission electron microscopy (Z-STEM), images were collected for a total of 84 QDs, examples of which are shown in Figure 3.1.

For our experiments, we chose to use commercial QDs (Life Technologies, QDOT 655). In ensemble, these QDs possess a narrow emission fwhm of 27 nm; the typical morphology and detailed atomic structure have also been described in the past.<sup>53</sup> Despite the high quality of the ensemble optical spectra, the aforementioned previous studies showed that a moderate level of structural and morphological diversity is encountered on a single QD basis. This QD-to-QD variation provides an ideal platform from which we can learn about both core/shell growth phenomena and structure-function relationships of QD heterostructures. The ensemble statistics of the 84 QDs studied are highlighted in Figure 3.2.

The heat map overlay shown in Figure 3.2a illustrates the physical heterogeneity of the QDs studied here. The morphology studied is an anisotropic core/shell, with the CdSe core in the dark region of the heat map and the CdS shell growing preferentially from one facet in a lengthwise direction. Heterodispersity observed in the length of these QDs is reflective of differing amounts of shell material, as illustrated in Figure 3.2b and shown in the histograms in Figure 3.2c,d.

The QD heat map overlay was created by overlaying the profiles (cross sectional areas) of each of the 84 QDs examined in this study. The intensity is linearly scaled in the fol-

---

<sup>†</sup>Adapted with permission from Orfield N.J., McBride J.R., Keene J.D., Davis L.M., and Rosenthal S.J., "Correlation of Atomic Structure and Photoluminescence of the Same Quantum Dot: Pinpointing Surface and Internal Defects That Inhibit Photoluminescence" *ACS Nano* **2015** 9(1), 831-839. Copyright 2015 American Chemical Society.

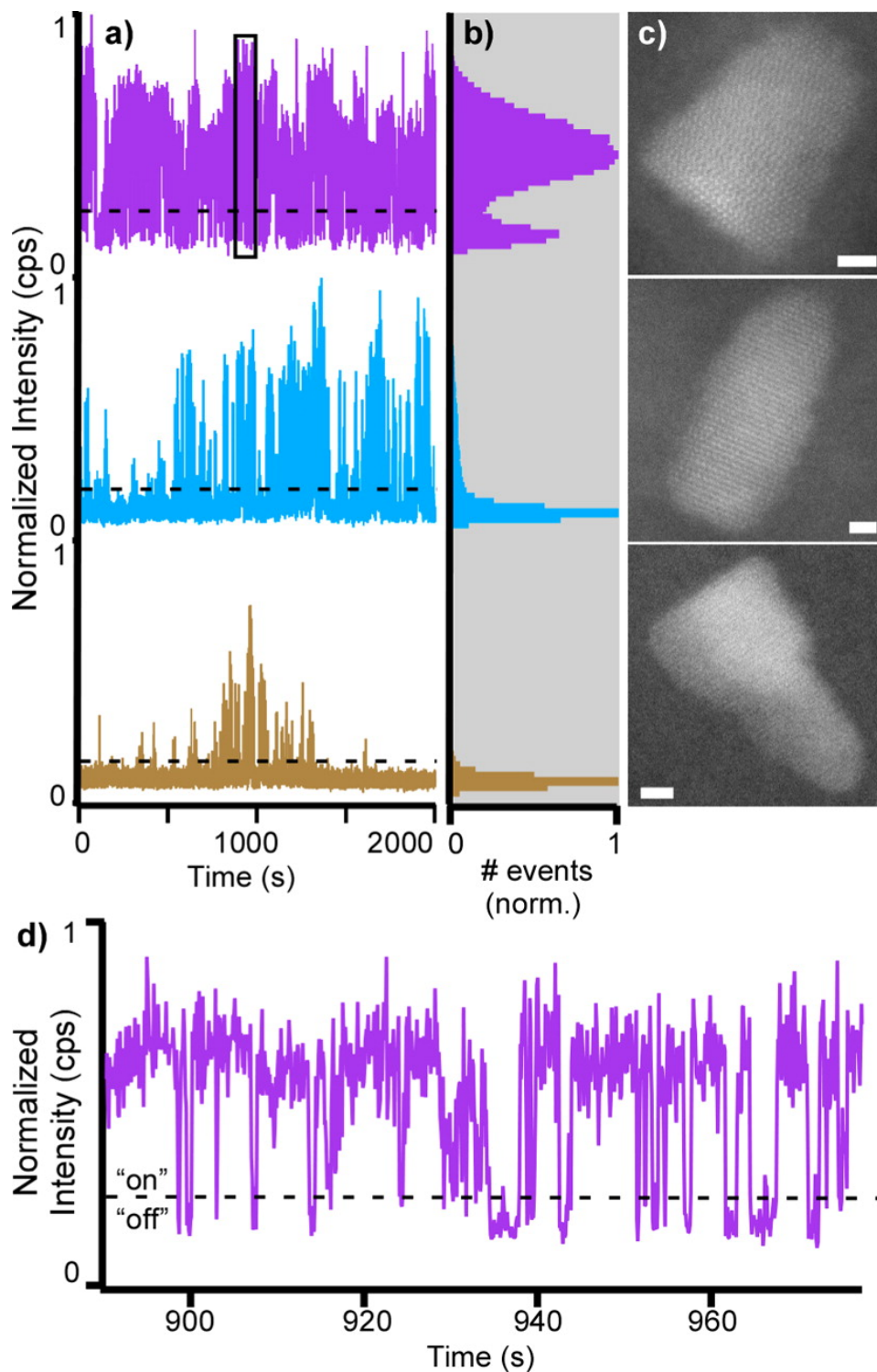


Figure 3.1: **Correlated fluorescence and structural data for individual QDs.** Shown in (a) are full fluorescence intensity transients; (b) shows the corresponding fluorescence intensity histograms for the 3 QDs whose structures are shown in (c). (d) The boxed truncated portion of the topmost fluorescence intensity transient in (a) shows the “on” and “off” states of a fluorescent QD. Scale bars in (c) are 2 nm.

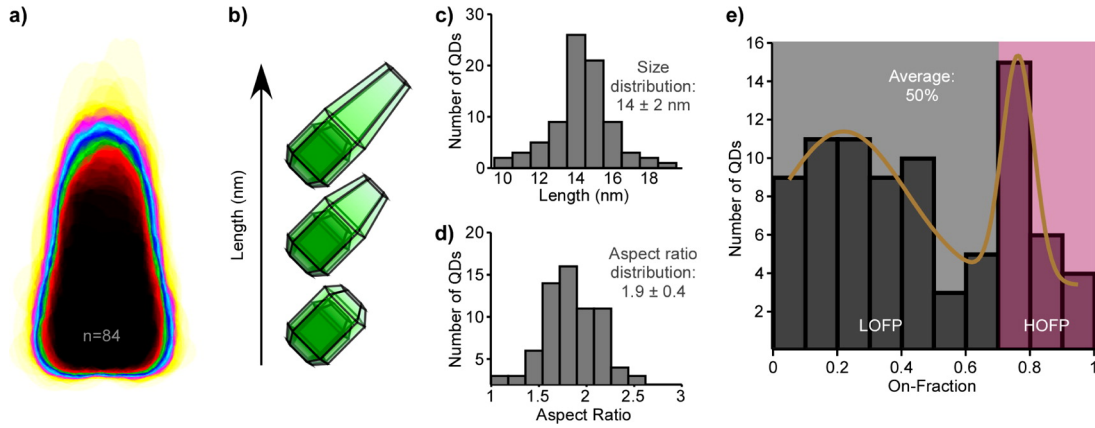


Figure 3.2: **Heterogeneity within the core/shell nanocrystal ensemble.** (a) A heat map overlay of the 84 QDs investigated displays the morphological heterogeneity in the observed population. (b) Because the core size is effectively equal among QDs, length reflects the amount of shell coverage in the direction of the  $C_{3v}$  (long) axis. (c) Size distribution and (d) aspect ratio distribution of the examined QD population. (e) The distribution of all observed QDs as a function of on-fraction. We observed that the QDs inhabited a low on-fraction population (LOFP) and high on-fraction population (HOFP).

lowing order, from lowest to highest intensity: yellow, magenta, cyan, indigo, green, red, black. This heat map is meant to illustrate the size dispersity of the examined QDs, and is not scaled for Z-STEM intensity contrast.

### 3.2 “On”-fraction heterogeneity in commercially available CdSe/CdS core/shell quantum dots

For each QD, the amount of time spent in the emissive “on” state was calculated and divided by the total collection time to find the QD on-fraction.<sup>86</sup> All on-fraction data is represented in the histogram shown in Figure 3.2e. All of the QDs examined, including the 7 permanently nonradiative QDs, fall into two separate subpopulations, one of which has a much higher on-fraction than the other. We delineate a high on-fraction population (HOFP) and low on-fraction population (LOFP) as illustrated in Figure 3.2e. We observe that the LOFP results from some QDs exhibiting defects resulting in a drastic reduction in on-fraction. We analyzed Z-STEM images to compare the QDs inhabiting each popula-

tion, allowing us to understand the distinct structural features that result in QD on-fraction segregation. All Z-STEM images for the 84 QDs studied herein are shown in Appendix A.

The Z-STEM images hold a wealth of information including size parameters, crystal structure, CdS shell epitaxy, and QD orientation. Additionally, contrast highlights variances in atomic composition, providing information about the shell epitaxy and core/shell interface.<sup>53</sup> Using this information in conjunction with observed lattice fringes and previous work<sup>52,87</sup> we determined which facets of the core were passivated by CdS and how much shell material was present for each QD. For the purposes of our discussion, because there is some overlap in the LOFP and HOFP, we established the cutoff at an on-fraction of 0.70. In all, 26 of the investigated QDs (31%) resided in the HOFP; these QDs exhibited both structural integrity and inorganic passivation of a large number of facets on the CdSe core by the CdS shell.

### 3.3 The good: Ideal quantum dot structures in the high on-fraction population

The collected data also allowed us to visualize the structures of QDs with high on-fractions in an effort to ascertain unifying characteristics within this population. Not surprisingly, the most commonly observed features were good structural integrity and near-complete inorganic passivation of the core. Two other less-expected features were observed as well. Out of the 84 QDs studied, the QDs oriented on end, with the  $C_{3v}$  axis perpendicular to the substrate, were seen to reside in the HOFP (average on-fraction = 0.87,  $n = 3$ , Figure 3.3a).

Z-STEM images show that, for these QDs, a large number of (010), (100) and corresponding facets are well passivated by CdS, resulting in high on-fractions. The reduced cumulative “off” time in these QDs may be further explained by a lack of interaction of the CdS shell surface with the  $\text{SiO}_2$  substrate. Further exploration of this orientation in the future will allow a more complete understanding of the high observed on-fraction.

Figure 3.3b highlights a subset of QDs with a high on-fraction that exhibit a previously

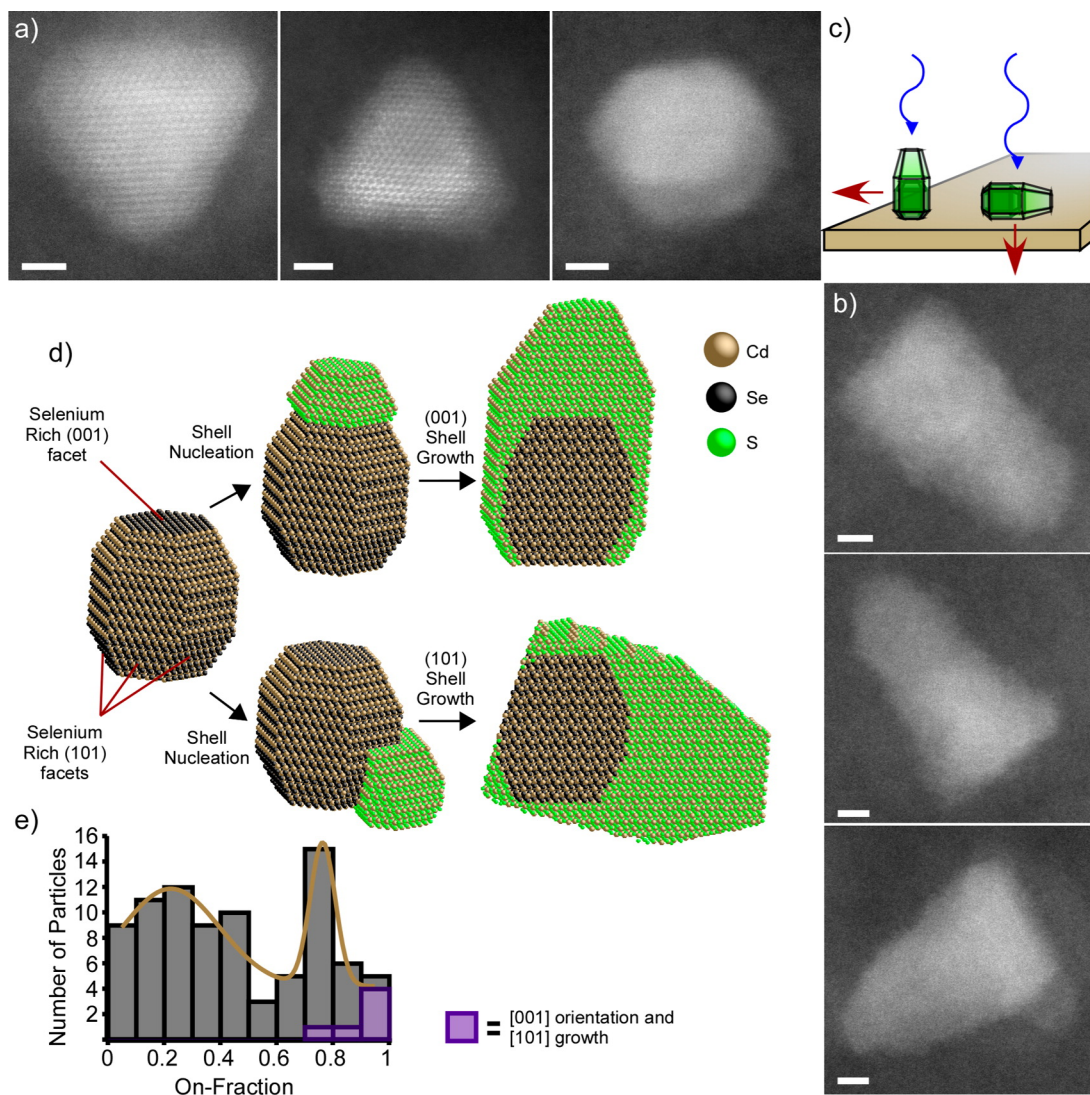


**Figure 3.3: Structures of suppressed blinking QDs.** The QD configurations with the highest on-fraction are shown in (a) and (b). Only three QDs were oriented along the *c*-axis (a), as shown on the left in (c); these QDs all exhibited highly suppressed blinking. All QDs but these three were oriented side-on, as shown on the right in (c). Also included in the high on-fraction population were QDs showing CdS shell growth from the Se-rich (101) face of the CdSe core (b). A cartoon of the previously unaddressed growth mechanism of these QDs is illustrated below the more common traditional growth in (d). The on-fraction distribution of these QDs with respect to all QDs in the sample demonstrates the suppressed blinking observed (e). Scale bars are 2 nm.

unaddressed shell growth (average on-fraction = 0.89,  $n = 3$ ). The lattice spacing and orientation of these QDs indicate that the view angle is along the [111] axis. In order for this structure to be formed, the CdS shell must nucleate and grow from a Se-rich (101) facet, as opposed to the commonly observed nucleation and growth from the Se-rich (001) facet. Although the traditional “bullet” shape is preserved, the lengthwise growth does not occur parallel to the  $C_{3v}$  axis of the CdSe core. This growth mechanism is highlighted in Figure 3.3d. Because the (101) facet is surrounded by two other Se-rich (101), one chemically neutral (010), and only one Cd-rich (001) facet,<sup>88</sup> shell growth after nucleation passivates a large area on the surface of the core. Specifically, this growth method seems to passivate the Cd-rich (001) facet, which is typically almost completely bare for the more common “bullet” shaped QDs, as seen in Figure 3.3d.

### 3.4 The bad: Stacking faults and visible surface irregularity act as nonradiative recombination centers

The presented technique allowed us to directly correlate specific structural defects with decreased photoluminescence of individual QDs. We used the acquired data to understand the effect of three commonly encountered defects: (1) stacking faults within the core or the core/shell heterostructure, (2) unpassivated Cd-rich (101) core facets, and (3) an etched/unpassivated Cd-rich (001) core facet. Out of the 84 QDs studied here, 12 were seen to exhibit highly visible zinc blende stacking faults. An example is shown in Figure 3.4.

Our data show that stacking faults facilitate charge trapping and promote nonradiative decay, as indicated by an average on-fraction of 0.26 ( $n = 12$ ). Previous work on II–VI semiconductor quantum wells has shown that stacking faults in the material act as efficient nonradiative recombination sites,<sup>(42)</sup> and it has been postulated that the same effect should be seen in QDs and QD heterostructures.<sup>89</sup> The stacking faults we observed were at the core/shell interface for 8 of 12 QDs (75%), indicating that this defect is likely formed during growth of the inorganic CdS shell onto the CdSe core.

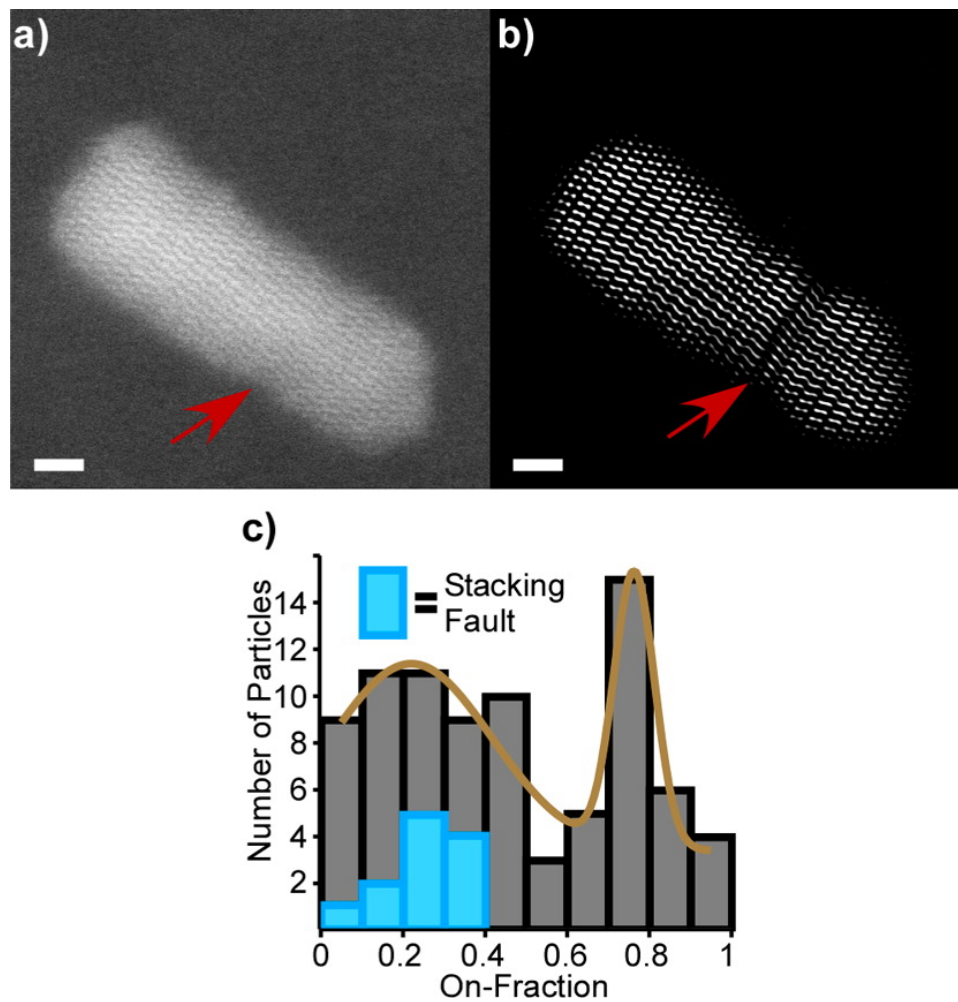


Figure 3.4: **Stacking faults inhibit single QD PL.** Shown in (a) is an example of a QD with a stacking fault. (b) The inverse Fourier transformed image demonstrates the disruption in the regular wurtzite lattice; this technique allows visualization of regular crystalline order arising from defect-free areas of the QD. (c) illustrates that all QDs with a similar visible stacking fault were observed in the LOFP. Scale bars are 2 nm.

Two morphological defect structures of individual QDs are shown in Figure 4. The first of these, pictured in Figure 3.5a, is a “pinched” shape that results from the presence of stoichiometrically distinct facets on the CdSe core:<sup>88</sup> the CdS shell grows preferentially onto the Se-rich (001) and chemically neutral (010) and (100) facets, in contrast with the ideal traditional concerted growth process that results in a contiguous shell.

The second morphological defect we took note of was the presence of a “divot” on the Cd-rich (001) surface of the QD core. This defect, which is shown in Figure 3.5b, arises due to uneven CdS shell growth: outgrowths from the Se-rich (101) facets result in the “divot” near the Cd-rich surface. This corresponds with the general trend that we observe—namely that incomplete coverage of Cd-rich facets produces QDs with a much lower on-fraction.

As shown in Figure 3.5c, the misshapen “pinched” and “divot” structures possess Cd-rich regions of the CdSe core that are exposed (not fully passivated), thereby increasing the likelihood of carrier trapping on the CdSe surface and lowering the observed on-fraction. QDs exhibiting an excessively exposed CdSe core, noncontiguous CdS shell growth, or some combination of these defects almost exclusively inhabit the LOFP, as shown in Figure 3.5d. The average on-fraction of QDs with these surface defects was 0.30 (n=31). All QDs meeting these criteria are highlighted in Appendix A.

The observed exposed Cd-rich core regions are not necessarily fully bare. Likely, there are passivating ligands on the surface of both the core and shell. These ligands, while effective at passivating some surface defects such as dangling bonds, are less photostable than an inorganic shell, and are not effective at eliminating vacancies at the surface of the core.<sup>90</sup> This can be seen by comparing the blinking behavior of QDs with no inorganic shell to nonblinking QDs with rationally designed gradient and thick inorganic shells.<sup>68,69</sup>

The traps formed at the surface of the CdSe core could be either shallow or deep surface traps due to vacancies, surface oxidation or dangling bonds.<sup>91</sup> In fact, it has recently been proposed that surface vacancies, if unpassivated, can atomically rearrange to transition from shallow to deep traps. This change would occur via charging of the QD, or even as a

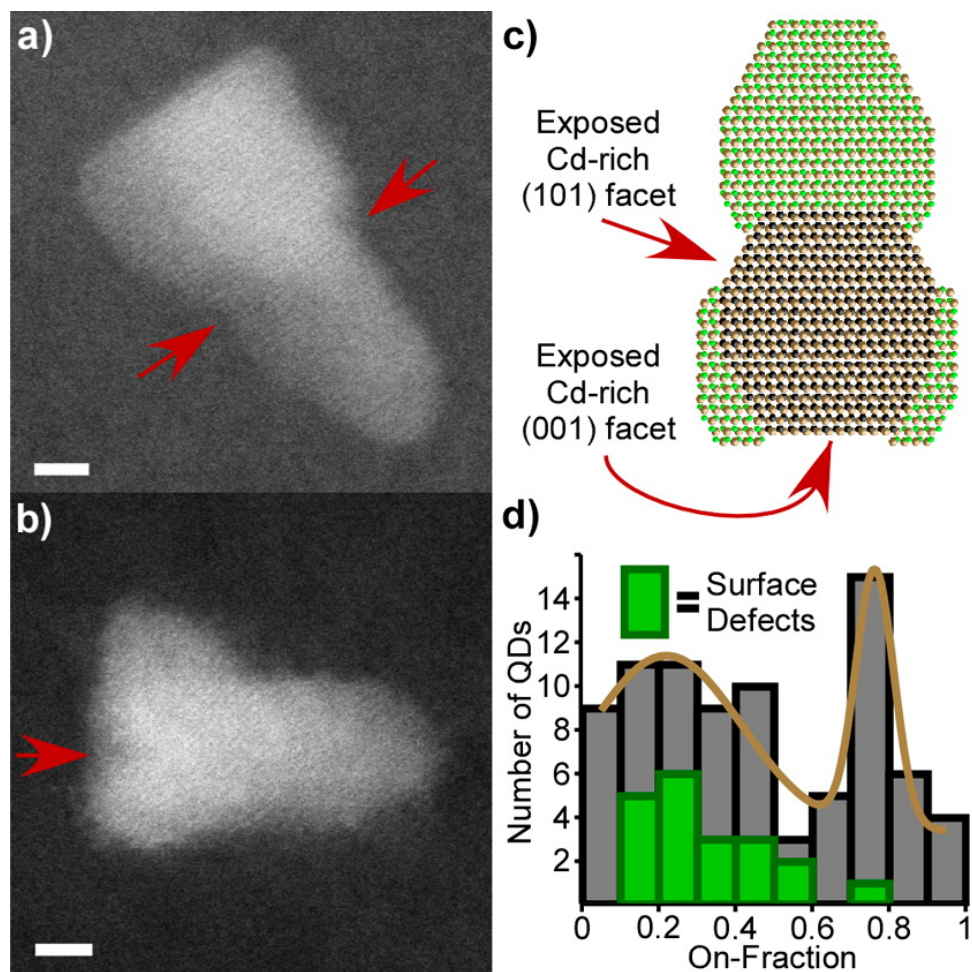


Figure 3.5: **Characteristic defects for QDs with a low on-fraction.** An example of a QD exhibiting a “pinched” shape is shown in (a), and an example of irregular shell growth at the base of a bullet QD is shown in (b). Highlighted on the representative QD structure in (c) are Cd-rich facets onto which lack of shell growth results in a lower on-fraction. These defects limit the on-fraction of QDs possessing them, as shown in the overlaid histogram in (d). Scale bars are 2 nm.

result of photoinduced surface rearrangement.<sup>90,92</sup> Our group has experimentally observed electron beam induced surface rearrangement, and similar results could be expected for single QD photoexcitation.<sup>87,93</sup>

For CdSe nanocrystals, shell material tends to favor nucleation and growth from the Se-rich (001) facet. The faceting of the wurtzite cores used for these commercial QDs results in the “bullet” shape observed in the QD population studied. Although this morphology is not ubiquitous, many core/shell syntheses display preferential shell growth onto chemically distinct core facets.<sup>94</sup> For this reason, the concepts introduced herein apply to many common literature preparation methods.

### 3.5 ... And the ugly: Determination of the crystal structure of single nonradiative quantum dots

One of the unique aspects of our approach is that it facilitates investigation of the structures of nonradiative, or “dark”, QDs. In the total population, 7 of the 84 QDs observed via Z-STEM were labeled as “dark” QDs. Optical excitation of the “dark” QDs in the fluorescence microscope did not yield fluorescence at any point during the collection period. The structures of these 7 QDs are shown in Figure 3.6.

Previous studies have identified the existence of permanently nonradiative QDs,<sup>45,95</sup> and it has been speculated that a permanently dark population may be the source of low PL quantum yield (PLQY) in nonblinking QDs.<sup>71</sup> Our ability to pinpoint and directly observe the atomic structures of these QDs is unmatched, however, and will allow a more complete understanding of the array of QDs that are detrimental to ensemble PLQY.

Examination of the “dark” QD structures reveals some interesting details. The QD shown in Figure 3.6a was the only QD in this study with a visible stacking fault in the core region. This may indicate the presence of a permanent internal defect at the core surface that results in a high rate of nonradiative recombination. The QD in Figure 3.6b shows a noncontiguous, asymmetric shell growth that would be expected to provide inefficient

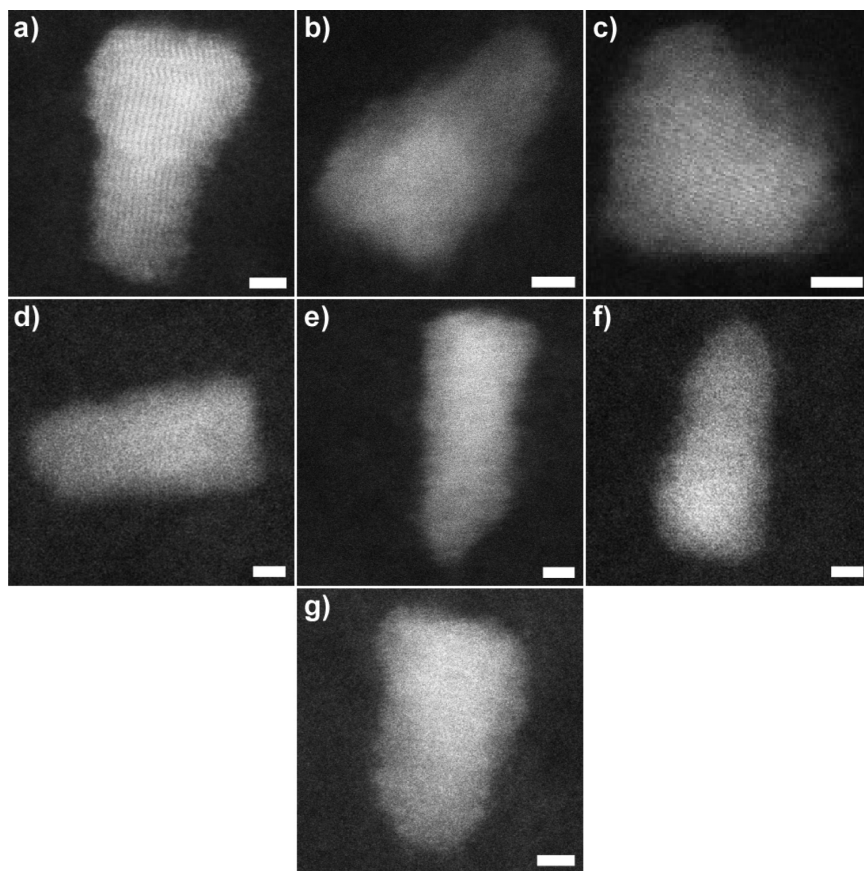


Figure 3.6: **Structures of nonradiative QDs.** Our technique affords the ability to determine the crystal structures of permanently nonradiative, or “dark”, QDs. The seven “dark” QDs identified in this study are shown here. Scale bars are 2 nm.

passivation for the same reasons outlined above for QDs in the LOFP. The QD shown in Figure 3.6c is anomalous in that it has little or no shell material grown onto the CdSe core. This QD would be excessively prone to surface oxidation and surface trap formation. The other “dark” QDs (Figure 3.6d-g) do not show egregious surface or internal defects. This indicates that perhaps there is some nonstructural explanation for a lack of PL in QDs—perhaps having to do with the dielectric environment or external traps on the substrate. More likely, “dark” QDs could arise due to features that cannot be resolved *via* electron microscopy, such as fine surface defects and organic ligand coating. Future studies will add to the library of “dark” QD structures, and will allow us to determine any existing structural motif among these QDs.

## 3.6 Other results

### 3.6.1 Length vs. on-fraction

One aspect of heterogeneity that we undertook to study was QD size and its effect on PL intermittency. All cores possess a similar size; therefore length is a good indicator of the amount of shell material grown onto the face of the QD. We found the length of QDs has no effect on the amount of time spent in the “on” state (Figure 3.7). This contrasts with previous reports that the ensemble PLQY of anisotropic core / shells decreases with increasing aspect ratio for anisotropic core / shells,<sup>96</sup> although a direct comparison between QD on-fraction and ensemble PLQY for these different syntheses would probably be facile. We notice that, within the same as-synthesized QD batch, once the native QD surface is passivated by a few monolayers of CdS, further growth of the shell does not result in more efficient confinement of charge carriers to the core. Only by passivating all surfaces without introducing defects can nonradiative processes be quenched.

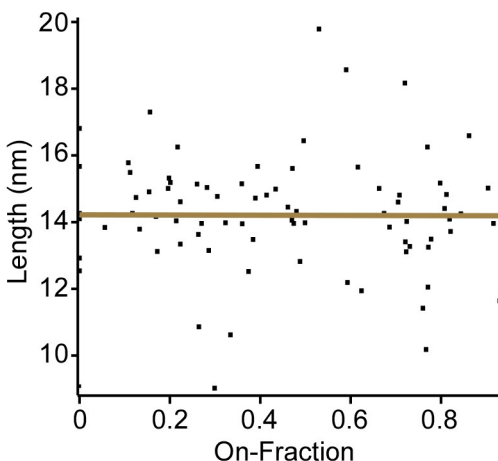


Figure 3.7: **Length vs on-fraction.** A graph of length vs on-fraction demonstrates that the total amount of shell material is less important for reduced blinking than efficient passivation of CdSe surfaces. A line with a slope of  $m=0$ , shown in gold, illustrates the lack of dependence of on-fraction on the length of the QD.

### 3.6.2 Probability distributions of “on” and “off” times

We noted no correlation between inverse power law parameters and QD structure, although a future study aimed at investigating this relationship would be very useful.

The longest “off” (“on”) times we observed were typically on the order of 100-200 seconds. Therefore, our measured “off” (“on”) times were never more than 10% of the total collection time of the experiment (2000 seconds). We chose a collection time of 2000 seconds to prevent potential bias of QD on-fraction measurements toward longer “off” (“on”) times. Previous analyses have indicated that this collection time is suitable for acquisition of blinking events to allow for analysis and determination of inverse power law parameters  $m$ ,  $\tau_{\text{on}}$ , and  $\tau_{\text{off}}$ .

### 3.6.3 Statistical certainty of subpopulation assignment

Because three QDs were assigned to the HOFP for each of the subpopulations categorized as “Perpendicular  $C_{3v}$  axis” and “101 Growth Direction,” it is reasonable to question whether the QDs in these subpopulations could have appeared in the HOFP by chance. For

both QD populations, the probability that all three QDs are in the HOFP by chance is given by:

$$P_{HOFP} = \left( \frac{\#QD_{SHOFP}}{\#QD_{total}} \right)^{\#QD_{subpopulation}}$$

Which, for both subpopulations, becomes:

$$P_{HOFP} = \left( \frac{26}{84} \right)^3 = 3\%$$

### 3.7 Conclusions

The presented correlation technique allowed investigation of the fine structural factors that mediate QD PL. We were able to unambiguously pinpoint the effect of specific surface and internal defects on the PL of single CdSe/CdS core/shell QDs. We found that, for the investigated QDs, shell material often covers little to none of the Cd-rich (001) or (101) facets. This lack of complete coverage results in the “pinched” and “divot” morphologies that we observed to decrease the total radiative time in single QDs. We also observed that stacking faults at the core/shell interface are detrimental to efficient radiative recombination in individual QDs. We now have direct evidence of what has previously been suspected: Cd-rich surface sites act as physical trap sites and the presence of a stacking fault at the core/shell interface enhances nonradiative recombination.

We also observed that suppressed blinking in anisotropic QDs can arise due to both orientational and structural factors, as illustrated by the suppressed blinking observed for all QDs oriented with the  $C_{3v}$  axis perpendicular to the substrate. The contrast between different observed morphologies in the studied QD sample is summarized in Figure 3.8. The correlation also identifies structures of QDs in the permanently nonradiative “dark” fraction; the information learned about these structures can be used to eliminate the “dark” QDs, thereby increasing ensemble PLQY. In the future, examination of heterogeneity within a population of isotropic QD heterostructures made with spherically faceted cores will be

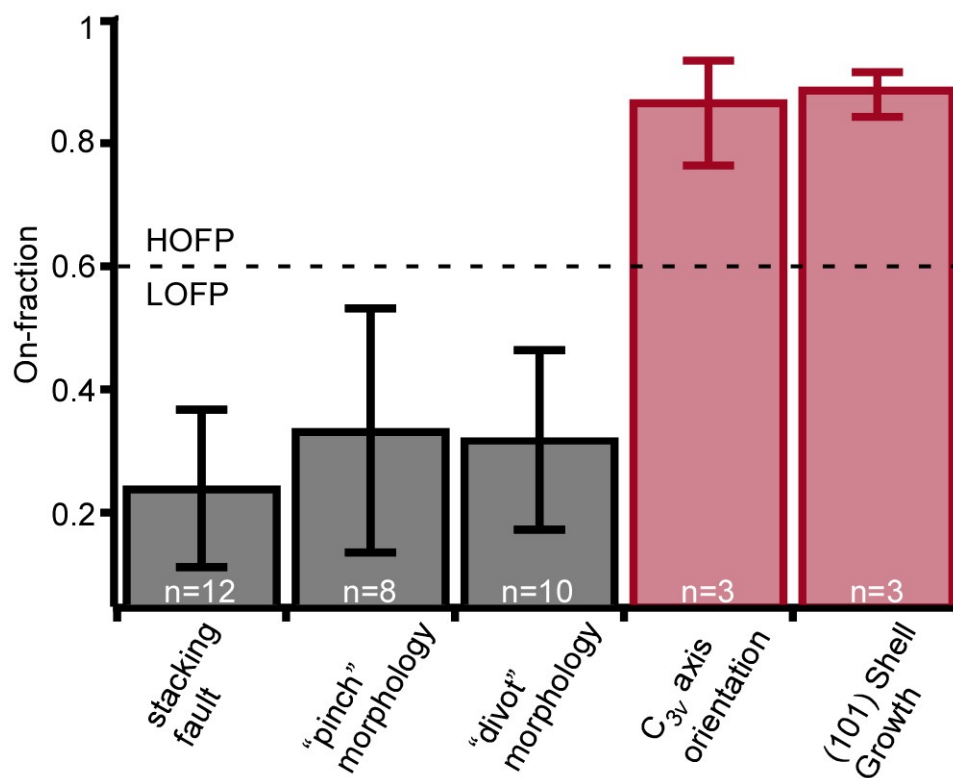


Figure 3.8: Morphologies and orientations of QDs in the high and low on-fraction populations.

useful in further elucidating ideal structures for designer QD emitters.

Ultimately, our correlation technique can be expanded to determine the structure dependence of a vast array of optical parameters. These include single QD spectra, spectral diffusion,<sup>97</sup> biexciton quantum yield, blinking frequency, and both excitonic and biexcitonic PL lifetime. Polarization dependence of PL behavior can also easily be examined, as dipole orientation is readily identified *via* electron microscopy. We believe that the use of this correlated characterization tool will facilitate rapid synthetic enhancement of desired QD properties for less developed, emergent QD systems.

## Chapter 4

### Nanocrystal-to-Nanocrystal Quantum Yield Heterogeneity and the Lack of a “Dark” Fraction in Nonblinking “Giant” Quantum Dots<sup>†</sup>

Physical variations in colloidal nanostructures give rise to heterogeneity in expressed optical behavior. This correlation between nanoscale structure and function demands interrogation of both atomic structure and photophysics at the level of single nanostructures to be fully understood. Herein, by conducting detailed analyses of fine atomic structure, chemical composition, and time-resolved single-photon photoluminescence data for the same individual nanocrystals, we reveal inhomogeneity in the quantum yields of single nonblinking “giant” CdSe/CdS core/shell quantum dots (g-QDs). We find that each g-QD possesses distinctive single exciton and biexciton quantum yields that result mainly from variations in the degree of charging, rather than from volume or structure inhomogeneity. We further establish that there is a very limited non-emissive “dark” fraction (<2%) among the studied g-QDs and present direct evidence that the g-QD core must lack inorganic passivation for the g-QD to be “dark”. Therefore, in contrast to conventional QDs, ensemble photoluminescence quantum yield is principally defined by charging processes rather than the existence of dark g-QDs.

---

<sup>†</sup>The contents of this chapter are taken from the manuscript *Quantum Yield Heterogeneity Among Single Nonblinking Quantum Dots Revealed by Atomic Structure-Quantum Optics Correlation* by Orfield, N.J., McBride, J.R., Wang, F., Buck, M.R., Keene, J.D., Reid, K.R., Htoon, H., Hollingsworth, J.A., and S.J. Rosenthal. At press time, the aforementioned manuscript was in revision at *ACS Nano*.

#### 4.1 The need for complete correlation of single colloidal quantum dot atomic structure, spatially resolved chemical composition, and single-photon photoluminescence behavior

In colloidal quantum dot (QD) heterostructures, dissimilarity in physical structure and morphology is intimately tied to electronic structure variations that have a profound influence on the expressed absorption and emission properties.<sup>78</sup> At the same time, commercial prospects for QDs are expanding rapidly, with successful incorporation of QDs into LEDs,<sup>98</sup> displays,<sup>60</sup> lasers,<sup>99</sup> and sensors.<sup>18</sup> Single QDs are also intriguing for use as single photon emitters,<sup>47</sup> entangled photon-pair emitters,<sup>32,100</sup> and biological labelling agents.<sup>101</sup> Despite the pronounced rise in efficiencies and availability of QD-based devices, much about the fundamental physics of QDs is still unknown—specifically, regarding the effects of atomic-scale defects and inhomogeneities on the expression of photoluminescence and absorption.<sup>77,102</sup> This fundamental understanding is crucial at the current stage of colloidal QD development.

Ensemble measurements, while informative, fail to provide insights into the effects of fine structural variance on photophysical properties. Single QD spectroscopy has been incredibly useful in elucidating the nature and mechanism of, for example, single QD photoluminescence intermittency,<sup>40,41</sup> and studies incorporating correlation of single QD photoluminescence data with structural measurements from atomic force microscopy (AFM)<sup>45</sup> and transmission electron microscopy (TEM)<sup>80,81</sup> have proven informative. However, AFM fails to provide detailed structural information such as lattice defects and shell epitaxy, while TEM has these same drawbacks accompanying a difficult correlation procedure that struggles to produce ambiguous identification of the same QD because of the low contrast of the electron microscopy method.<sup>81</sup> A comprehensive description of the effects of size, shape, and structural inhomogeneities—a feat beyond the reach of conventional AFM and TEM correlation—is imperative in order to understand the underlying physics inherent in QD optical expression.

When a QD is struck by a laser pulse, the probability of a photon being absorbed is directly related to the size of the QD. Further, the fate of an exciton generated within the QD is dictated by the electronic environment, which is highly dependent upon the physical properties of the QD. The core size is the best known physical parameter on which electronic structure depends—the larger the core, the lower the energy of photons that are able to be absorbed and emitted. There are, however, many other physical parameters that directly influence the energy and characteristic time in which the exciton radiatively recombines. For example, structural defects can induce nonradiative recombination, which competes directly with radiative emission as a potential outcome of exciton formation.<sup>102</sup> Therefore, studying exciton outcomes in single QDs as a function of structural and morphological differences provides insight into the charge transport properties and energy conversion efficiency of films and arrays made from colloiddally synthesized QDs.

Recently, we achieved correlation of time-resolved photoluminescence data with atomic structure in commercially available core/shell QDs.<sup>102</sup> This correlation allowed an understanding of the delicate effects—on a single QD basis—of defects, crystal structure and shell epitaxy on the photoluminescence behavior of individual QDs. Herein, we extend this approach to “giant” CdSe/CdS core/thick-shell quantum dots (g-QDs)<sup>68,71,103</sup> to address outstanding issues pertaining to their unique photophysical properties. g-QDs exhibit suppressed blinking behavior on the single-dot level, and also show significantly reduced Auger recombination rates due to the presence of a thick CdS shell.<sup>51</sup> Intriguingly, although essentially complete suppression of blinking has been recently realized for this system,<sup>71,103</sup> ensemble quantum yields have generally remained well below unity. Previous work has suggested that a non-emissive “dark” fraction may be contributing to sub-optimal quantum yields;<sup>104</sup> however, in that case the non-blinking fraction had also not been optimized, leaving open the challenge to reconcile a fully non-blinking behavior with relatively low QYs (<50%). In this study, we determined the chemical composition of the same individual QD heterostructures for which we had previously acquired extensive

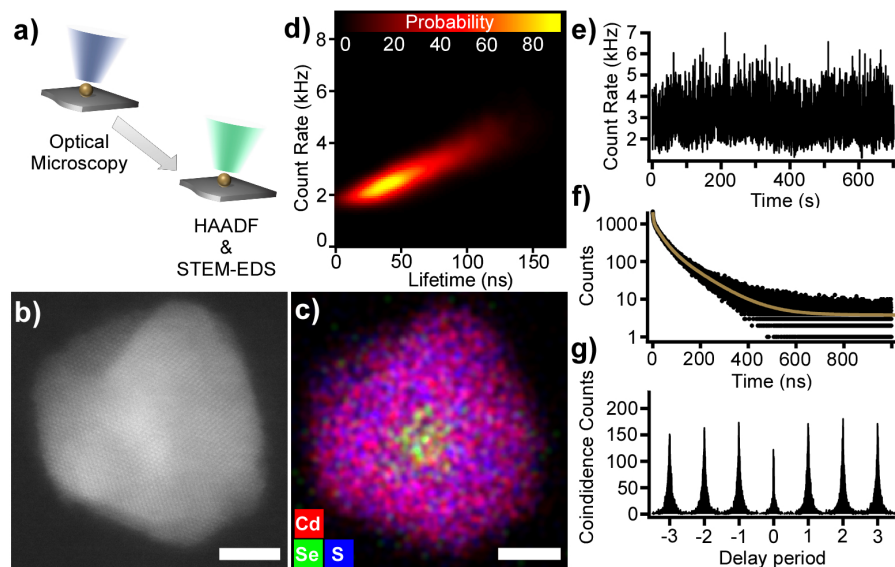


Figure 4.1: **Acquisition of optical, structural and chemical data for a single colloidal quantum dot.** (a) An individual quantum dot is located on a  $\text{SiO}_2$  substrate and sequentially imaged via optical spectroscopy and high-resolution electron microscopy according to a previously published method.<sup>102</sup> The measurable parameters from the very same single colloidal quantum dot include (b) fine atomic structure, (c) spatially-resolved chemical composition, (d) fluorescence-lifetime intensity distribution plots (FLIDs), (e) photoluminescence time trace, (f) photoluminescence lifetime, and (g) second-order fluorescence intensity correlation ( $g^{(2)}$ ). The location of the CdSe core can be determined from the EDS mapping trace of selenium in (c). Because the lifetime and intensity of the QD photoluminescence varies over time, both are calculated for each time bin (every 100 ms); plotting the lifetime vs intensity for each bin provides a 2D heatmap histogram (d) that facilitates visualization of exciton dynamics over long time scales. Probability in (d) reflects the likelihood of the QD to emit from a specific correlated lifetime-intensity state. Scale bars in (b) and (c) are 5 nm.

photoluminescence data, as shown in Figure 4.1a.

In the past, usage of high angle annular dark field (HAADF) detection on a scanning transmission electron microscope (STEM) (Figure 4.1b) has allowed for identification of core location via differential contrast based upon atomic number.<sup>52</sup> However, when studying bulkier structures than traditional core/shell nanocrystals, such as the g-QDs studied here, the large shell volume inhibits the sensitivity of HAADF to determine the location of higher atomic number elements within the heterostructures. Additionally, because HAADF intensity is indicative of both atomic number contrast and sample thickness, implementa-

tion of HAADF imaging to locate cores in core/shell QDs is a somewhat qualitative exercise. For this study, we have used STEM paired with energy dispersive x-ray spectroscopy (STEM-EDS, Figure 4.1c) to provide a much more complete picture of the chemical structure of the QD. This measurement allows visualization of QD-to-QD variations in location of the CdSe core. The minimum observable distance between the core and the surface of the g-QD heterostructure can then be correlated to specific PL behaviors. With our expanded correlation toolset, we are able to probe the relationship between a plethora of parameters, including core location (via single-QD STEM-EDS), surface roughness (via 2D perimeter), absorption cross-section, PL intensity time trace (Figure 4.1g), PL radiative decay lifetime (Figure 4.1f), and second-order fluorescence intensity correlation ratio  $g^{(2)}$  (Figure 4.1g). We can also record the trajectory of both PL lifetime and PL intensity over time. These parameters can then be histogrammed to provide insight into changes in the exciton recombination pathway as a function of time, as demonstrated in the fluorescence lifetime intensity distribution in Figure 4.1d. The  $g^{(2)}$  measurement (Figure 4.1g) indicates the likelihood of biexciton emission from a single quantum dot after biexciton formation due to a single laser pulse.<sup>32</sup> Any time two photons are sequentially emitted after excitation by one pulse, a count is registered around the zero-time delay peak. Therefore, the area ratio of the center peak to any of the side peaks of  $g^{(2)}$  is typically used as a means to measure biexciton quantum yield relative to that of single exciton quantum yield (BXQY/SXQY). This measurement also provides a good indication of the ability of a QD to emit radiatively under high pump fluence (when biexciton formation is more likely) and has been shown to be heterogeneous among as-synthesized QD samples—making study of structural dependence vital to QD development.<sup>29,100</sup>

Although g-QDs are non-blinking (100% nonblinking fraction, see Appendix B), they still exhibit intensity variations in average PL intensity from dot to dot. Without a structural correlation, these emission variations could reasonably be attributed to corresponding variation in the volume of single g-QDs. Because the volume (and absorption cross-section) of

g-QDs changes substantially with as little as a single-monolayer of variation, the heterodispersity of g-QDs demands single QD QY measurements in order to understand if variations in emission intensity are due to changes in single QD QY or changes in QD size. Here, we have used intensities acquired from HAADF-STEM to facilitate precise determination of the absorption cross-section for every individual QD on which we performed single QD spectroscopy. This measurement, along with measured photoluminescence (PL) intensity, was used to determine the QY of each g-QD relative to all other QDs.

#### 4.2 Correlation of atomic structure and photoluminescence for g-QDs

The correlated PL and STEM images for a population of QDs on one TEM support film window are shown in Figure 4.2. Figure 4.2a shows the raster-scanned PL image taken with the single nanocrystal fluorescence microscope at Los Alamos National Laboratory. The reflection of the excitation beam off of the SiO<sub>2</sub> substrate can be seen in the upper right and lower right corners of this image, while the PL from the polystyrene latex beads that were used to localize the same QDs later in STEM can be seen in the middle right of Figure 4.2a.

The collage of the correlated STEM images at low magnification is shown in Figure 4.2b. Single QDs are marked with similar red circles and lines for ease of identification of the same areas on the fluorescence image and electron micrograph. The scale bar is 2 μm.

#### 4.3 Time-correlated single photon counting for improved description of single quantum dot photoluminescence

After preparation, the support film was placed, face-down, on a No. 1 glass cover slip. The sample was then imaged by raster scanning with a 405 nm pulsed excitation source (PicoQuant PDL; 30 ps pulse width, 2.5-10 MHz repetition rate). This setup has previously been described in full detail.<sup>105</sup> The repetition rate was chosen to ensure that the PL lifetime trace decayed fully before the arrival of subsequent pulses. Excitation and collection of emission occurred through an oil-immersion Olympus objective with N.A. of

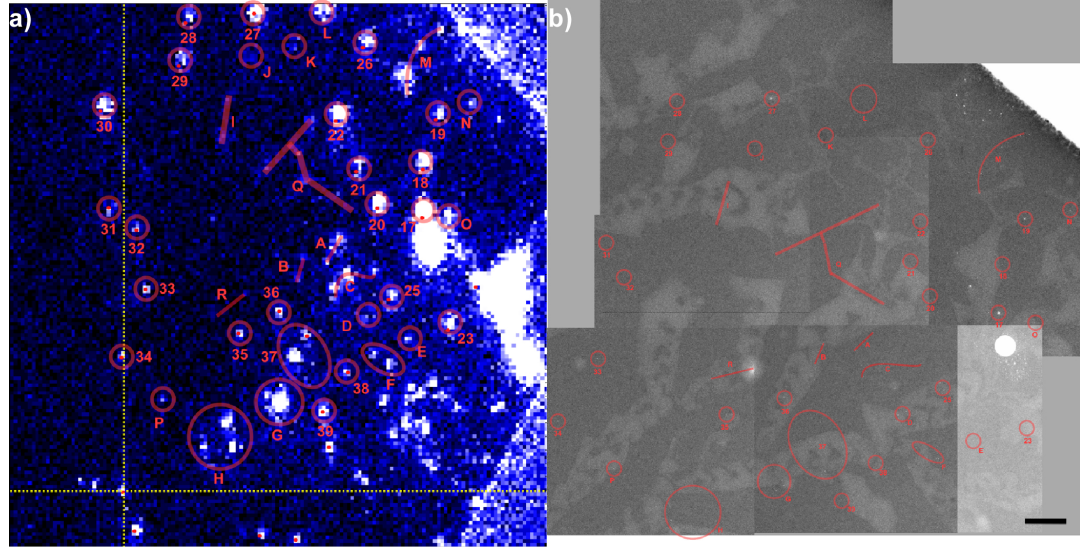


Figure 4.2: **Correlation of confocal raster scanned fluorescence and atomic structure for individual quantum dots.** The image obtained on the raster-scanning fluorescence microscope (a) g-QDs can be identified as bright white pixels on the STEM image. The presented STEM image is a composite of many high magnification STEM images. (b) corresponds to the area imaged by STEM. The large patterns in the STEM image are a product of the film manufacturing process.

1.3. The emitted photons were collected onto two avalanche photodiodes (APDs; SPCM-AQRH-14, Perkin Elmer) in a Hanbury-Brown Twiss interferometric configuration. We verified that, for all QDs studied, the number of excitations per pulse  $\langle N \rangle$  was less than 0.2. This was done according to a previously established method of measuring  $\langle N \rangle$  as a function of excitation intensity.<sup>105</sup>

Homebuilt software was used to perform all analysis of photoluminescence data and generate FLIDs.

#### 4.4 Single quantum dot energy dispersive x-ray spectroscopy

After all relevant photoluminescence data had been collected, support films were stored in a grid holder until electron microscopy could be performed. Scanning transmission electron microscopy images were obtained using a Tecnai Osiris operating at 200 kV, with a spot size set to 10 (to reduce charging effects) and a camera length of 220 mm for HAADF

imaging. HAADF-STEM imaging was chosen over HRTEM imaging since the white-on-dark-contrast for STEM greatly facilitates the location of individual quantum dots at low magnifications. Patterns of polystyrene were used to align the STEM image and distances measured from the optical microscope were used to identify regions of interest. Large area STEM images were used to identify neighboring particles and possible dark particles. After obtaining a high resolution STEM image of a particle, the spot size was lowered to 4 yielding  $\sim 1.5$  nA of beam current with a probe size on the order of  $0.5 \text{ \AA}$ . These conditions, in conjunction with a highly efficient Super-X<sup>TM</sup> EDS detection system, enabled rapid collection of EDS spectrum maps with a minimal number of scans ( $\sim 30$  seconds total acquisition time). EDS hypermaps were collected using Bruker's Esprit software.

#### 4.5 Determination of single quantum dot quantum yields via high angle annular dark field imaging

The absorption cross section is calculated according to the following modified equation:<sup>100,106</sup>

$$\sigma = V \alpha_w |f_w|^2 \frac{n_w}{n_{medium}} \quad (4.1)$$

where  $\sigma$  is the absorption cross-section of the g-QD heterostructure,  $\alpha_w$  is the absorption coefficient,  $|f_w|^2$  is a correction factor,  $n_w$  is the refractive index of CdS,  $n_{medium}$  is the refractive index of air, and  $V$  is the rough volume of the heterostructure measured from the HAADF intensity. We approximate the value of the QD volume by setting the maximum measured HAADF density to the value of the maximum measurable two-dimensional diameter (the Feret diameter,  $R_F$ ) and calculating *via* the equation:

$$V_{QD} = A \sum \left\{ \frac{\phi_i}{\phi_{max}} \gamma R_F \right\} \quad (4.2)$$

where  $A$  is the two-dimensional projection of the area of the QD on the TEM support film in  $\text{nm}^2$ ,  $\phi_i$  is the integrated density per pixel, and  $\gamma$  is the number of pixels per  $\text{nm}^2$ . The absorption cross-section can then be used to calculate the relative QY for any given intensity using the simple relationship:

$$QY \propto \frac{I}{\sigma} \quad (4.3)$$

where  $I$  is the measured photoluminescence intensity. This allows us to determine the QY ratio of all g-QDs and normalize to the highest QY in the studied population.

For calculation of QD volume, detection of scattered electrons was presumed to scale linearly with material thickness as demonstrated previously.<sup>107,108</sup> Also, the approximation is made that QD height does not vary drastically from the width measured from 2D cross-sections. Additionally, in contrast to smaller core/shell QDs, the CdSe core here accounts for <5% of the total heterostructure volume. Because the intensity contrast of the HAADF varies nonlinearly as a function of atomic number  $Z$  ( $I \propto Z^\alpha$ ), where the variable  $\alpha$  is always <2,<sup>107</sup> any overestimation in the QD volume due to atomic number contrast difference between CdSe and CdS would be <2% and within the error of the instrument. Therefore, a correction factor for variable atomic number contrast was deemed unnecessary.

#### 4.6 Quantum yield heterogeneity and the lack of a “dark” fraction

For this study, we examined 24 individual g-QDs from the same synthetic batch. Full details on synthesis are available in Section 4.1. The QY distribution of this sample is shown in Figure 4.3a—it is apparent from this plot that there was an inherent inhomogeneity in the distribution of single QD QYs.

The average of the QYs that were measured was 43%. It is important to note that the QYs presented here are relative, and the QD assigned a QY value of 1 likely possessed a value somewhat smaller than unity. Therefore, the 43% value is a slight overestimate of the

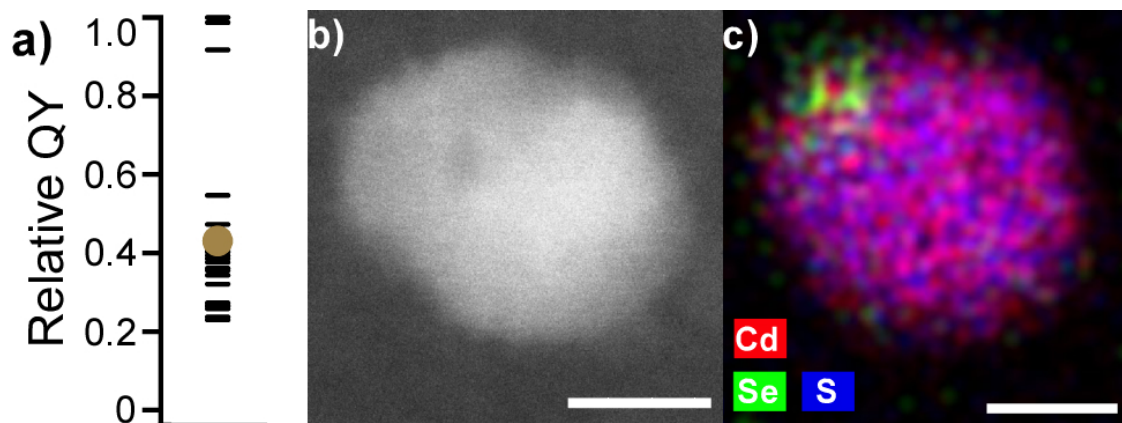


Figure 4.3: **Quantum yield heterogeneity among single nonblinking QDs.** (a) The g-QDs display a heterogeneous distribution of single-QD quantum yields. The gold point represents the mean of the single-QD measurements. (b) HAADF / EDS overlay of the single nonemissive dot found in the examined sample. This particle was the lone g-QD with an exposed (unpassivated) CdSe core, as demonstrated in the EDS map. On the whole, we find that QY heterogeneity, and not a significant “dark” fraction, accounts for the measured ensemble PLQY. Scale bars are 5 nm.

mean QY expressed by single QDs. As a result, the calculated ensemble g-QD QY via an arithmetic average of single-QD QYs is internally consistent with the measured ensemble QY in solution ( 30%).

This observation became more intriguing when searching for “dark” QDs. Previous studies of traditional QDs have demonstrated that a “dark fraction” of permanently non-radiative QDs contributes negatively to ensemble QD photoluminescence (PL).<sup>45,95</sup> In the past, we have shown the unique ability to probe the precise atomic structure of “dark” QDs.<sup>102</sup> With this in mind, we set out to determine a unique structural motif among “dark” QDs in the overall g-QD population. To aid in the investigation of the “dark” fraction, a g-QD sample was chosen that exhibits good nonblinking PL behavior on the individual QD level, but an ensemble photoluminescence quantum yield (PLQY) of  $\sim 30\%$ . For the purpose of examining this “dark” fraction, the sample size was expanded to  $>50$  QDs using wide-field fluorescence microscopy at Vanderbilt; in total, only 1 g-QD was observed to be permanently nonradiative, and it had an unpassivated CdSe core (Figure 4.3b and 4.3c). A sample image from the search for “dark” QDs is shown in Figure 4.4.

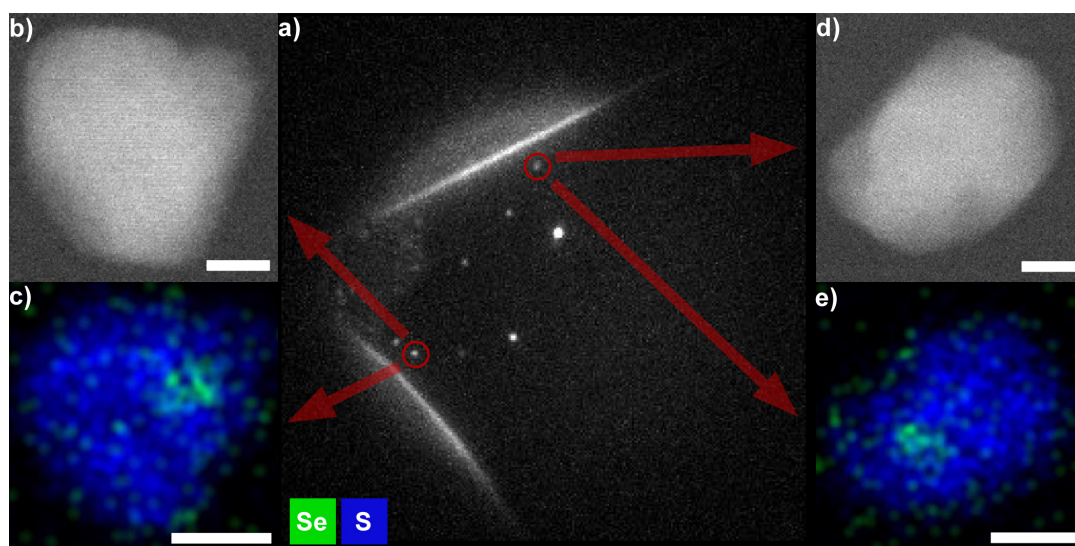


Figure 4.4: **Correlation of wide-field fluorescence and atomic structure.** These data were acquired in the search for “dark” g-QDs. (a) An optical image taken with wide-field excitation. The edge of the TEM support film window can be seen in the fluorescence image, and a structure of polystyrene latex spheres that was used for correlation is located in the middle left area of the image. (b) - (d) Crystal structures and EDS maps for individual QDs found on the TEM grid. Through this search, it was found that only  $\sim 2\%$  of QDs in the examined were “dark,” contrary to previous study of g-QD samples. Scale bars in (b)-(d) are 5 nm.

In light of these results, the measured ensemble QY ( $\sim 30\%$ ) is attributed to variation in the single-QD QY, and not to the presence of a large “dark fraction” of QDs. The lack of a substantial population of “dark” QDs is notable—this observation runs contrary to those made by several groups in the past in work on traditional QDs.<sup>45,95</sup> More broadly, we have determined that in order for a QD to be in the “dark” population, some portion of the CdSe core must be unpassivated by the shell material—an assertion that is supported by previous study.<sup>55,102</sup> This would explain the presence of only one observed “dark” g-QD; the large successive ionic layer adsorption and reaction (SILAR) grown CdS shell provides complete surface passivation of the CdSe core for nearly every studied QD.

#### 4.7 Single quantum dot quantum yield “pinning”

Notably, three of the g-QDs had a remarkably high QY when compared to the rest of the sample, as can be seen in Figure 4.3a. On the other hand, Figure 4.3a also demonstrates that the QY of the remaining individual g-QD population is much lower, and varies from QD-to-QD. As an explanation for this single-QD QY variation, we attempted to implicate a specific structural factor via analysis of QD structure. There is, however, no observed relationship between structural properties and QY, as shown in Figure 4.5. Additionally, visual inspection of individual g-QDs did not reveal specific morphological or structural features that are tied to high single-QD QY.

It is important to note that none of the g-QDs with non-unity average QY has a maximum single-QD QY near-unity. As shown Figure 4.6a, the average QY (determined from the integrated single-QD photoluminescence intensity) is intimately tied to the maximum measured QY (determined from the maximum single-bin photoluminescence intensity).

This QY pinning phenomenon indicates that any nonradiative process suppressing the single-QD QY is occurring on a time scale much faster than the 100 millisecond binning time, leading to an apparent QY that shows little temporal variance over the entire acquisition time (always  $\geq 300$  seconds). Additionally, we found that QDs with high single-QD

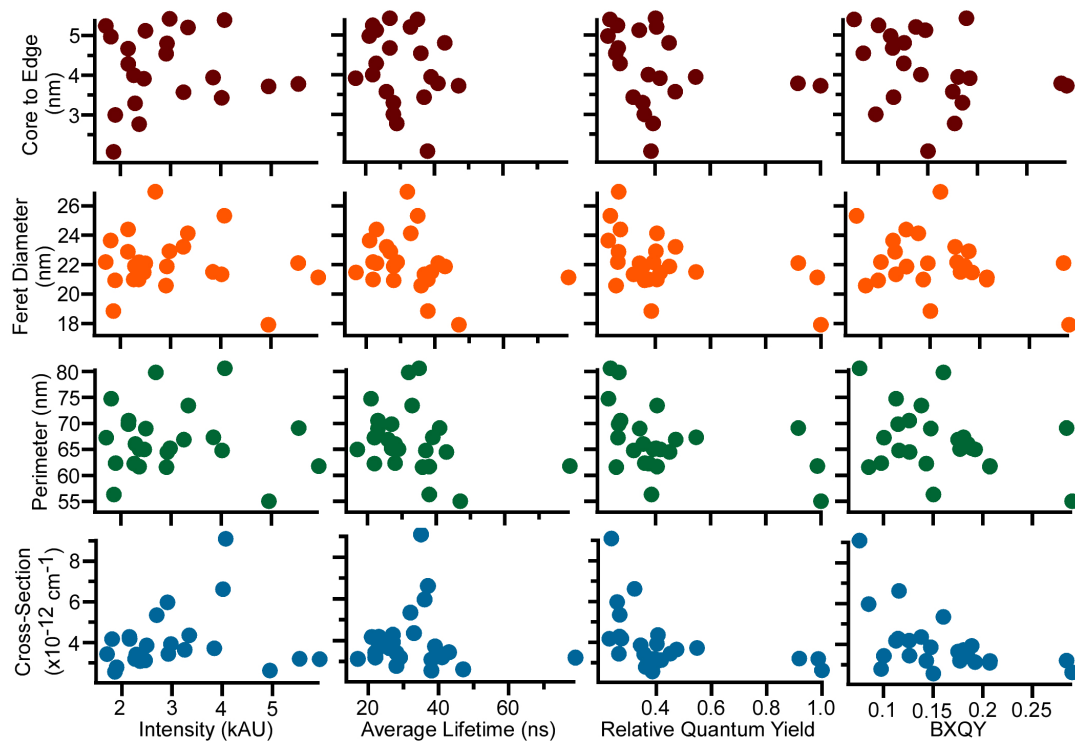


Figure 4.5: **Optical vs physical parameters for studied quantum dots.** Shown is a plot of assorted physical parameters vs assorted photoluminescence features for 24 individual g-nQDs.

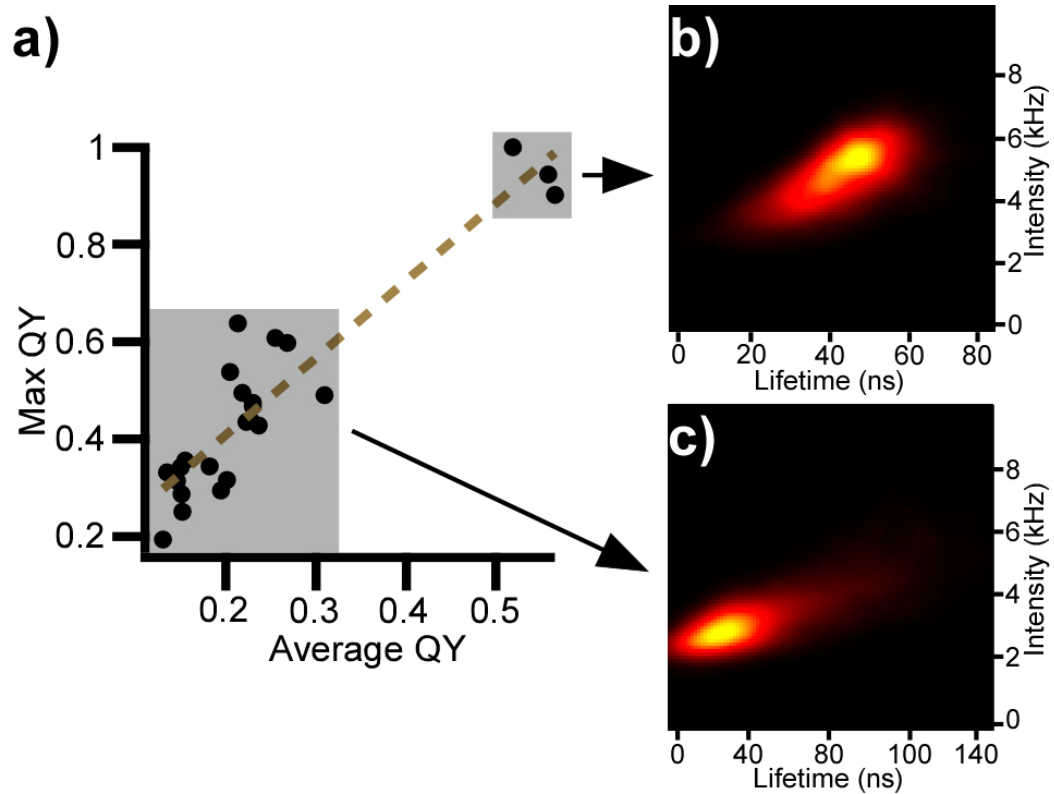


Figure 4.6: **Quantum yield “pinning” in nonblinking QDs.** (a) Single g-nQDs are “pinned” to characteristic QYs, with single particles expressing a time-invariant single QD QY over the entire PL collection period. Max QY is calculated from the highest-intensity single time bin, while Average QY is calculated from the average QD intensity over the entire collection time. (b) g-nQDs with high QY have FLIDs with tails moving toward low lifetime and low intensity, (c) g-nQDs with low QY show the opposite trend.

QY have long lifetimes and a FLID with a tail extending toward low PL intensity and short lifetime (Figure 4.6b). Meanwhile, the g-QDs with low single-QD QY show the opposite trend (Figure 4.6c).

#### 4.8 Charging as an explanation for variation of single quantum dot quantum yield

To assist in determination of the underlying cause for the QY heterogeneity, we performed intensity-discriminate  $g^{(2)}$  analysis on a g-QD from each of the high- and low-QY subsets. This analysis allows determination of the  $g^{(2)}$  value for different intensity levels of the photoluminescence time trace, and has previously been shown to provide information about the charge state of a QD.<sup>109</sup> The structures and optical analyses of the high- and low-QY g-QDs are shown in Figure 4.7.

The  $g^{(2)}$  spectra and corresponding global fits that were used to determine values of BXQY/XQY ratio are shown in Figure 4.8.

The high-QY g-QD possessed a low overall  $g^{(2)}$  value and no intensity-dependent  $g^{(2)}$  behavior, indicating that the BXQY/SXQY ratio was constant over all measured intensities (Figure 4.7e and 4.7g). Meanwhile, the low-QY g-QD showed a high  $g^{(2)}$  value, but a marked variation of  $g^{(2)}$  with intensity (Figure 4.7f and 4.7g). Based upon a previously-established precedent, which showed that charged QDs have a drastic level of  $g^{(2)}$  variation with PL intensity but neutral QDs do not,<sup>109</sup> these results implicate single-QD charging as the source of low QY. This is corroborated by the shapes of the g-QD FLIDs (Figure 4.7c and 4.7d)—previous spectroscopic and spectroelectrochemical work has shown that a FLID with a tail rising toward high PL intensity and lifetime is indicative of a charged QD.<sup>40,105</sup> We consistently observed this FLID shape for all but the highest QY g-QDs.

The conventional g-QD charging mechanism involves the Auger ionization of a biexciton, followed by excitation with a photon to form a trion. In the CdSe/CdS system used here, the hole is more strongly confined to the core than the electron,<sup>55</sup> so Auger ionization of the hole is more likely than that of the electron. Therefore, biexciton Auger recom-

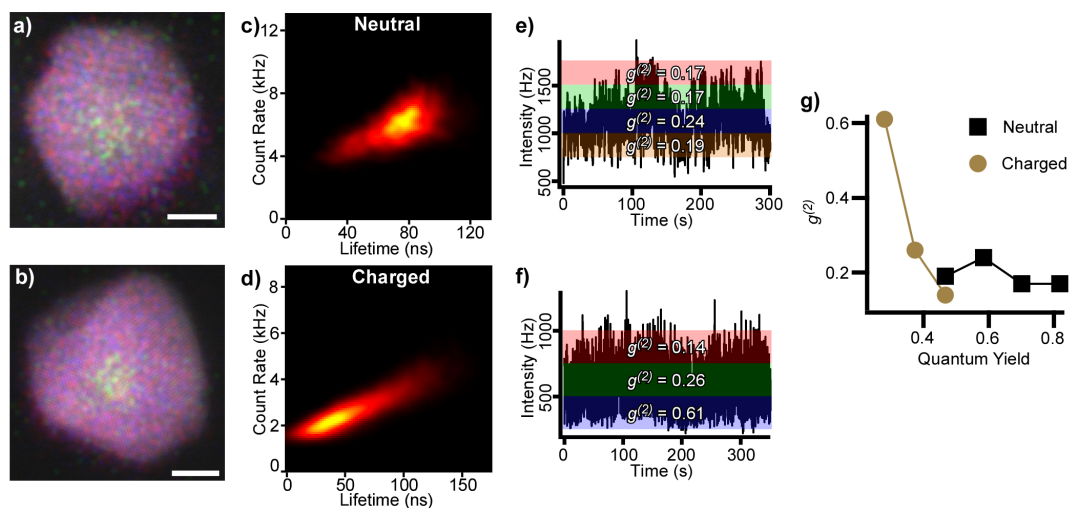


**Figure 4.7: Further analysis of the influence of charging on single-QD quantum yield.** Shown are corresponding structure / EDS map overlays (a),(b) and optical data (c)-(g) for a representative neutral (a) and charged (b) g-QD. The FLIDs indicate that the g-QDs with highest single-QD QY are neutral, while the g-QDs with heterogeneously distributed lower single-QD QYs are charged. This is confirmed by determining intensity-dependent  $g^{(2)}$  values from the photoluminescence intensity transients (e) and (f) of the two g-QDs. For plots (e) and (f), if the photoluminescence intensity of a given time bin falls within the shaded area, the photon arrival events corresponding to that bin are included in the  $g^{(2)}$  measurement. This allows us to measure the value of the second-order correlation parameter  $g^{(2)}$  for different intensity levels within the overall photoluminescence intensity transient. The  $g^{(2)}$  values of each intensity level are indicated on the corresponding shaded areas in (e) and (f), and are also plotted vs quantum yield of the corresponding intensity levels in (g). The  $g^{(2)}$  values of the neutral g-QD are constant with intensity, while the charged g-QD  $g^{(2)}$  values decrease with increasing intensity (g). Scale bars are 5 nm.

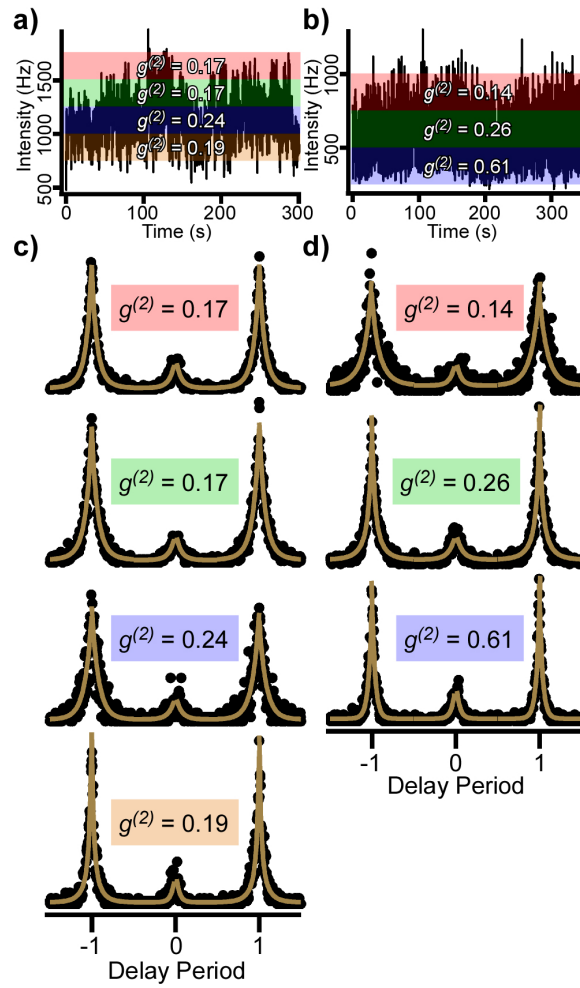


Figure 4.8:  $g^{(2)}$  fits for the QDs shown in Figure 4.7. PL intensity transience traces (a), (b), and intensity-dependent  $g^{(2)}$  fitting (c), (d) for the neutral (a), (c) and charged (b), (d) g-QD.

bination results in excitation of the hole, which can become localized in trap states on the surface of the g-QD. Upon excitation of the g-QD by the next laser pulse, a negative trion is formed.<sup>40,105</sup> The g-QD remains in this charged state, which possesses a characteristically low PL emission intensity due to competition between the radiative and nonradiative trion decay rates, until the hole recombines with the extra electron in the core. In this explanation of QD charging, the density of surface trap states determines the likelihood of charge trapping, and the depth of the respective trap state determines the amount of time the g-QD spends in the corresponding charged state. This would result in QD surface charging that would compete with excitonic recombination and reduce the overall PLQY on the single-QD level. These effects (trap density and depth) combine to dictate the overall percentage of time the g-QD spends in a charged state. This simple mechanism is illustrated in Figure 4.9.

As a result of the fast time scale of QD charging,<sup>110</sup> the measured QY for each g-QD is temporally invariable and directly related to the rates of charging and discharging for that specific g-QD. For CdSe/CdS heterostructures, charging by a lone charge carrier has been shown to result in quenching of emission intensity and reduction in fluorescence lifetime.<sup>40,65</sup> Therefore, the observed heterogeneity in the low single-QD QY g-QDs is hypothesized to be due to dissimilarity in the charging / discharging rates from QD to QD. This dissimilarity likely arises from the location as well as the nature of the trap sites on the QD.

To further confirm this hypothesis, we developed a two-state model to explain the relationship between charging and single-QD QY. In our model, the QD is fluctuating between a neutral state with 100% QY and a charged state with QY defined by the minimum measured single-QD QY. Under these assumptions, the relationship between single-QD average QY and single QD average lifetime becomes:

$$Q_{avg} = \frac{\tau_{avg}(Q_{max} - Q_{min}) + \tau_X(\frac{Q_{min}}{2})(2 - Q_{max})}{\tau_X(1 - \frac{Q_{min}}{2})} \quad (4.4)$$

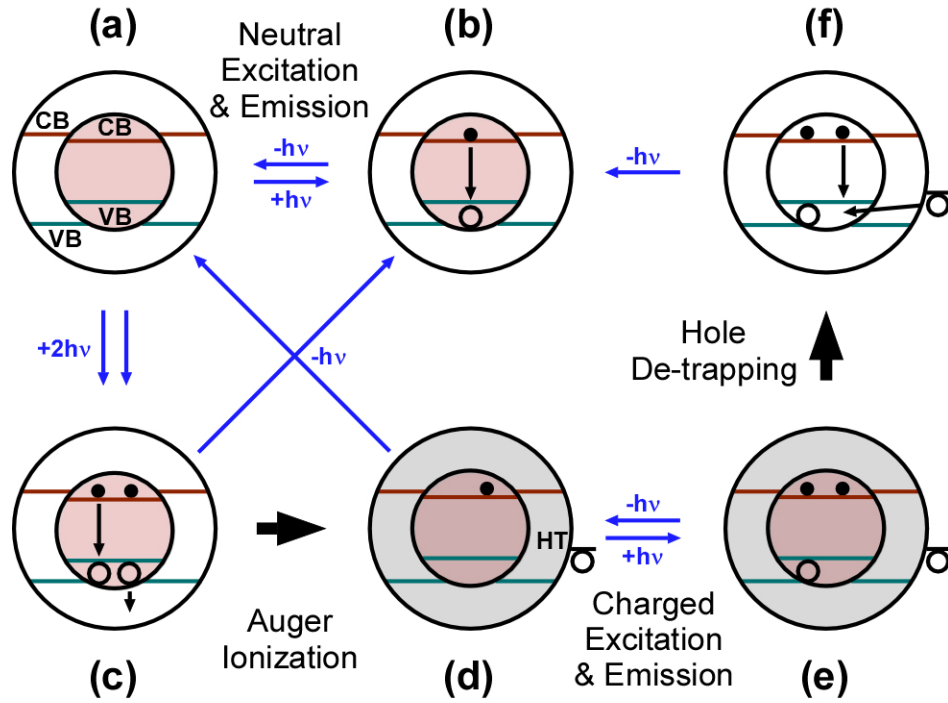


Figure 4.9: **Mechanism to describe QY heterogeneity.** (a) A single g-QD with quasi-type-II band structure. The valence band is shown as a green line, while the conduction band is indicated with a red line. When the g-QD is struck by a laser pulse, the most common outcome is a single exciton (b) that can recombine radiatively—a process that occurs with near-unity QY. Occasionally, a biexciton is formed (c); Auger ionization of the biexciton results in a negatively-charged g-QD with the hole localized in a hole trap (HT) on the heterostructure surface. After excitation, emission of this singly charged g-QD (e) occurs much less efficiently than photon emission from a neutral g-QD, reducing overall PLQY. The g-QD remains in the charged state until the hole escapes from the hole trap and recombines with the extra electron  $\{(f) \rightarrow (b) \text{ or } (d) \rightarrow (a)\}$ .

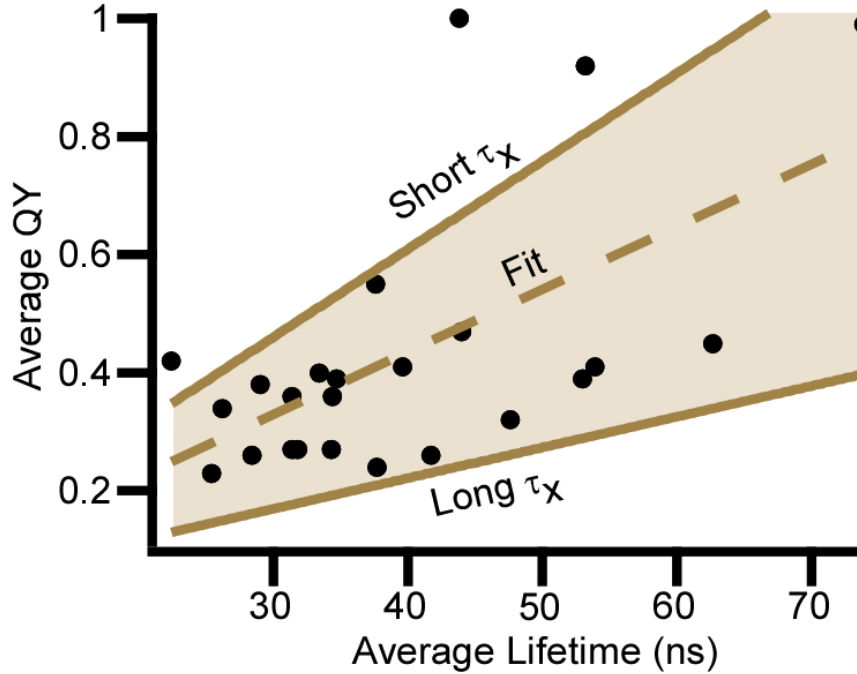


Figure 4.10: **Modeling the relationship between quantum dot quantum yield and lifetime.** Plotting average quantum yield vs average lifetime for each quantum dot reveals a linear relationship between the parameters. This linear model assumes that a single QD is in either a neutral or singly charged state. Because the neutral exciton lifetime varies between dots, an upper and lower bound corresponding to short and long neutral exciton lifetime are plotted.

where  $Q_{max}$  and  $Q_{min}$  are the single-QD QYs of the neutral and charged states, respectively,  $\tau_X$  is the neutral exciton lifetime, and  $\tau_{avg}$  is the average lifetime of the single QD (see Section 4.11 for full derivation). Figure 4.10 demonstrates the relationship between single-QD QY and  $\tau_{avg}$ .

Neutral exciton lifetime varies from QD-to-QD; for this reason the derived model is shown for a range of  $\tau_X$  varying from 66 to 189 ns, corresponding to the minimum and maximum measured  $\tau_X$  values for the investigated sample. The agreement between our single-charging model and the measured data confirms that such a model is sufficient to describe the observed variations in single-QD QY.

In previous work, we have shown that the presence of crystalline defects at the core/shell interface results in reduction of the PL “on” time of individual QDs. This phenomenon

likely occurs due to the presence of surface defects that form as a result of the stacking faults found at the core/shell interface.<sup>102</sup> In the system studied here, this type of surface defect would occur as a result of continuation of stacking faults at the core/shell interface outward to the surface, and would be expressed as a grain boundary in the thick CdS shell of the g-QD heterostructure. However, stacking faults at the core/shell interface would be difficult to observe in our HAADF images because this interface is typically obscured by the large particle volume, which lowers the chance of the nanocrystal being aligned perfectly on a zone-axis—a requirement for high resolution imaging.

In addition to the above mentioned defects, several other sources of surface defects are known which could contribute to g-QD charging, and consequently reduce the g-QD PLQY. Ligand coverage is especially important, and steric crowding at the surface of the nanocrystal can prevent complete ligand passivation of the surface.<sup>111</sup> Further, under-coordinated atoms at the surface can act as trap states that could localize charge carriers. Previous results have also shown that surface dynamics of the nanocrystal and passivating ligands can result in surface trapping;<sup>87,93</sup> this type of defect has been used to describe reduced PL emission as well as QD blinking behavior.<sup>90,92</sup> Although g-QDs benefit from a thick inorganic shell, the exciton recombination dynamics are not entirely divorced from the QD surface due to the large energy of Auger ionization; minimization of defects related to ligand coverage is key in increasing the overall PLQY by reducing g-QD charging.

#### 4.9 Implications for measurement of biexciton quantum yield

With regard to  $g^{(2)}$  measurements—as has been noted previously, the  $g^{(2)}$  value, which can be calculated as the center peak-to-side peak ratio for the second order intensity correlation histogram, is known to be equal to the biexciton quantum yield divided by the single exciton quantum yield (BXQY/SXQY).<sup>29,32</sup> Therefore, the actual BXQY value is not necessarily the same as the  $g^{(2)}$  value for the QDs studied. In the case of the g-QDs studied here, because the value of the SXQY is typically lower than 100%, the deviation of  $g^{(2)}$

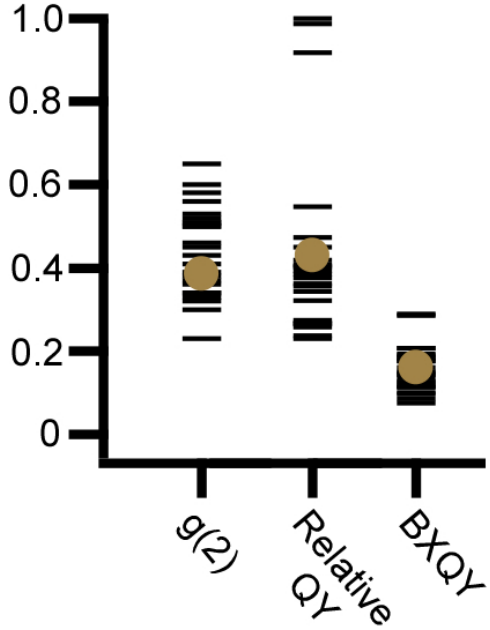


Figure 4.11: **The use of single-QD quantum yield to determine BXQY.** The  $g^{(2)}$  values measured for each QD are used, in conjunction with the measured single g-QD QY, to calculate BXQY for each QD. The tight grouping of BXQY values indicates that charging, and not BXQY variation, is the main source of  $g^{(2)}$  heterogeneity.

from BXQY is significant. When the experimentally measured single-QD QY is used to calculate BXQY according to this relationship, the average BXQY value for the observed QDs is reduced by a factor of  $\sim 2$  from the measured  $g^{(2)}$  value, as shown in Figure 4.11.

While  $g^{(2)}$  values show a wide, heterogeneous distribution, BXQY values calculated using measured QY show a very narrow distribution, suggesting that Auger suppression is quite uniform across the sample (radiative recombination from the biexciton state is similar for all g-QDs). This also indicates that observed variations in  $g^{(2)}$  are mainly a result of variation in the degree of charging in individual g-QDs, and the inherent BXQY for each g-QD is fairly constant.

#### 4.10 Entanglement in a “quantum heart”

As part of this correlated fluorescence microscopy and STEM study on g-QDs, an accidental discovery of an electronically-coupled “heart-shaped” pair of QDs (coupled QD, or CQD) within the same g-QD heterostructure was made. This structure is of great interest due to the potential for use in a variety of quantum information technologies. Specifically, CQDs are crucial for development of quantum computation due to their promise to reduce optical-electronic-optical conversion bottlenecks upon implementation into single-photon switches and routers.<sup>112,113</sup> Although CQDs have been grown epitaxially,<sup>114</sup> successful colloidal synthesis of this type of heterostructure has thus far been limited. Coupling of two colloidal QD cores could lead to entanglement generation, obviating the need for custom-growth of single epitaxial CQDs and facilitating rapid development of quantum communication technology.

The EDS spectrum shown in Figure 4.12b demonstrates that the CQD analyzed has two cores; however, on the timescale of single exciton emission, the CQD emits only one photon at a time. To determine this, a time-gated  $g^{(2)}$  method that only analyzes photons collected after 20 ns (much longer than the biexciton emission lifetime of  $\sim 5$  ns that is generally observed in “giant” CdSe/CdS core/thick-shell QDs). If antibunching is observed in photons collected in this time frame, the analyzed fluorophore is acting as a single-photon emitter. The gated second-order intensity correlation spectrum with  $g^{(2)}=0.03$  demonstrates that dipole-dipole coupling or charge transfer interactions required for the creation of entangled states occur between the two spatially separated QD cores.

Further fundamental investigation is needed to understand the nature of emission from such colloidal CQDs. A synthesis method that can lead to reliable, on-demand synthesis of such CQDs with custom-tailored physical parameters would be especially useful to the expanding field of quantum information technology.

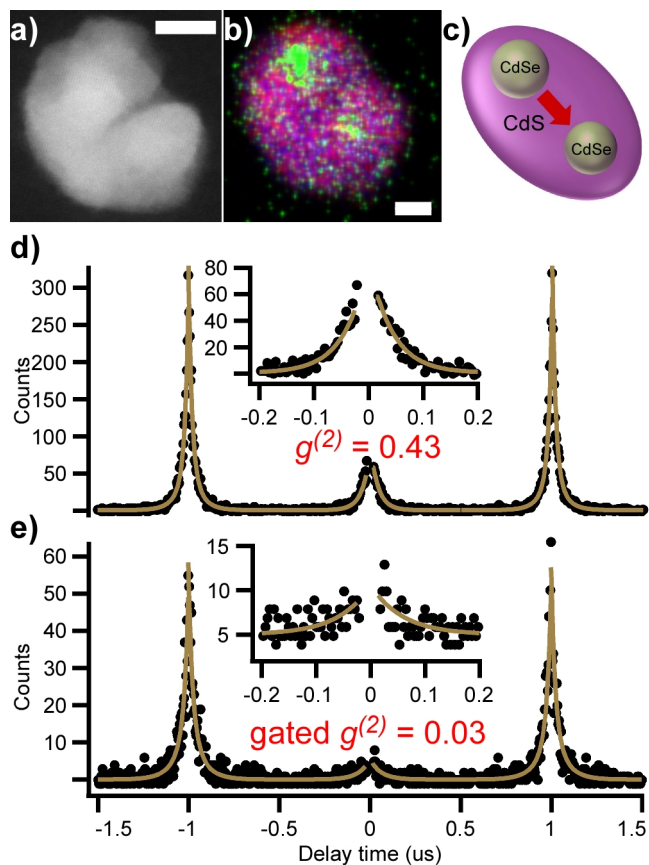


Figure 4.12: **Quantum optical signature of coupling between artificial atoms in a colloidal QD heterostructure.** Z-STEM (*a*) and STEM-EDS (*b*) of an electronically coupled pair of CdSe cores, as illustrated in (*c*). While (*d*) shows that the antibunching trace  $g^{(2)}$  has a nonzero value (0.43), this is due to high BXQY, as illustrated in the time-gated  $g^{(2)}$  spectrum shown in (*e*), which has a center peak to side peak ratio of 0.03. Insets in (*d*) and (*e*) are expanded regions of the same  $g^{(2)}$  spectrum at a delay time of  $\tau = 0$ . Scale bars are 5 nm.

## 4.11 Conclusions

Reduced PLQY is intimately linked with surface defects—and remarkably, these fine defects seem to have little to do with overall morphology of the g-QDs. Rather, such defects likely result from synthetically controllable conditions such as ligand selection, ligand ratios, shelling temperature, and the level of alloying at the core/shell interface. This would explain the recent success of, for example, high-temperature shelling procedures<sup>115</sup> and graded alloy syntheses<sup>116</sup> in obtaining high-QY QD samples.

A tandem of HAADF-STEM and PL spectroscopy has proven crucial for a comprehensive understanding of single QD photoluminescence behavior. Without this pairing, it would not have been possible to determine single-QD QY or to identify single-QD QY heterogeneity among individual nonblinking QDs. Further analysis of single-photon emission events was necessary to elucidate the mechanism by which single-QD QY is reduced—namely single-QD charging.

Our data indicate that, even within nonblinking QDs, quantum yield heterogeneity arises from charging processes that occur on a time scale much faster than is measurable using conventional single-QD photoluminescence spectroscopy. We show that such quantum yield heterogeneity can account for g-QD ensembles simultaneously characterized by moderate quantum yields yet also nearly fully nonblinking behavior. We also note that QY pinning is due to rapid charging and discharging from a singly-charged state, rather than multiple discrete charged states for individual nanocrystals—an assertion that is supported by previous research on the quasi-type-II band gap offset between CdSe and CdS,<sup>55</sup> and also by our own model.

## 4.12 Experimental methods

### 4.12.1 Nanocrystal synthesis

*Materials.* Selenium (1-3 mm shot, 99.999%), CdO powder (99.998%), and oleic acid (OLAC, 90%) were purchased from Alfa Aesar. Sulfur (99.999%), oleylamine (OLAM, C18 content 80-90%), 1-octadecene (ODE, 90%), and octadecane (OD, 90%) were purchased from Acros Organics. Trioctylphosphine (TOP, 90%) was purchased from Sigma Aldrich, and trioctylphosphine oxide (TOPO, 90%) was purchased from Strem Chemicals. All chemicals were used as received without further purification, and all syntheses were performed under Ar atmosphere using standard air-free Schlenk techniques.

*Preparation of Stock Solutions.* 0.5 M Cd(II)oleate solution was prepared by dissolving CdO in OLAC at 180 °C, followed by removal of water under vacuum at 80 °C. Similarly, 0.2 M Cd(II)oleate solutions (10:1 mol/mol OLAC: Cd<sup>2+</sup>) were prepared by dissolving CdO in a mixture of OLAC and either OD or ODE. 0.2 M sulfur solutions were prepared by dissolving sulfur powder in either OD or ODE at 180 °C. Stock solutions of trioctylphosphine-selenium complex (TOP-Se) were typically 1M, and prepared by stirring Se in TOP overnight under air-free conditions.

*Synthesis of CdSe quantum dot (QD) cores.* CdSe QD cores were prepared according to previously published literature, with slight modifications.<sup>71,117</sup> Briefly, a room-temperature solution containing 4 mL of 1 M TOP-Se, 3 mL OLAM, and 1 mL ODE was rapidly injected into a 300 °C solution containing 0.750 mL of 0.5 M Cd(II)oleate, 1.2 g TOPO, and 9 mL of ODE. The temperature recovered and was maintained at 270 °C, and after 5 min, a solution containing 3 mL of 0.2 M Cd(II)oleate in ODE and 6 mL of 1 M TOP-Se was added dropwise over ~1h. The resulting nanocrystals exhibited a lowest energy absorbance peak at 605 nm, corresponding to an approximate size of 4.8 nm.<sup>118</sup>

*CdSe/CdS “giant” quantum dot (gQD) synthesis:* CdSe/CdS gQDs were synthesized using a SILAR approach, following previously published methods.<sup>71</sup> Briefly,  $2.0 \times 10^{-7}$  mol

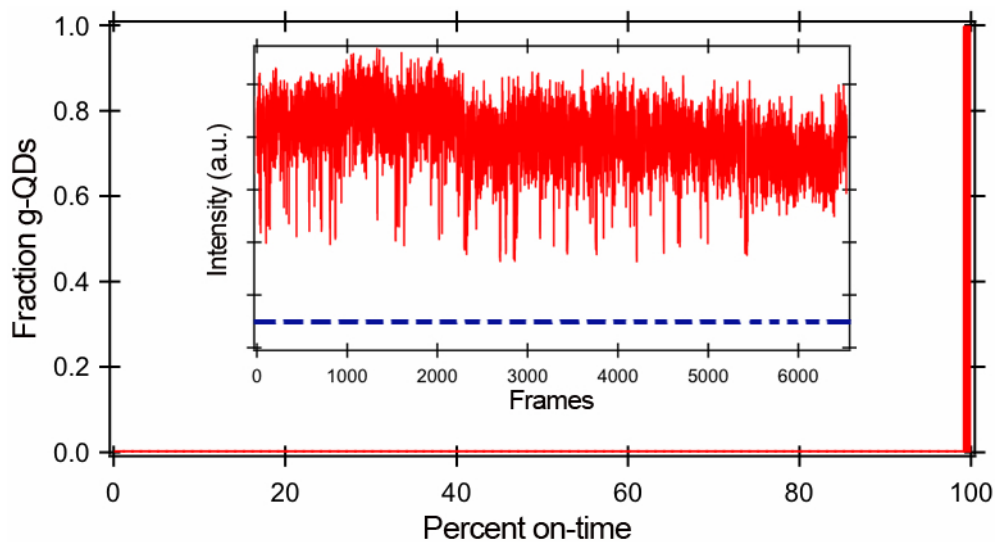


Figure 4.13: **Nonblinking fraction of g-QD sample.** The fraction of g-QDs that were observed to be nonblinking was 100%, as illustrated here. The inset shows a sample nonblinking trace of a single g-QD for a  $\sim 35$  minute collection period.

of purified CdSe cores, dispersed in hexanes, were added to a mixture of 5 mL OLAM and 5 mL OD. Hexanes were removed in vacuo at 80 °C, and the temperature was raised to 240 °C for SILAR. Alternating injections of 0.2 M Cd(II)oleate and 0.2 M sulfur (both in OD) were performed in a dropwise fashion, allowing 3 h of solution-phase annealing after each Cd(II)oleate addition and 1 h after each S addition. The delivered precursor volumes were calculated<sup>71</sup> to yield one ML of CdS shell per addition cycle, for a total of 16 ML CdS.

#### 4.12.2 Nonblinking fraction of g-QDs

The nonblinking fraction of the analyzed g-QD sample was determined to be 100% in a separate study, as shown in Figure 4.13.

#### 4.12.3 Derivation of the two-state charging model

The model for fitting QY vs average lifetime was derived by assuming that the maximum measured lifetime for each QD was the lifetime of the neutral exciton. The range of  $\tau_X$  is then taken to be between the highest and lowest measured values of  $\tau_X$ . The QY is

taken to be:

$$sQY = \frac{AQ_{max} + BQ_{min}}{A + B}$$

where  $A + B = 1$ , and  $Q_{max}$  and  $Q_{min}$  are the QY of the neutral and charged state, respectively. Rearranging this equation gives

$$B = \frac{A(Q_{max} - Q_{avg})}{Q_{avg} - Q_{min}}$$

Similarly, the average lifetime can be expressed as:

$$\tau_{avg} = \frac{A\tau_X + B\tau_{X^-}}{A + B}$$

where  $\tau_X$  can be taken to be the maximum measured lifetime of a single QD. Meanwhile, the lifetime of the charged state can be expressed as a sum of the radiative and Auger lifetimes:

$$\frac{1}{\tau_{X^-}} = \frac{1}{\tau_{min}} = \frac{1}{\tau_{r,X^-}} + \frac{1}{\tau_{A,X^-}}$$

and “statistical” scaling indicates that

$$\frac{1}{\tau_{r,X^-}} = \frac{2}{\tau_{r,X}}$$

Further, the QY of the charged state can be expressed as

$$Q_{X^-} = Q_{min} = \frac{\frac{1}{\tau_{r,X^-}}}{\frac{1}{\tau_{r,X^-}} + \frac{1}{\tau_{A,X^-}}} = \frac{\frac{2}{\tau_{r,X}}}{\frac{1}{\tau_{r,X}}}$$

and

$$\tau_{min} = \frac{Q_{min}}{2} \tau_{max}$$

so the average lifetime becomes

$$\tau_{avg} = \frac{A\tau_{max} + B\tau_{min}}{A + B} = \frac{A\tau_{max} + B(\frac{Q_{min}}{2})\tau_{max}}{A + B}$$

which rearranges to

$$A\tau_{avg} + B\tau_{avg} = A\tau_{max} + \frac{BQ_{min}\tau_{max}}{2}$$

Substituting the equation for the scaling parameter  $B$  and rearranging gives the final form:

$$Q_{avg} = \frac{\tau_{avg}(Q_{max} - Q_{min}) + \tau_{max}(\frac{Q_{min}}{2})(2 - Q_{max})}{\tau_{max}(1 - \frac{Q_{min}}{2})}$$

When the known values for  $Q_{max}$  (1),  $Q_{min}$  (0.03), and  $\tau_{max}$  (upper bound: 66 ns, lower bound: 189 ns) are substituted, we obtain the two linear equations representing the upper and lower bounds of our model, which takes into account differences in neutral exciton lifetime:

$$Q_{avg}(upper) = 0.0149\tau_{avg} + 0.0137$$

$$Q_{avg}(lower) = 0.0052\tau_{avg} + 0.0137$$

All but three of the QDs fall within this range.

Average lifetimes for QDs were calculated as a weighted average of lifetimes from the FLID probability distribution plot. For many of the examined QDs, a triple-exponential decay would have been necessary to fully describe the decay dynamics. This indicates that there may be a multiexciton or multiply charged state involved in QD emission. This state was typically faintly visible as an additional correlated lifetime-intensity state in the FLID, however, and is therefore not likely to be the reason for different QDs being pinned to differing QYs.

#### 4.12.4 Comparison of a spherical QD approximation with volume from HAADF intensity

It was interesting to find that approximating the g-QDs as a sphere did not result in a drastic change in the measured QD volume. Typically, the calculation of sphere volume from the feret diameter resulted in a slightly larger volume estimate than the calculation of volume from HAADF intensity. The average difference between these two calculations, however, was only 19%. Therefore, even an approximation of the g-nQDs as spheres results in the observation of a heterogeneous distribution of QYs. The full statistical data comparing the two methods of calculating QD volume are shown in Table 4.1.

#### 4.12.5 Physical and optical data of studied g-QDs

Table 4.2 shows select physical and optical data for all g-QDs studied.

#### 4.12.6 Sample preparation

A transmission electron microscopy (TEM) support film coated with polystyrene latex sphere markers was prepared for correlation as reported previously.<sup>102</sup> The synthesized g-QD samples were diluted to  $\sim 1$  nM concentration in hexanes. Approximately 10  $\mu$ L of this solution was then dropcast onto the prepared support film (Ted Pella, PELCO 8 nm Ultra-Flat Silicon Dioxide Support Film) and the residual hexanes solution was immediately wicked away with a KimWipe.

#### 4.12.7 Fitting of $g^{(2)}$ traces for determination of center peak to side peak ratio

Many of the acquired  $g^{(2)}$  traces had sharp peaks attributed to cross-talk between APDs. To determine true areas of peaks on the  $g^{(2)}$  plots, we implemented a global fit that allowed fitting of multiple parameters on each peak simultaneously. Typically, peaks were fit with a double exponential decay or rise of the form:

Table 4.1: Comparison of calculation of sphere volume with calculation of volume from HAADF integrated intensity.

	$V_{\text{SPHERE}}$ (nm <sup>3</sup> )	$V_{\text{HAADF}}$ (nm <sup>3</sup> )	% Difference (norm.)
	38743	39535	2.0
	43840	42637	2.7
	58881	54037	8.2
	50369	48624	3.5
	52448	45122	14.0
	39551	39485	0.2
	50139	53000	5.7
	41711	46056	10.4
	68003	112704	65.7
	55318	51719	6.5
	45170	47729	5.7
	45725	42449	7.2
	60782	51789	14.8
	41508	38755	6.6
	45663	39589	13.3
	28051	31749	13.2
	24101	32457	34.7
	82082	66250	19.3
	43997	42294	3.9
	36532	74023	103
	38770	38257	1.3
	40759	82070	101
	45293	39622	12.5
	38422	34446	10.3
<b>Average:</b>	<b>46494</b>	<b>49767</b>	<b>19</b>

Table 4.2: **Physical and optical data of studied g-QDs.** QY is the single g-QD quantum yield, normalized to the highest QY. BXQY is biexciton quantum yield measured from  $g^{(2)}$  and single g-QD QY.  $\tau_{\text{avg}}$  is the average lifetime in nanoseconds.  $D_F$  is the Feret diameter in nanometers.  $\sigma$  is the absorption cross-section in  $10^{-13} \text{ cm}^2$ .

	<b>QY</b>	<b>BXQY</b>	$\tau_{\text{avg}}$ (ns)	$D_F$ (nm)	$\sigma(10^{-13} \text{ cm}^2)$
	1	0.29	45	17.9	2.62
	0.99	0.21	74	21.1	3.19
	0.92	0.28	49	22.1	3.20
	0.55	0.18	37	21.5	3.72
	0.47	0.18	38	23.2	3.64
	0.45	0.13	39	21.9	3.44
	0.42	0.19	18	21.5	3.12
	0.41	0.14	54	24.1	3.09
	0.41	0.19	34	22.9	4.36
	0.40	0.19	30	22.9	3.92
	0.39	0.18	32	22.2	3.19
	0.39	0.15	42	18.8	2.56
	0.38	0.14	24	21.0	3.19
	0.36	0.10	30	21.0	2.78
	0.36	0.18	30	21.9	3.41
	0.34	0.15	25	22.1	3.85
	0.32	0.12	41	21.3	6.62
	0.27	0.13	27	24.4	4.18
	0.27	0.16	33	27.0	5.35
	0.27	0.11	30	22.9	4.28
	0.26	0.10	25	22.2	3.43
	0.26	0.09	36	20.6	5.97
	0.24	0.08	33	25.3	9.10
	0.23	0.11	23	23.6	4.17
<b>Average:</b>	<b>0.43</b>	<b>0.16</b>	<b>35</b>	<b>22.1</b>	<b>4.0</b>

$$f(x)_{rise} = y_0 + A_1 e^{\frac{x-x_0}{\tau_1}} + A_2 e^{\frac{x-x_0}{\tau_2}}$$

$$f(x)_{decay} = y_0 + A_1 e^{-\frac{x-x_0}{\tau_1}} + A_2 e^{-\frac{x-x_0}{\tau_2}}$$

For the global fit analysis,  $\tau_1$ ,  $\tau_2$ ,  $A_1$ ,  $A_2$ , and  $x_0$  were linked for the center peak rise and decay. Further,  $\tau_1$  and  $\tau_2$  were linked for the left and right peak rise and decay.  $A_1$  and  $A_2$  were linked for the left peak, and  $A_1$  and  $A_2$  were linked for the right peak.

Finally,  $y_0$  was linked for all fit rises and decays. The variable  $x_0$  was set to the known value based upon the laser repetition rate. After fitting, the area under the fit curves was integrated to yield the center-to-side peak ratio, which has been referred to simply as  $g^{(2)}$  in this manuscript for convenience.

## Chapter 5

### Conclusions

In this work, the necessity of fully studying and understanding single QDs at a time was demonstrated through a series of experiments on colloidal QDs. The developed correlation strategy was incredibly useful for examination of two well-known, well-studied CdSe/CdS core/shell heterostructure QD systems. It is expected to be even more powerful when applied to relatively undeveloped QD and nanostructure syntheses.

*The presented strategy of correlating fine atomic structure with quantum optical single-photon data can be used as an ideal tool to enhance the means by which QD synthesis is performed.*

#### 5.1 Overall conclusions

The greatest obstacle in performing a study to understand the interplay of structure and function on a single QD level is not in the data analysis, but in the use of an unambiguous, reproducible method to acquire these correlated data. Because it is not yet possible to simultaneously acquire electron micrographs and fluorescence data from the same single QD, a method had to be developed which allowed precise identification of QDs and examination of these QDs in both optical and electron microscopes. The specific strategy of using polystyrene latex beads as fiducial markers and an ultrathin support substrate of SiO<sub>2</sub>—demonstrated in Chapter 2—has been developed and implemented here to great effect. This strategy is characterized by traits of simplicity, reproducibility, lack of ambiguity, and universality that make it a powerful technique for studying fine physical effects on the optical behavior of colloidal nanostructured systems. Within the context of this dissertation, the correlation strategy has provided answers to questions about CdSe/CdS

heterostructured QD systems that would perhaps otherwise have remained unanswered.

By studying a CdSe/CdS core/shell QD heterostructure with incomplete surface overcoating but high ensemble PLQY, a detailed view of the effects of structural heterogeneity on optical properties was provided in Chapter 3. There exists a bulk of literature research into the nature of the QD surface and its effect on QD photoluminescence, but the work presented here is the first to directly pinpoint specific surface defects and directly correlate them with detrimental PL behavior in QDs. Additionally, crystal structure, orientation and shell epitaxy were demonstrated to be highly important considerations that must be optimized fully to achieve optimal QD heterostructure synthesis. The powerful correlation technique demonstrated here will assist with this optimization.

Chapter 4 demonstrated the most complete description of a single colloidal QD that has been achieved: high-resolution scanning electron microscopy showed the exact shape and fine atomic structure of the QD, energy dispersive x-ray spectroscopy demonstrated the variation of chemical composition within the QD, and advanced single-photon detection and analysis techniques allowed determination of the fluorescent lifetime,  $g^{(2)}$  spectrum, and time-dependent photoluminescence behavior of the QD. Additionally, because quantitative techniques were used to measure the PL and the atomic structure, the quantum yield of single QDs was determined. Surprisingly, the examined sample exhibited a variety of quantum yields correlated to single QDs; this behavior was unexpected based upon past precedent. This study also directly demonstrated the utility of the presented correlation technique to inform the synthetic chemist: understanding that the ensemble PLQY is characterized by charging, rather than the presence of a large fraction of “dark” QDs, allows for guidance of efforts to improve the synthesis of this QD system.

### 5.1.1 Limitations of the correlation

One of the major limitations of the technique presented in this dissertation is the inability to examine single QDs from multiple orientations. When making measurements of

photoluminescence and atomic structure, the orientation of the QD influences radiative decay intensity. Additionally, in order to obtain lattice-resolved or atomic resolution electron micrographs, the QD must be oriented such that it can be viewed along a lattice plane. If this condition is not met, it becomes difficult to understand the precise crystal structure of the individual QD—this could prevent study and discovery of important effects of atomic structure on single QD PL. For example, in Chapter 4, STEM-EDS was a crucial component of the study that allowed acquisition of core-centering data for CdSe/CdS core/shell heterostructures. However, the data still only provide a two-dimensional projection of the chemical composition; it is a distinct possibility (or even likelihood) that many of the three-dimensional centering values differed from those measured in two-dimensions.

Additionally, acquisition of extensive data for individual QDs is much more time-intensive than ensemble characterization of a QD sample. As presented here, the correlation technique would be much better suited to continue studying fundamental physical phenomena arising in QD systems, rather than as a tool for routine characterization of synthesized samples. Finally, the methods presented here are typically destructive with regard to the examined samples. Importantly, STEM is known to quench single QD PL.<sup>80,81</sup> For this reason, it is necessary to examine atomic structure only *after* acquisition of detailed PL data. If any photobleaching or structural changes occur due to the irradiation of the QD, the subsequently acquired electron micrograph(s) may be different than those that would have been acquired before PL study. This is unlikely to affect the overall structure of large core/shell heterostructures such as those studied in this dissertation, although it should be taken into account when studying more photon flux-sensitive materials.

## 5.2 Future work

### 5.2.1 QD development

It would be highly beneficial to use advanced single QD characterization techniques to study binary blinking QDs to elucidate the effects of charging in these emitters. Even more interesting would be a study of QDs from recently reported syntheses that exhibit both high ensemble PLQY and nonblinking behavior.<sup>115</sup> A very recent study purports to show bulky CdSe/CdS QDs with unity biexciton QY—our technique would be able to verify this assertion, and may be able to shine light on the mechanism by which BXQY is raised to such unprecedented levels on a global scale in this synthesis.<sup>119</sup>

### 5.2.2 Non-QD development

Perhaps some of the most intriguing applications of this work will be unrelated to the realm of quantum dot development. The general strategy laid out in this dissertation for correlation of optical and structural properties could be applied to a variety of colloidal nanostructures that demand a fully-informed refinement of synthetic parameters to yield optimal syntheses. Single nanoparticle fine absorption measurements continue to increase in resolution—correlation of this property with structures of nanostructures could illuminate the convolution of size, shape, aspect ratio and volume that are known to dictate single particle absorption and reflectance.<sup>120</sup> Additionally, plasmonic behavior could be studied as a function of physical parameters for a wide variety of colloidal nanosystems.

### 5.2.3 Ramifications of this work for colloidal quantum dot research

The correlation technique presented here has been utilized to understand the fundamental physics of single CdSe/CdS QDs. However, the potential for this technique is much more far-reaching. In fact, the heightened understanding of QD photophysics derived from the characterization and analysis herein can inform future synthetic strategies. The results

presented in Chapter 3 demonstrate that chemistry and stoichiometry of facets are crucial in deciding shell morphology and epitaxy, and therefore are able to dictate the PL behavior of the QD batch. Chapter 4 showed that, even within QDs with a “giant” inorganic shell, surface trapping processes can still dictate the emission, and tie into important processes such as single QD and ensemble QY.

The synthesis of CdSe-based QD systems, however, has benefited from decades of synthetic refinement by dozens of state-of-the-art academic and industrial research labs. The characterization technique presented in this dissertation may be more ideally suited to development of less well-studied QD syntheses that must compete with Cd-based strategies for enhancement of light emitting devices and photovoltaics. Many such II-VI and III-V structures have been demonstrated to exhibit great promise for replacement or complementing of CdSe as a “workhorse” colloidal QD system.<sup>121</sup>

One would assume that the synthesis of these alternative compositions of QDs would be readily informed by the abundance of literature available for CdSe QDs. However, it is becoming apparent that even the basic traditional nucleation and growth mechanism for CdSe is not universally displayed by other QD heterostructures. Rather than proceed through the slow, iterative development process that has been followed for CdSe, it will be crucial to use advancing characterization methods to better understand the results of colloidal synthesis, thereby allowing the nanochemist to make a much more informed decision of how to proceed when developing new QD chemistry.

## Appendix A

### Structures and Photoluminescence of Commercially Available CdSe/CdS Core/Shell Quantum Dots

Following are structures of all examined LifeTech™ QD605 QDs. Each structure is labeled with the observed “on-fraction.” Additionally, QDs placed in subpopulations in Sections 3.3—3.5 are labeled according to the legend at the end of the displayed structures.

In Figure A.1, (A) shows the raw summed fluorescent image over 2000 s; 14 regions of interest (ROIs) can be seen on this wide-field fluorescent image, as shown in (B). (C) shows the bright field image from the optical microscope, which corresponds to the low- and medium-magnification TEM images shown in (D) and (E), respectively. (F) shows a Z-STEM image of the area near the bottom of the PS formation shown in (E). ROIs could be identified as bright spots highly localized to only a few pixels; further magnification resulted in the high-resolution images as in (G), (I), (K), (M), (O) and (R). (H), (L) and (N) show medium-magnification identification of ROIs. Frequently, after imaging a QD, contamination would occur that showed up as a brighter spot on subsequent lower-magnification scans. This is the case with ROI2 in (J). When the ROI is not close enough to the PS to allow direct correlation, grid contamination can be used as an aid for finding ROIs from the fluorescence image, as shown in (P) and (Q).

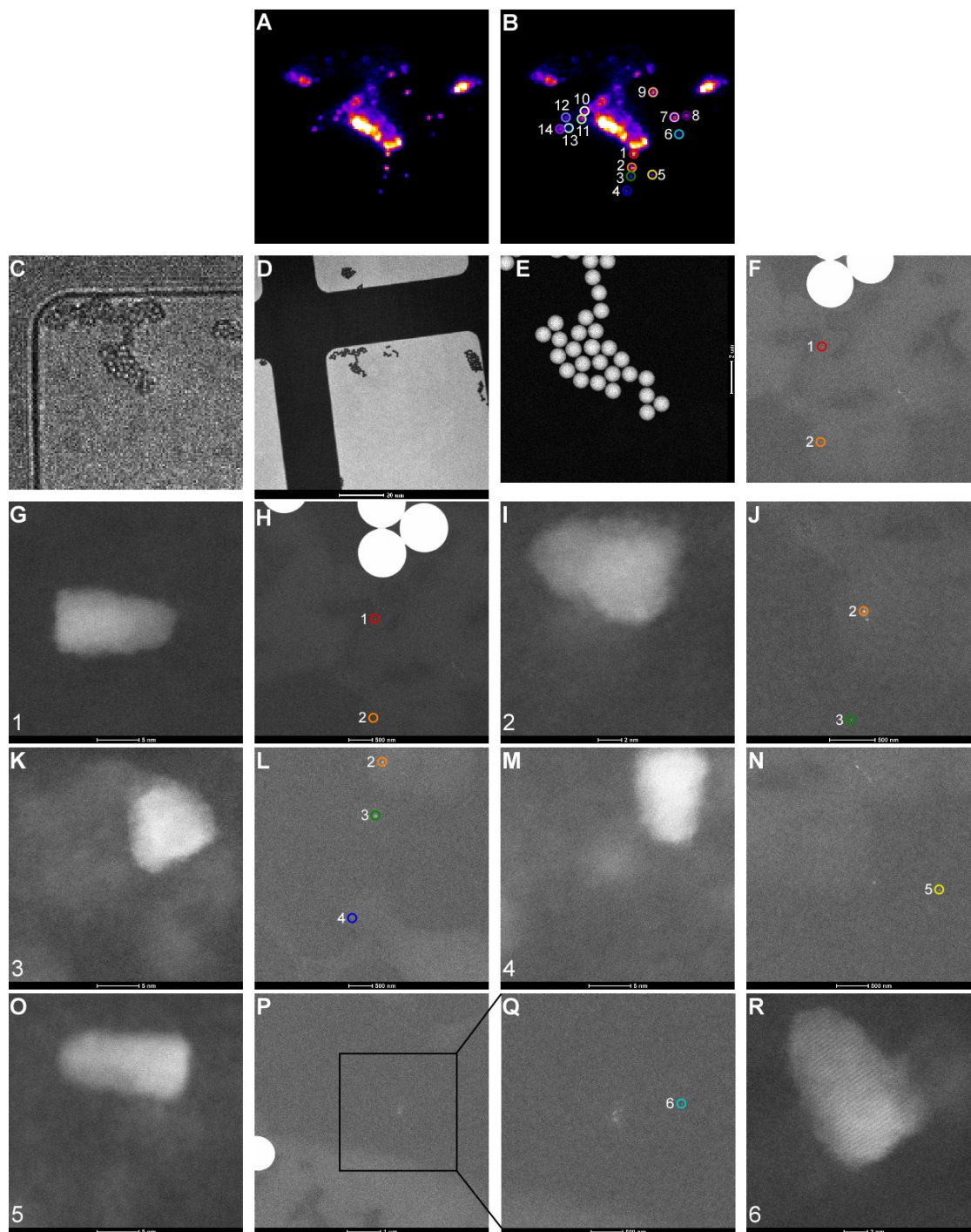


Figure A.1: An illustration of the method used to locate and interrogate single QDs on the 8 nm SiO<sub>2</sub> support film.

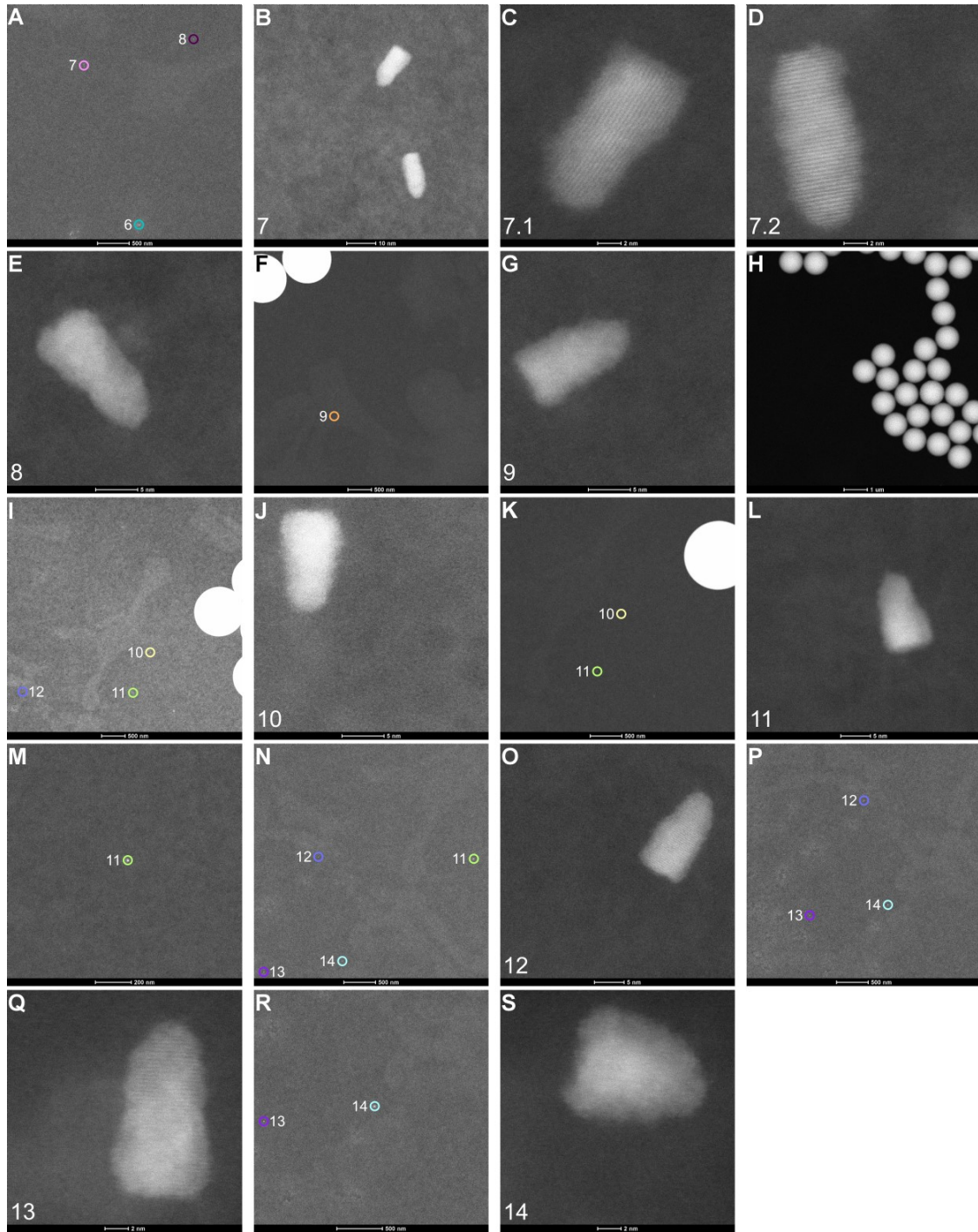
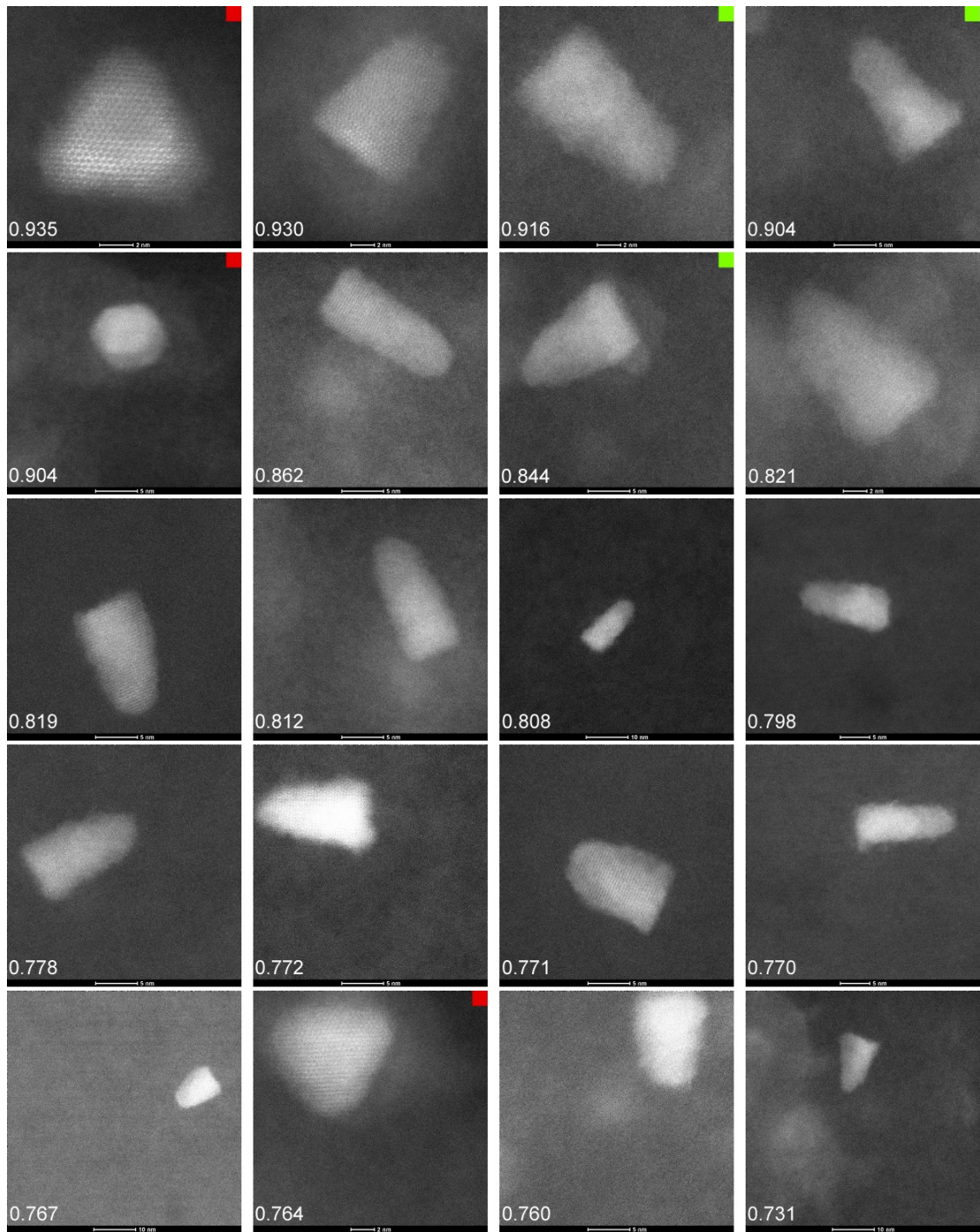
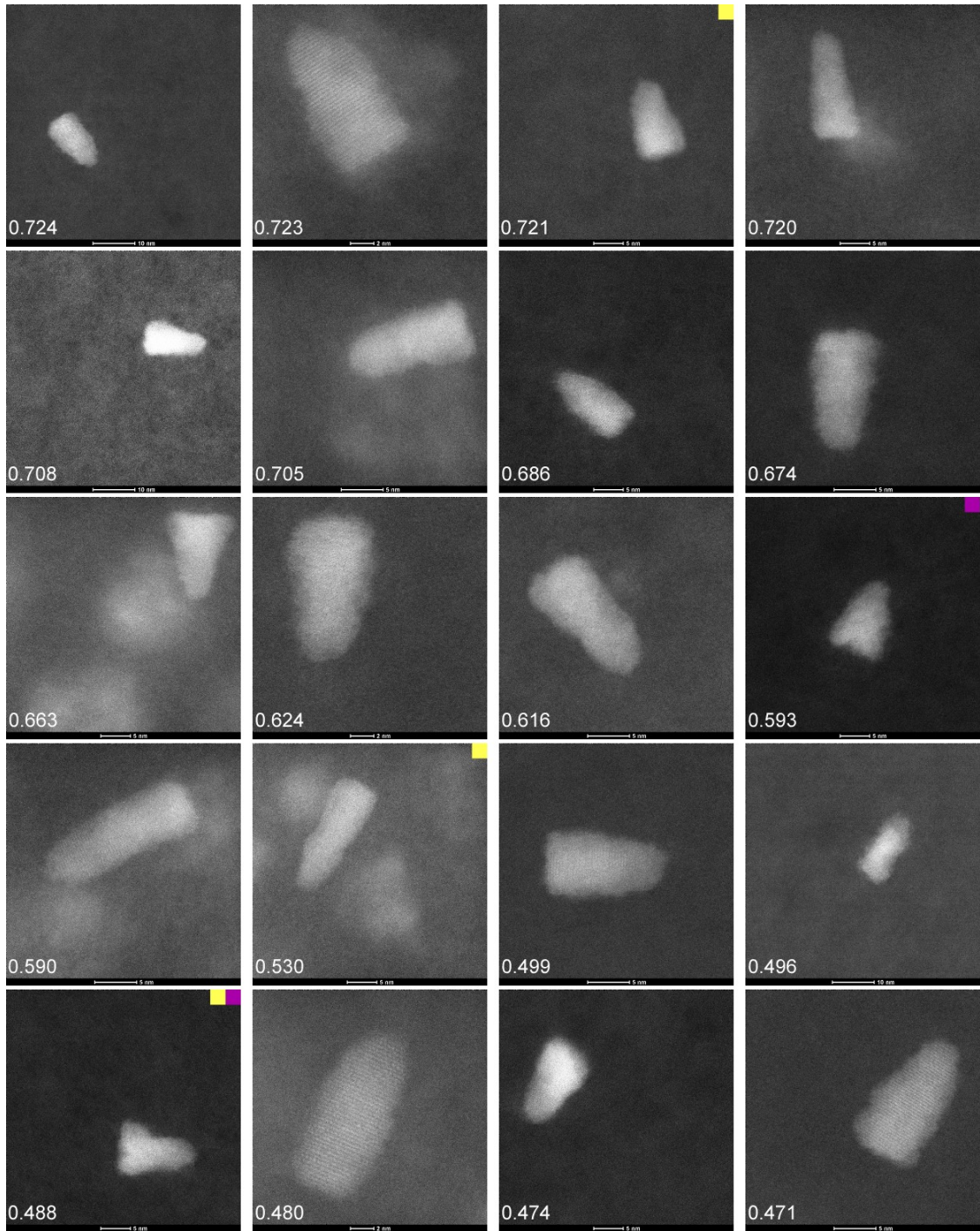
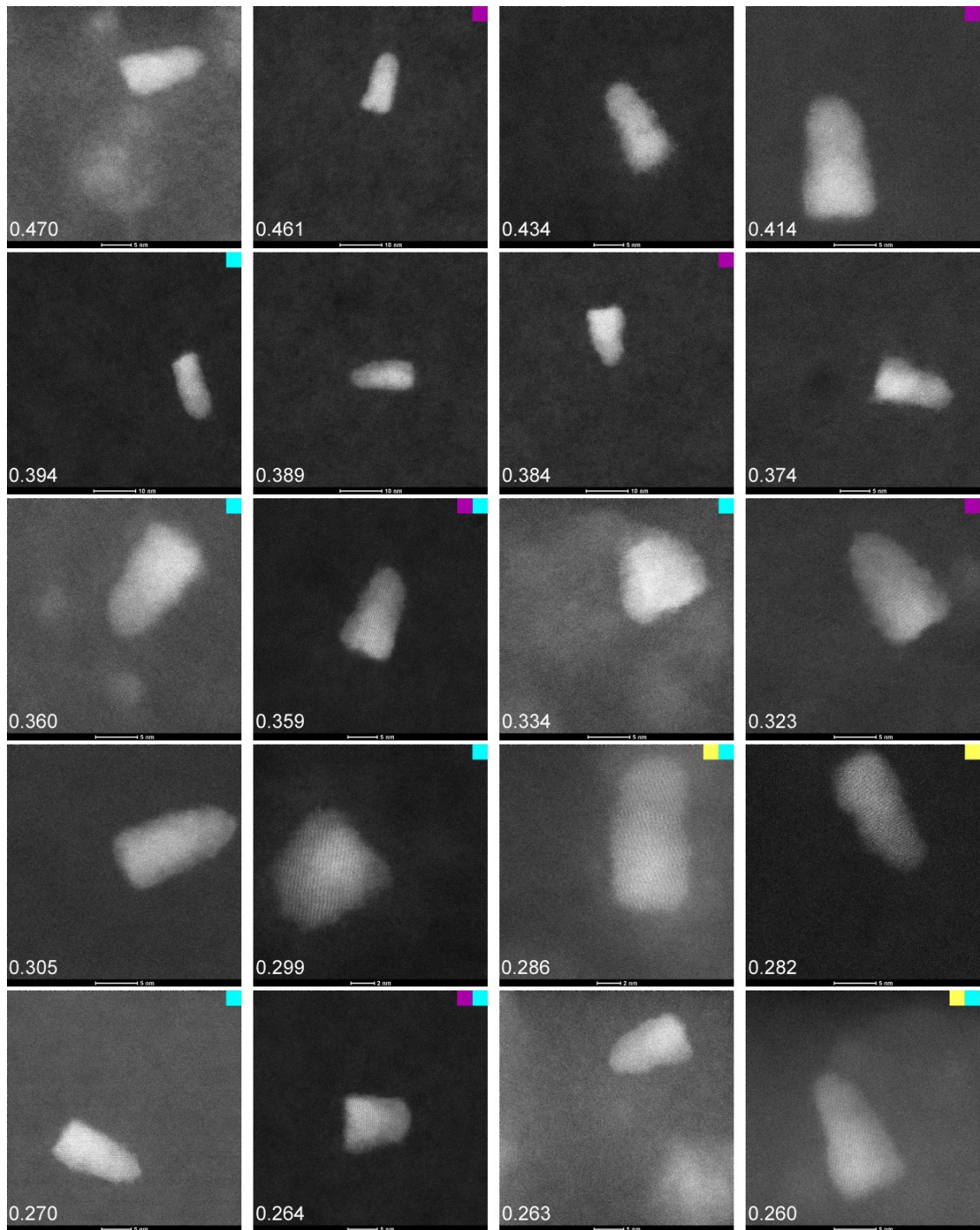
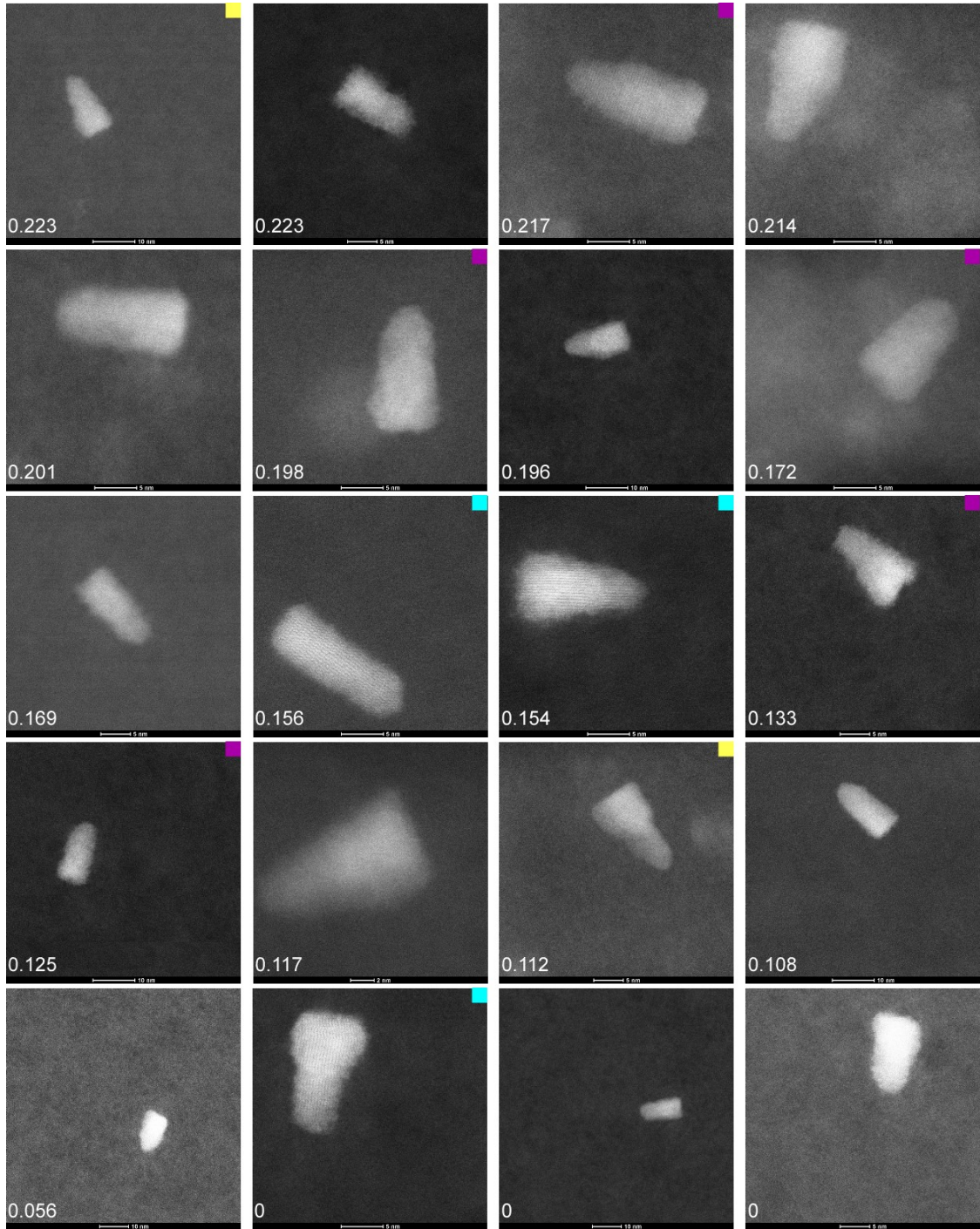


Figure A.2: **Acquisition of Z-STEM images for the remaining ROIs shown in (A).** (A), (F), (H), (I), (K), (M), (N), (P), and (R) show the medium-magnification identification of ROIs, while (B), (C), (D), (E), (G), (J), (L), (O), (Q), and (S) show high-resolution scans of individual ROIs. Occasionally, a fluorescent ROI would occur due to multiple QDs occupying the same region as shown in (B). These ROIs containing multiple QDs were readily identified; all instances of multiple QDs in the same region were disregarded for the purposes of this study.









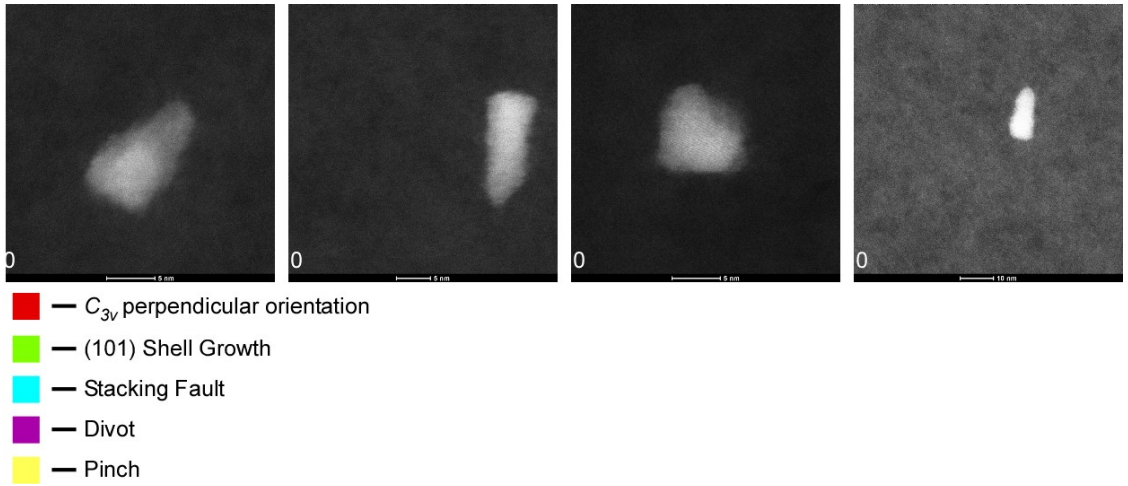
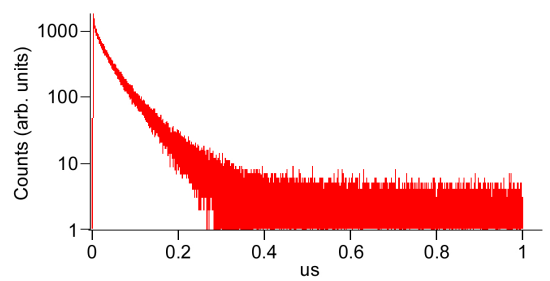
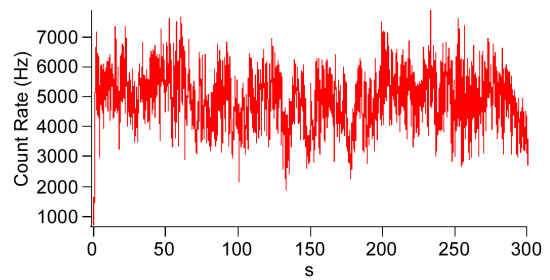
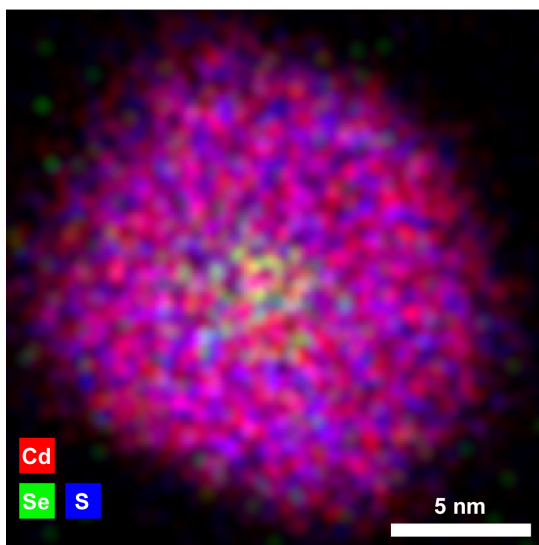
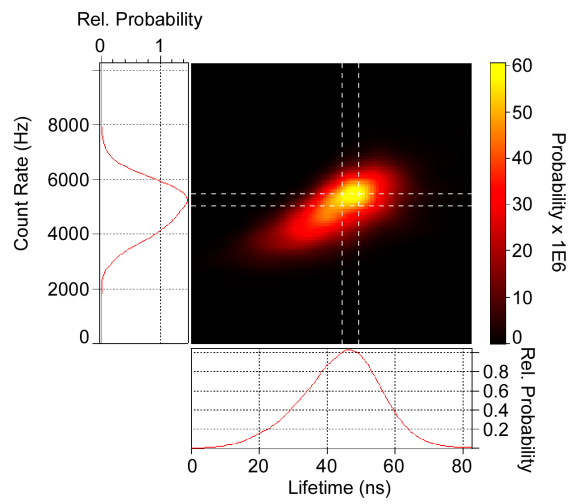
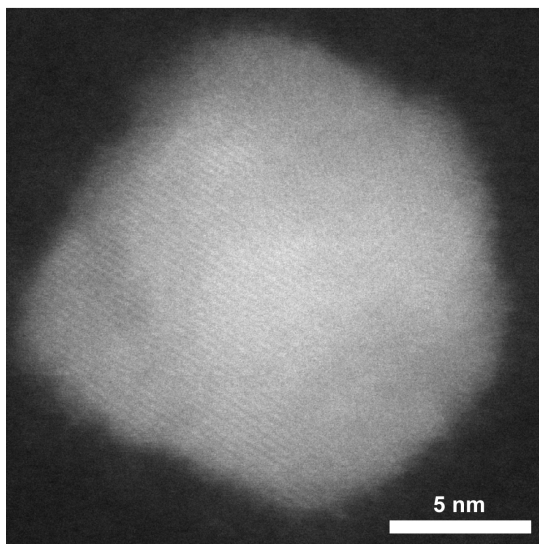


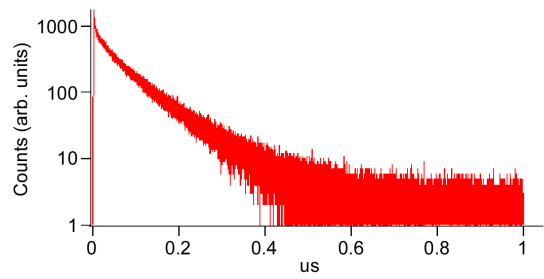
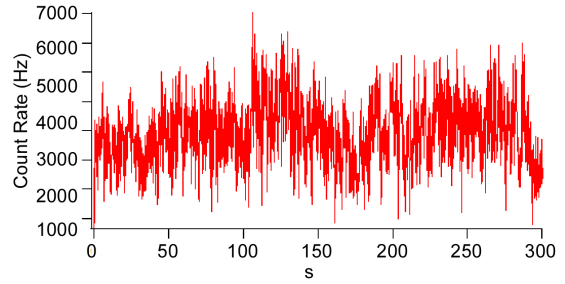
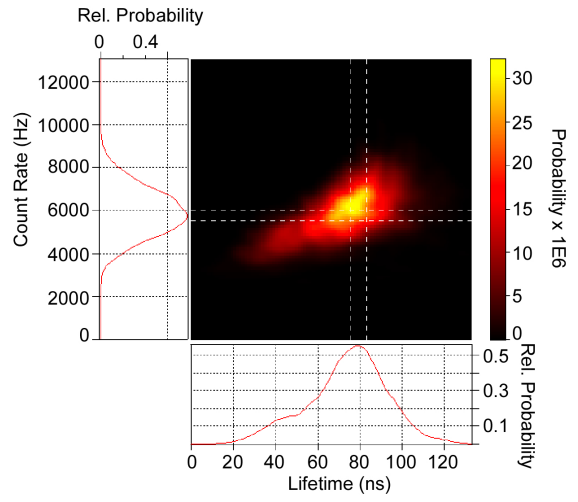
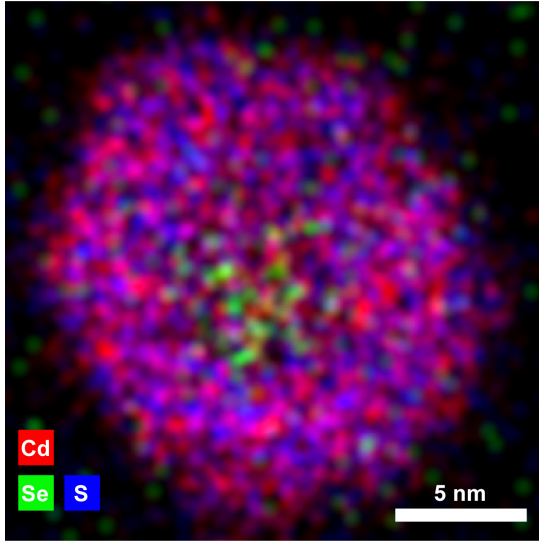
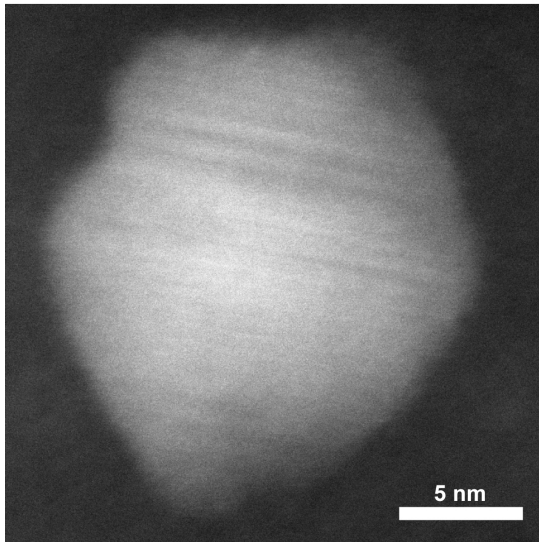
Figure A.3: **High-resolution Z-STEM images for all of the QDs used for this study.** Shown along with the image of each QD is the corresponding on-fraction. This image also highlights QDs placed into the subpopulations identified in the main text.

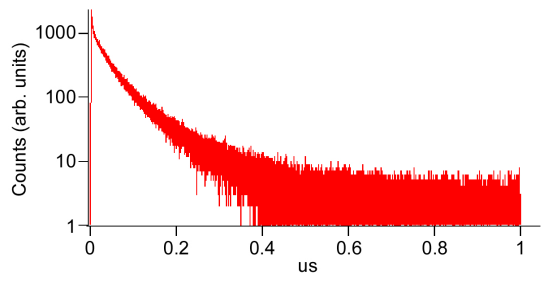
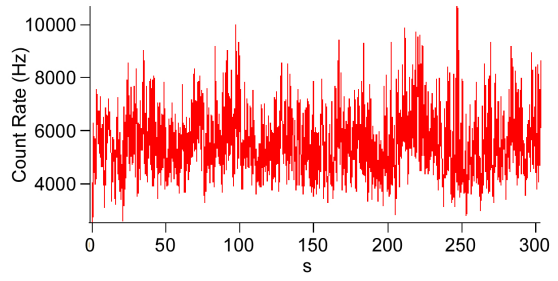
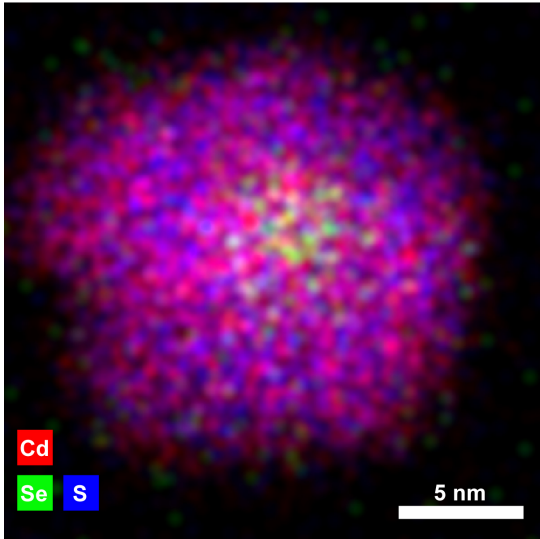
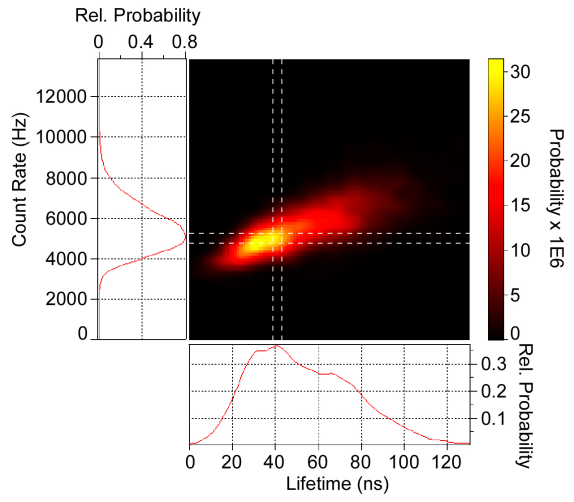
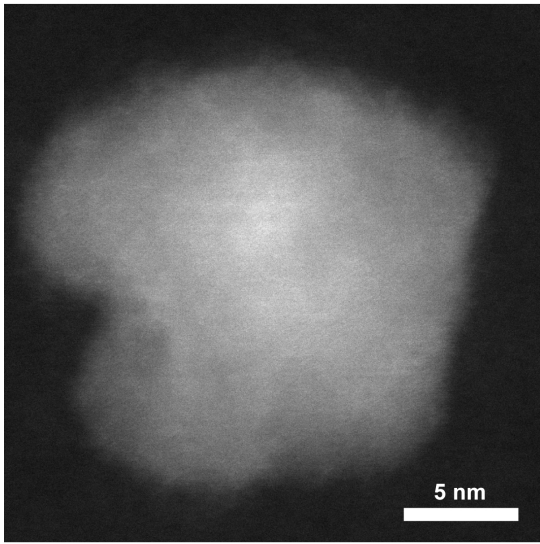
## Appendix B

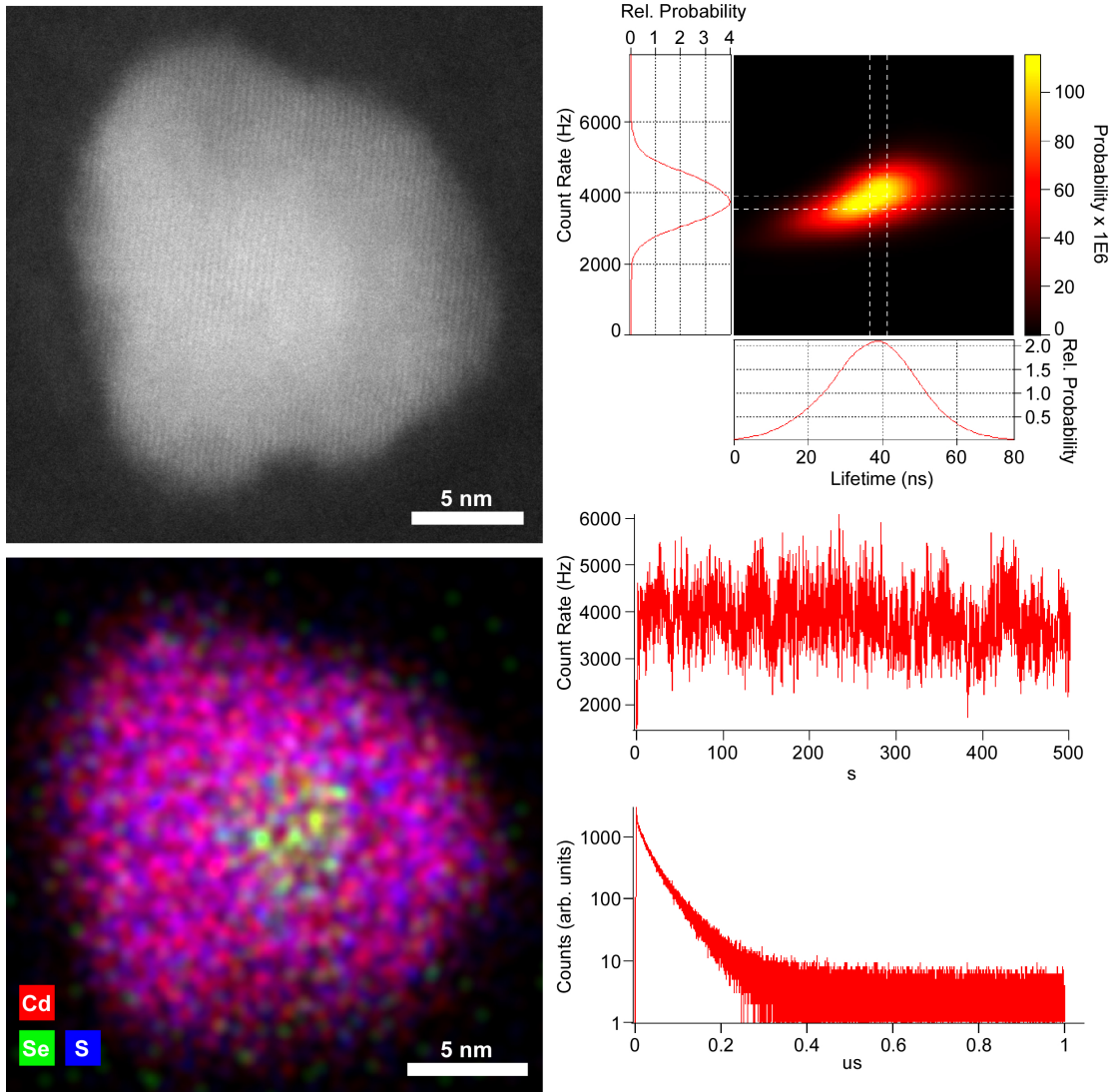
### Full Structural and Optical Data for Studied “Giant” CdSe/CdS Core/Shell Nanocrystal Quantum Dots

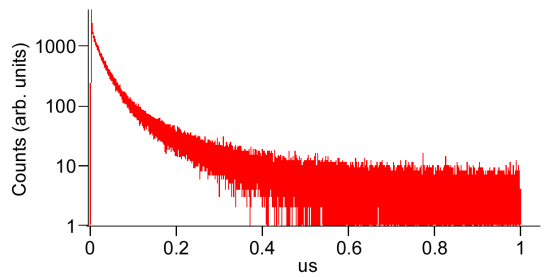
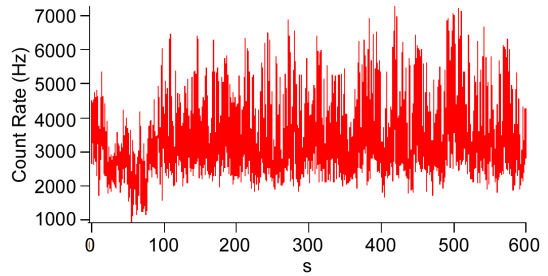
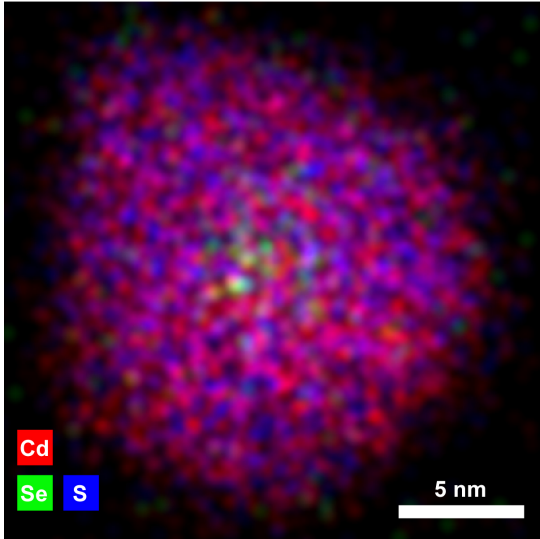
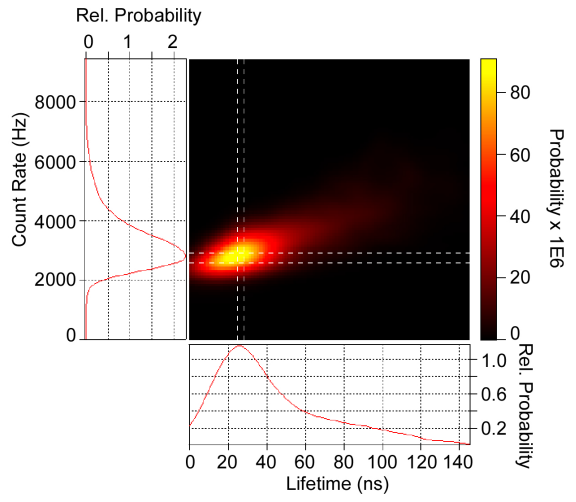
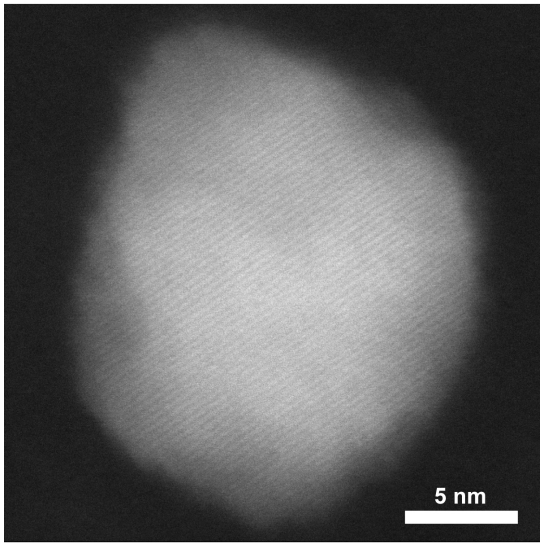
Following are all collected structural, chemical and optical data for the g-QDs studied in Chapter 4. The g-QDs are displayed in order of measured QD QY. Refer to Table 4.1 and Table 4.2 for optical and physical data corresponding to these g-QDs.

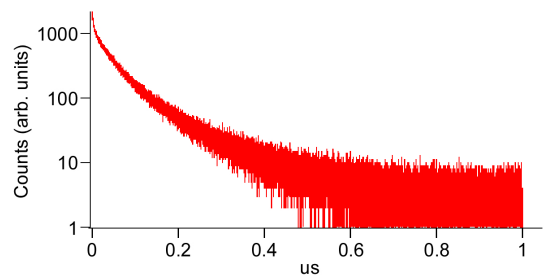
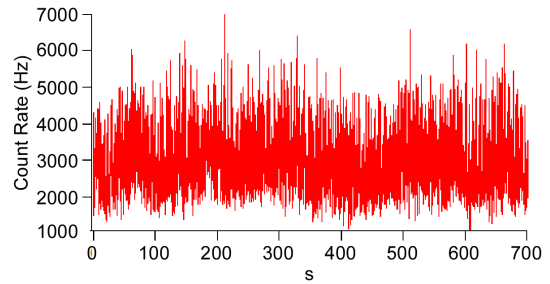
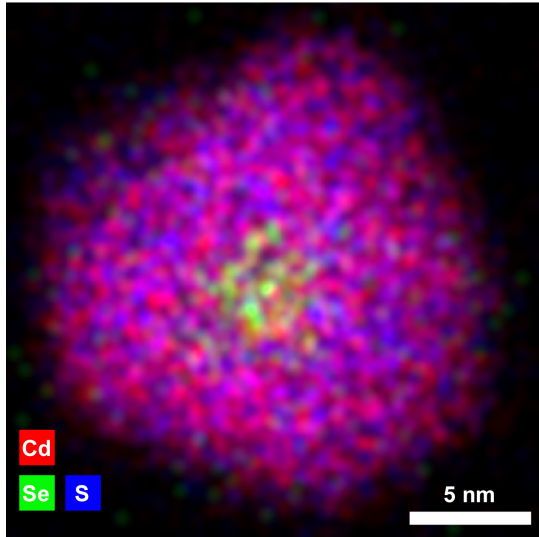
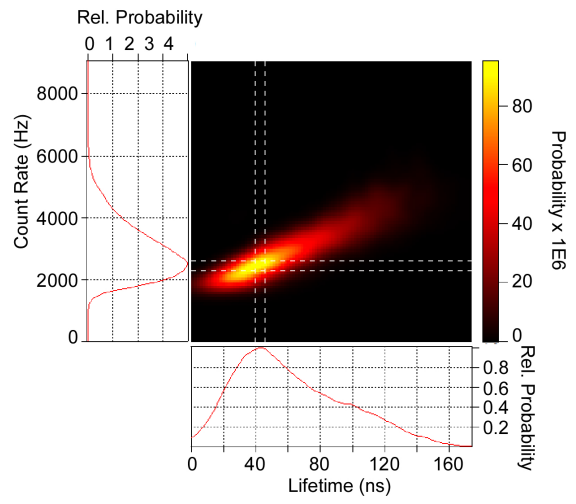
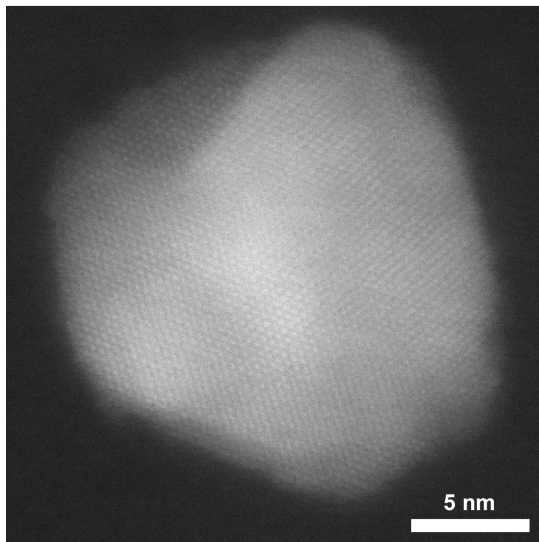


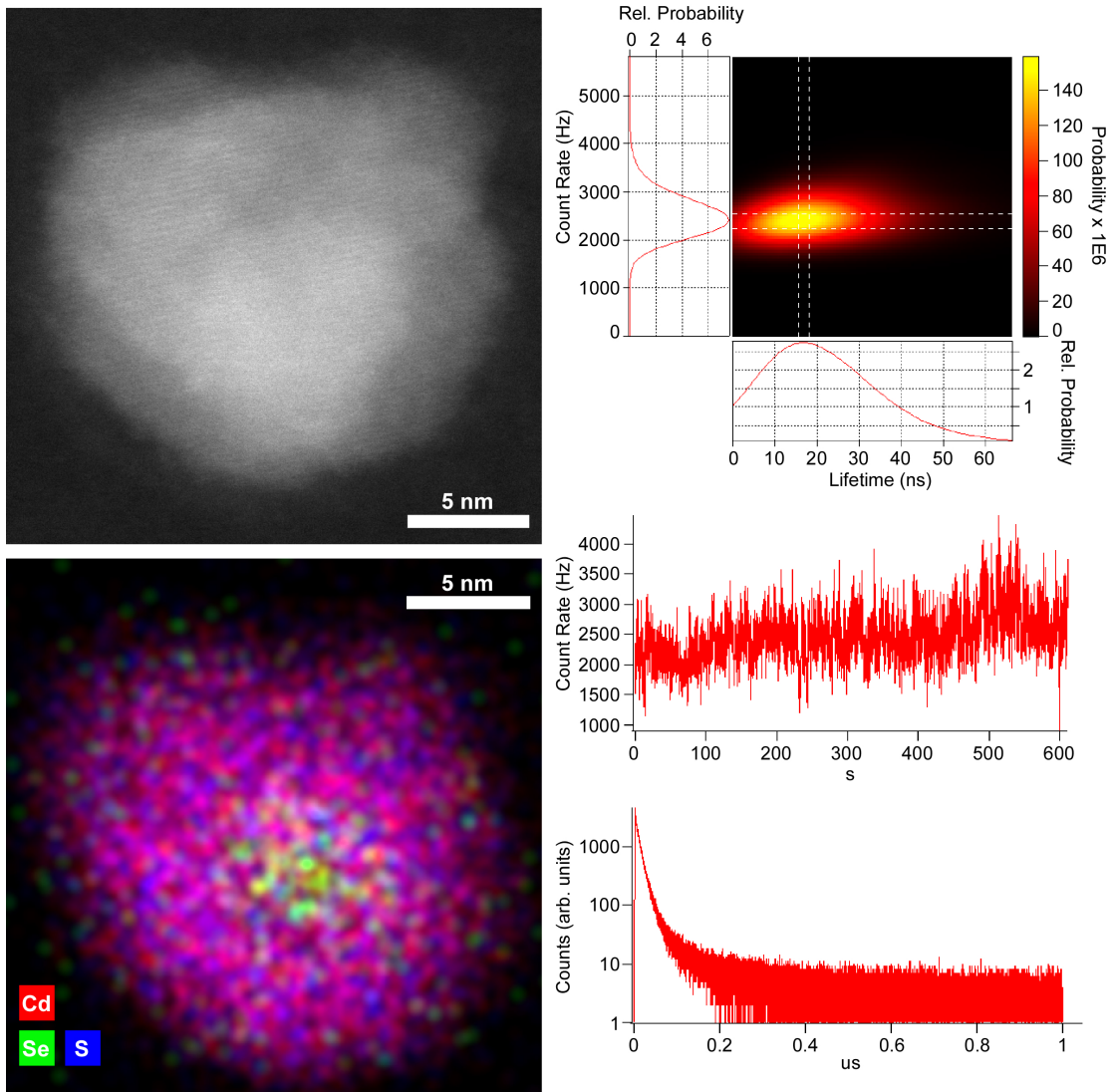


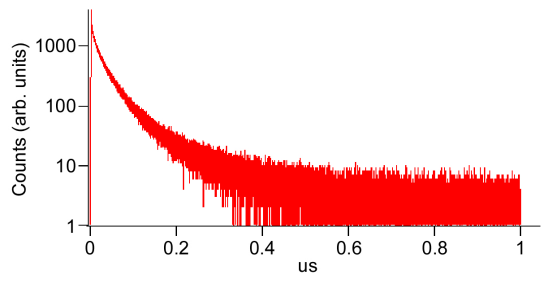
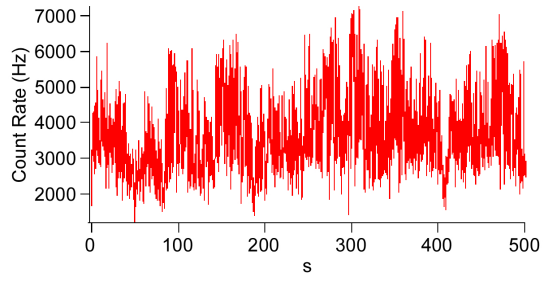
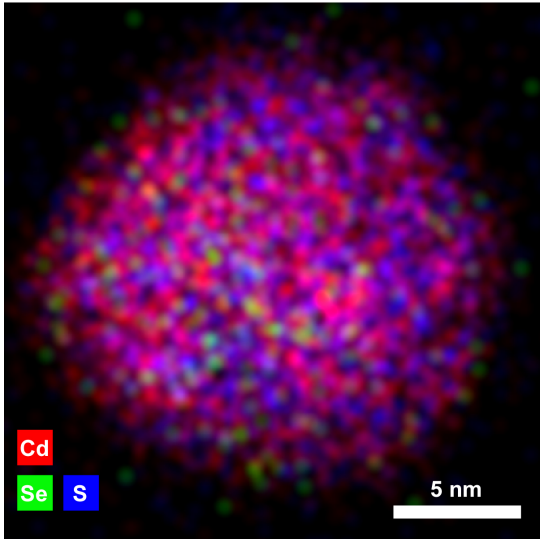
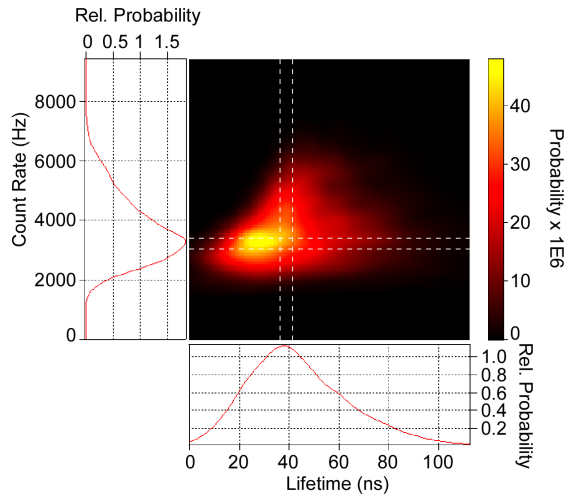
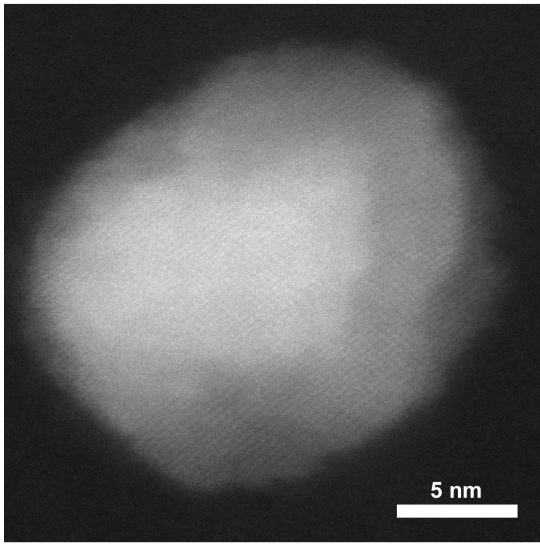


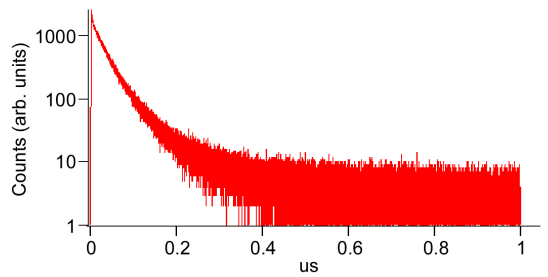
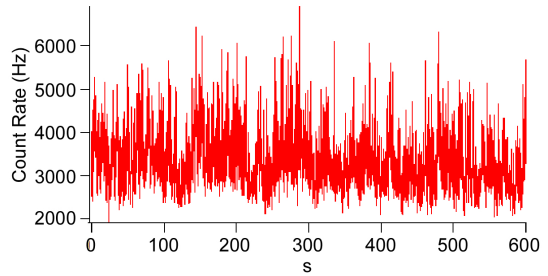
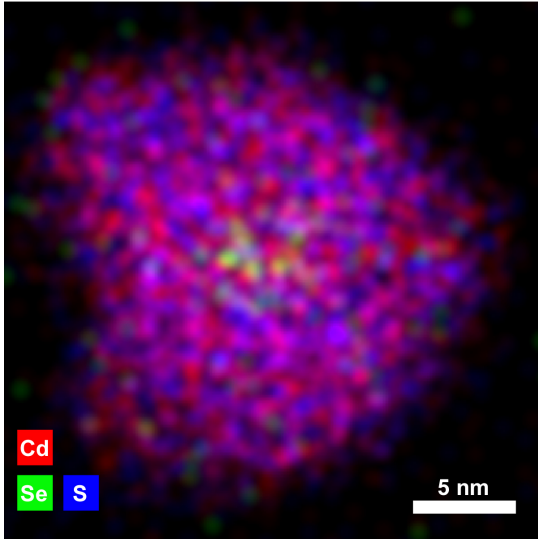
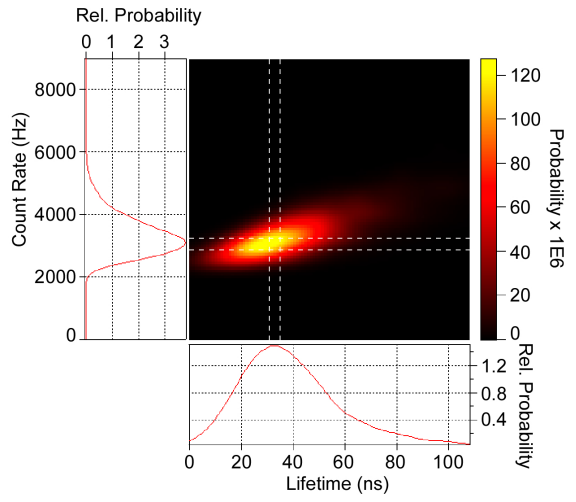
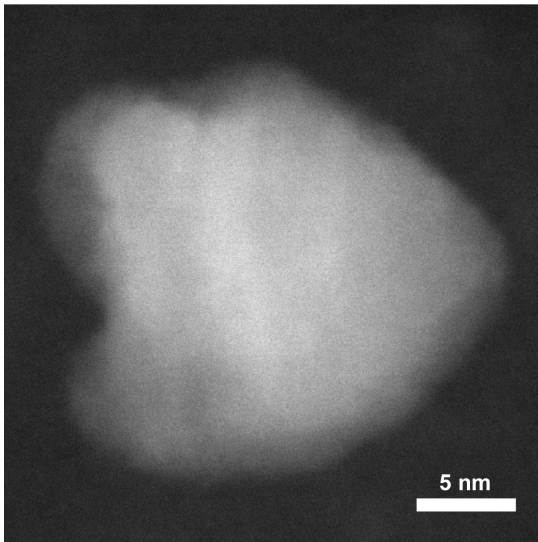


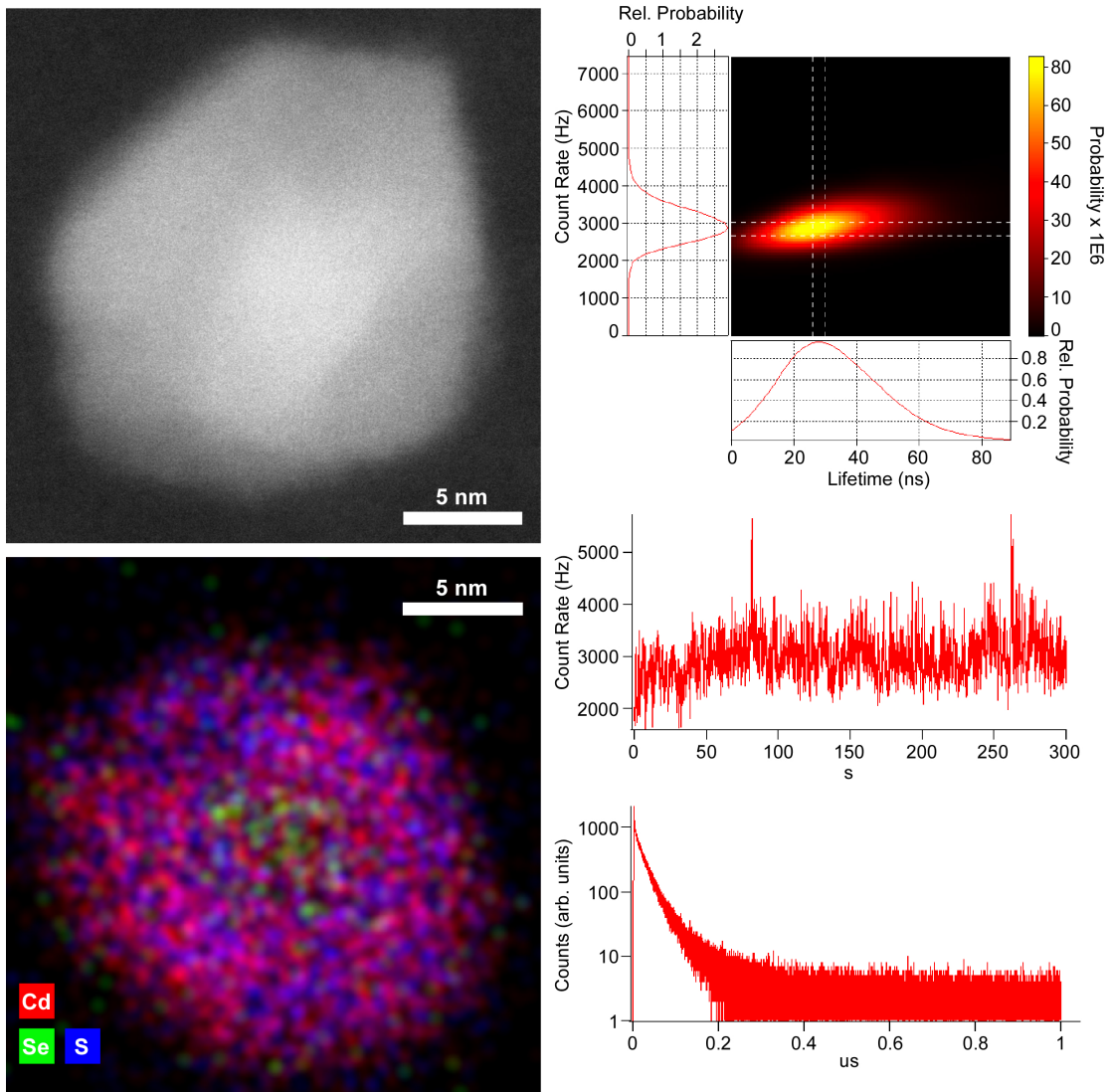


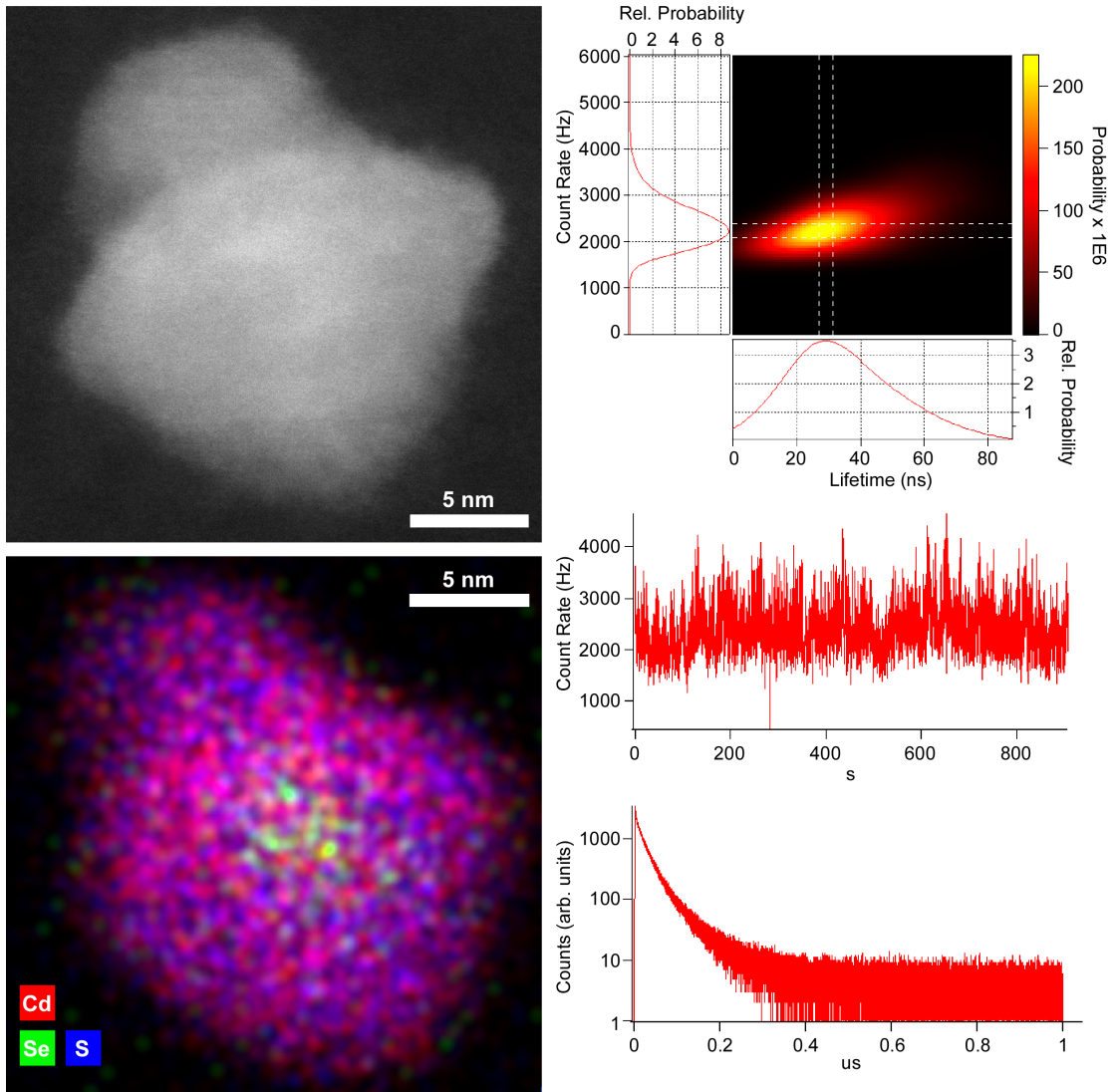


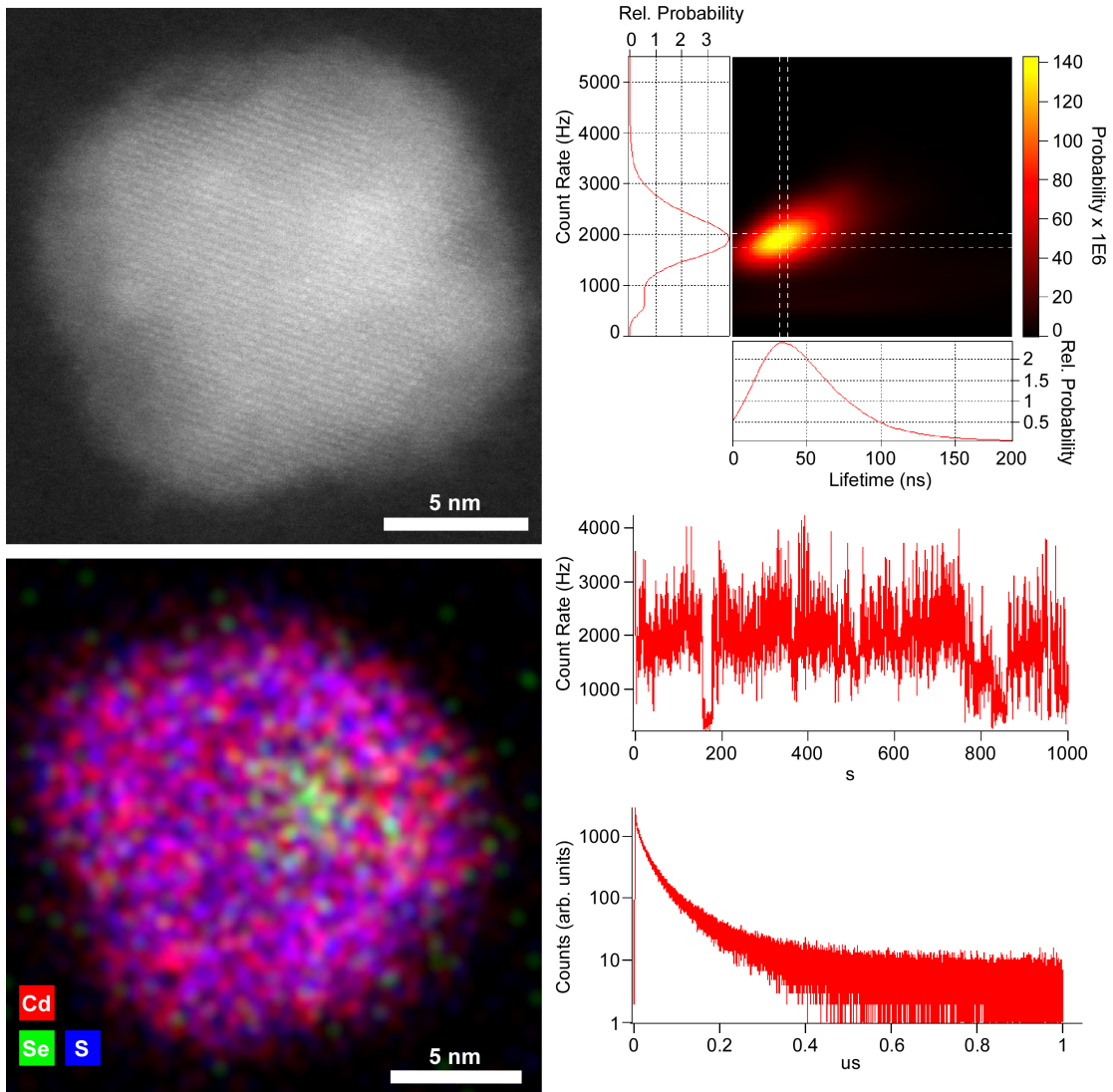


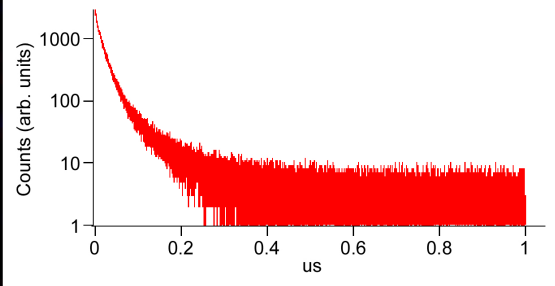
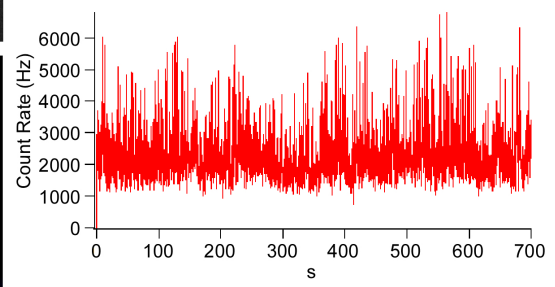
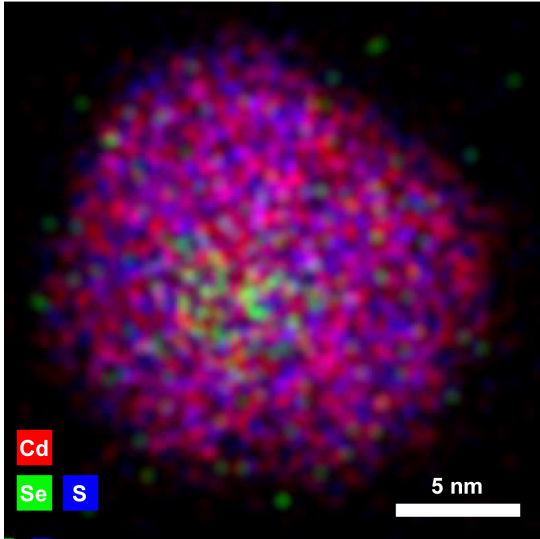
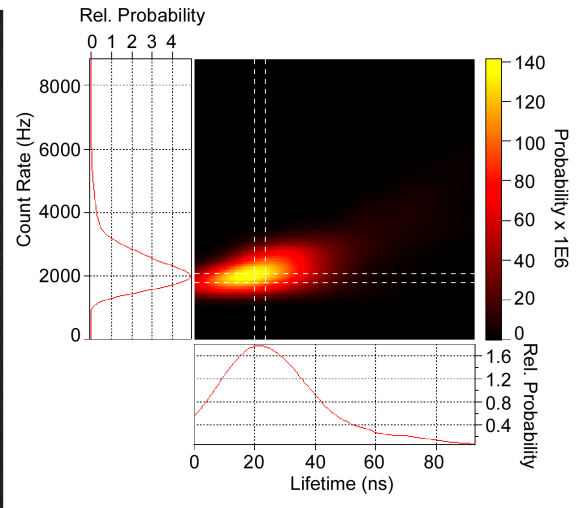
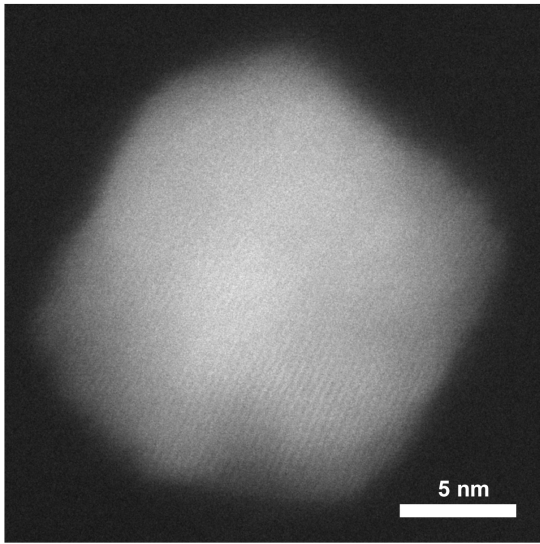


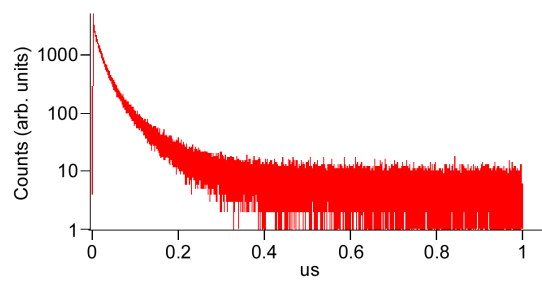
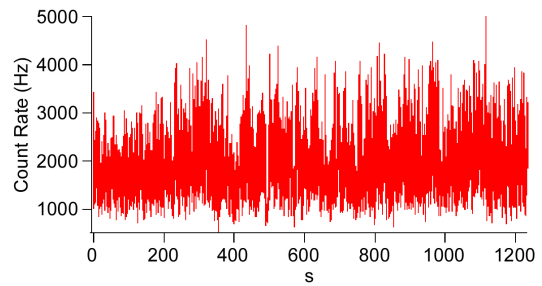
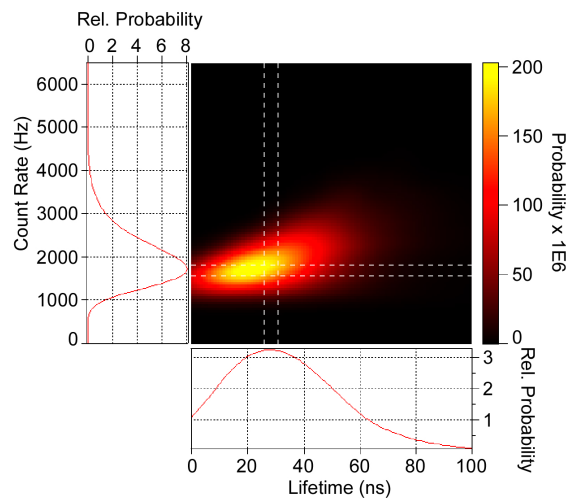
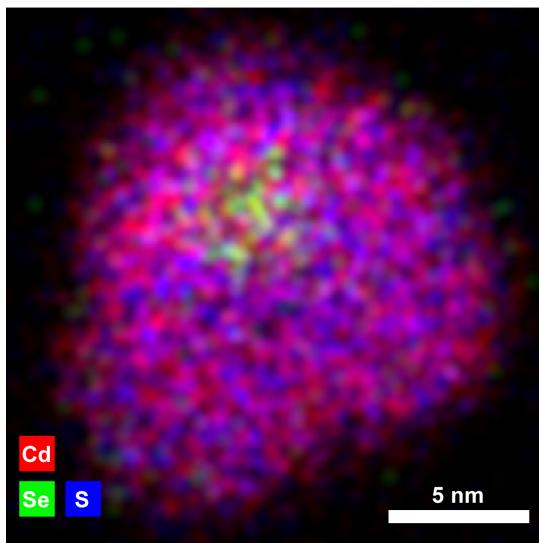
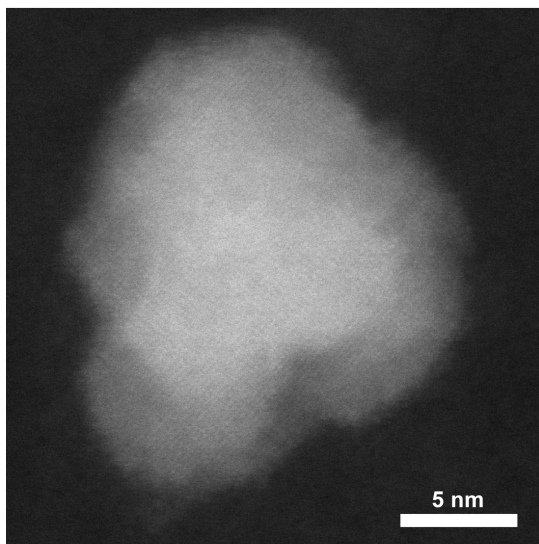


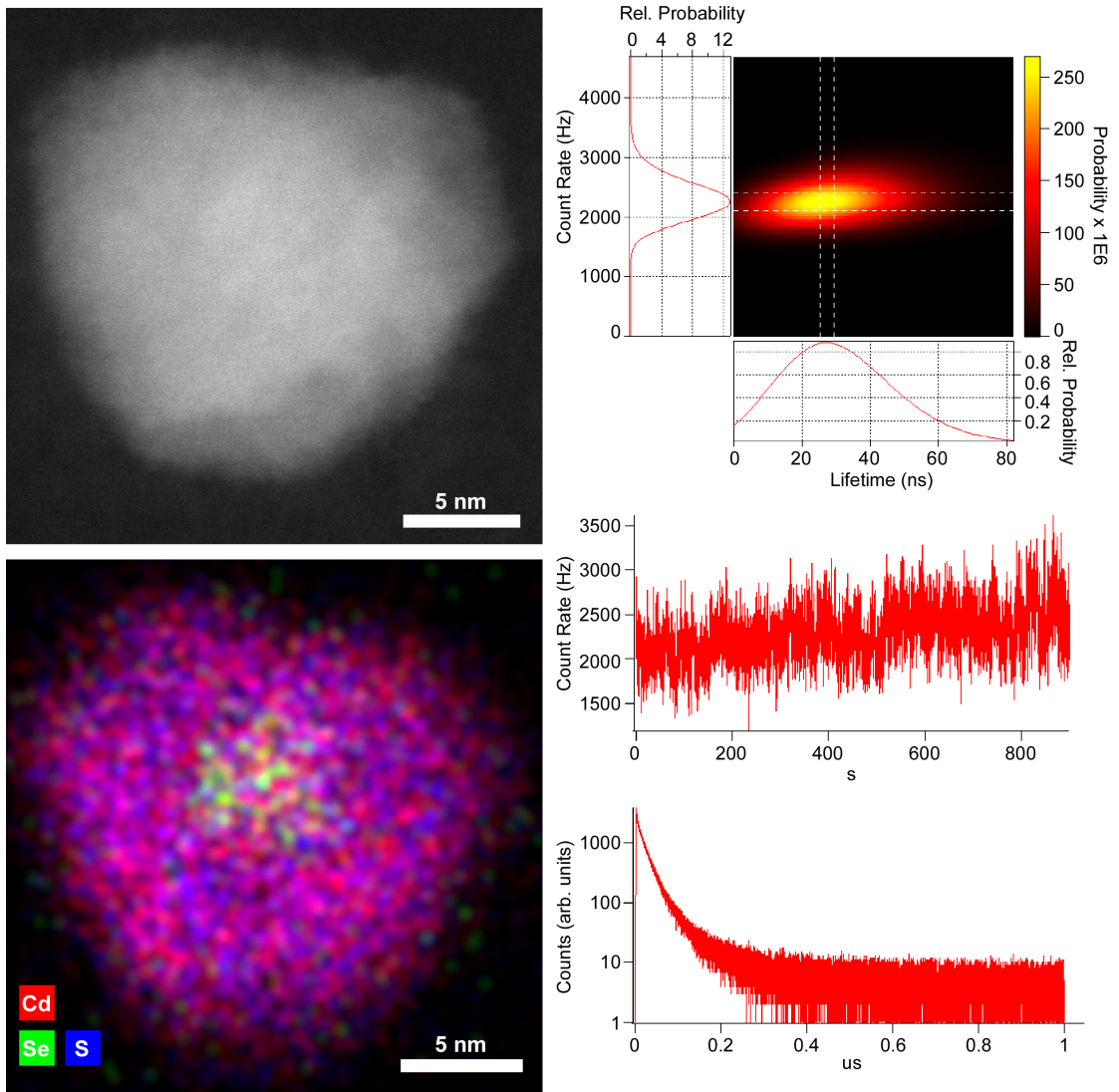


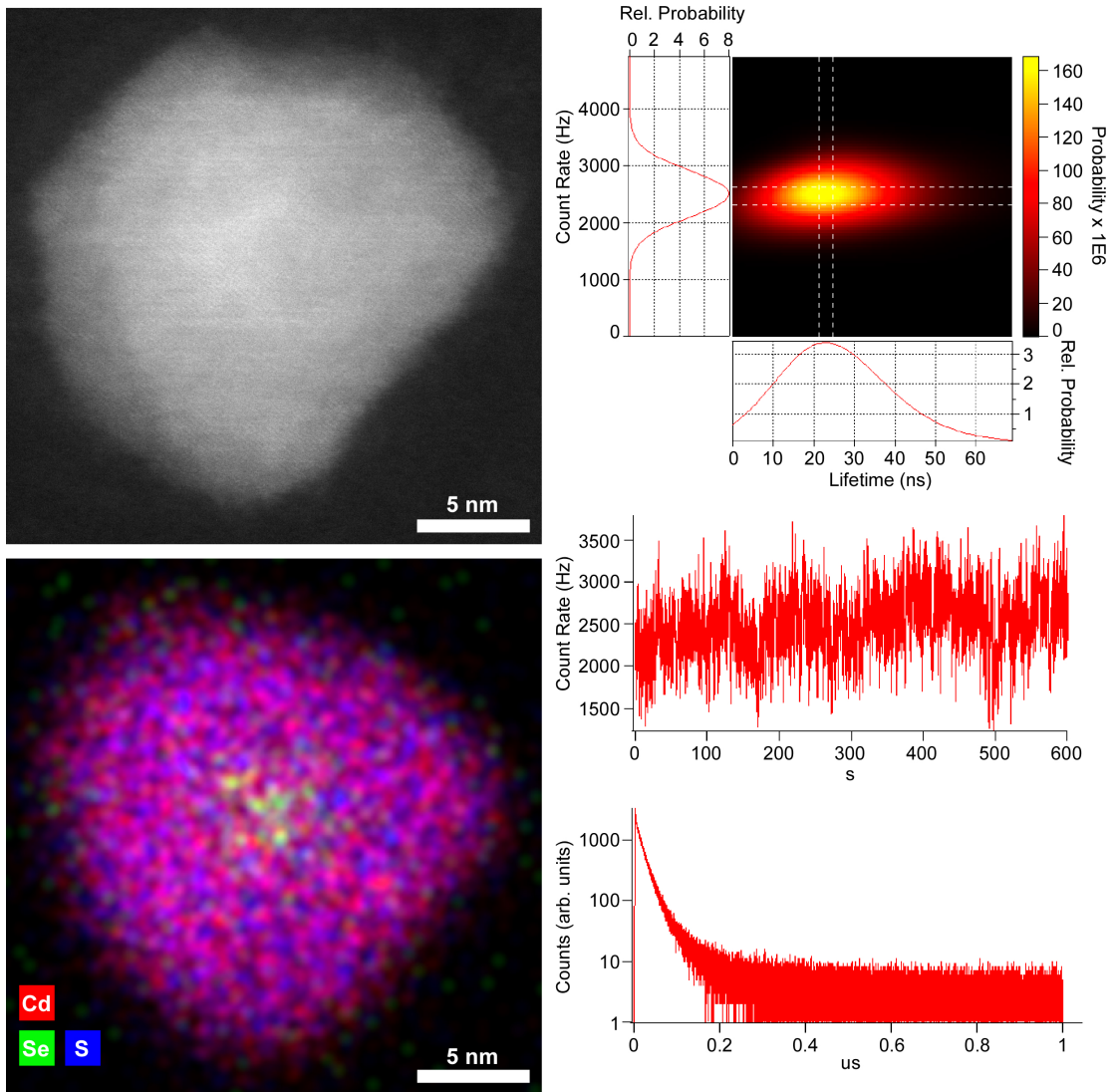


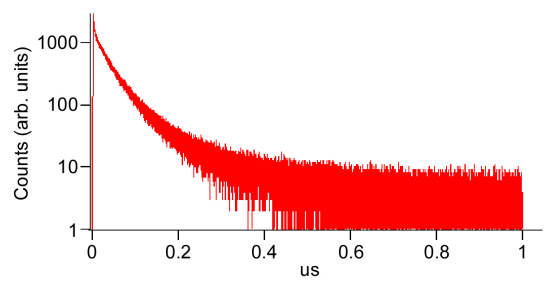
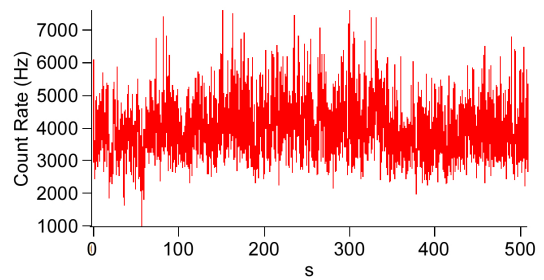
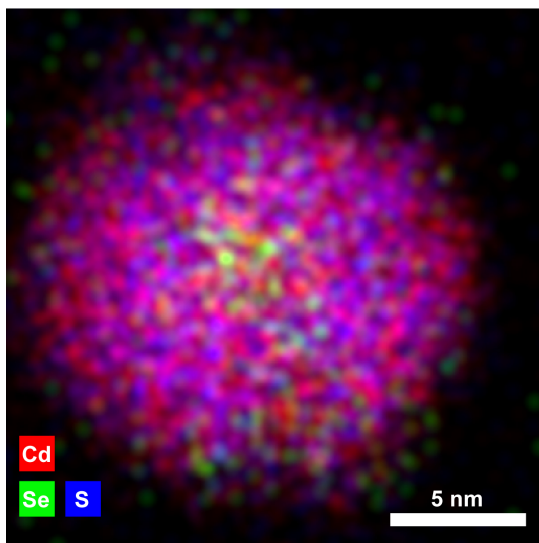
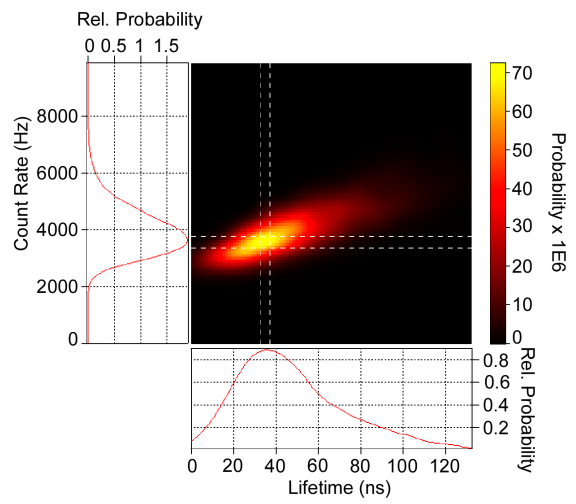
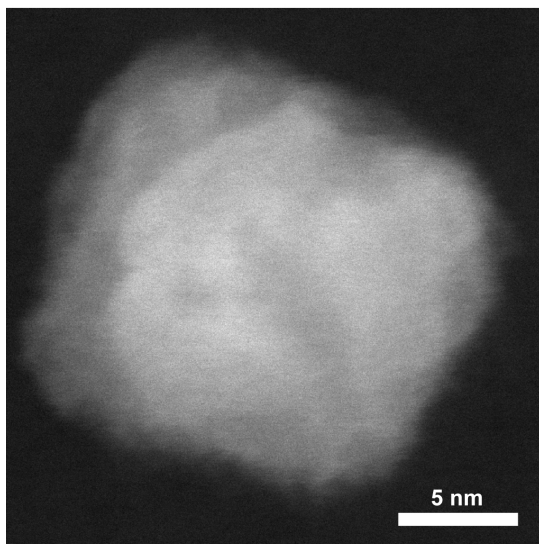


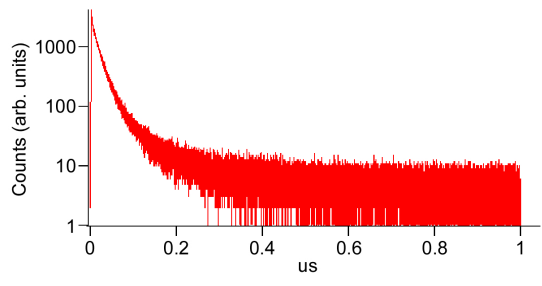
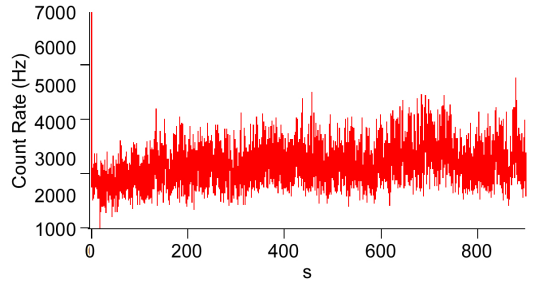
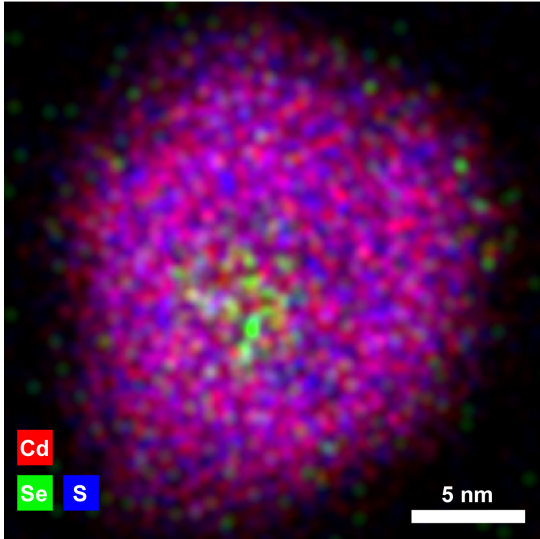
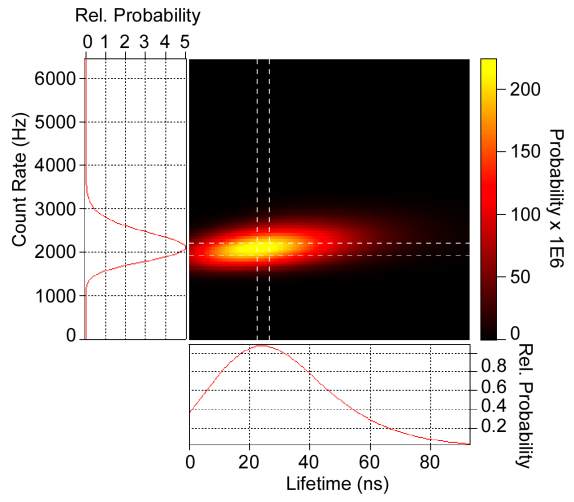
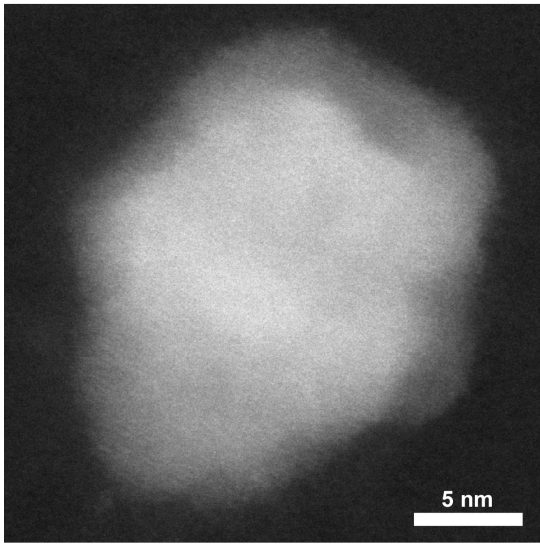


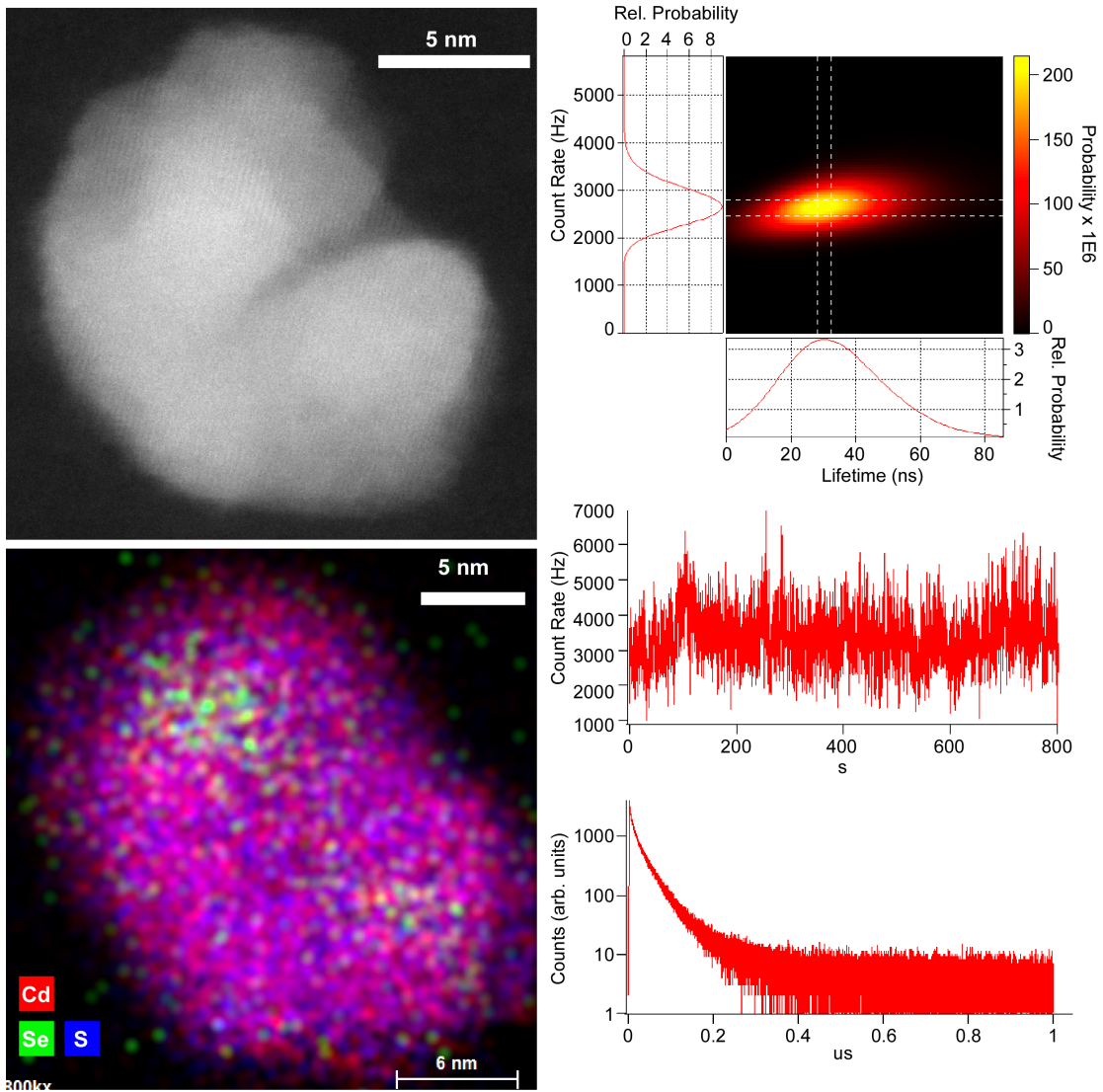


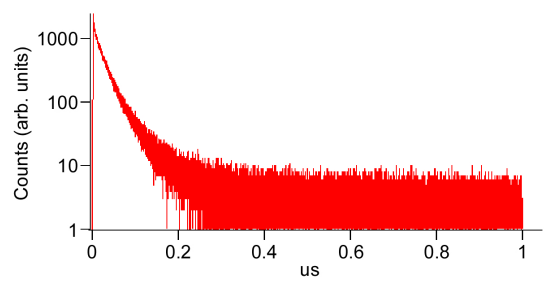
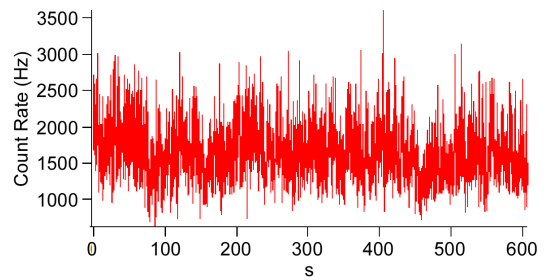
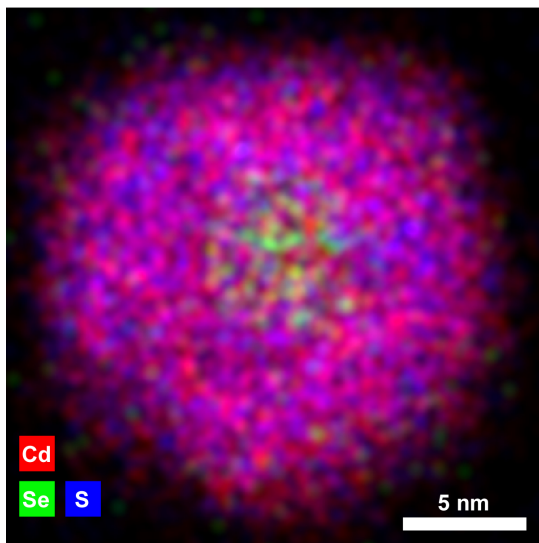
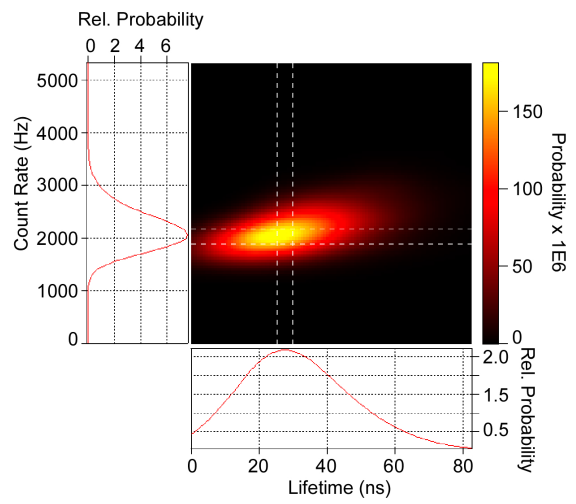
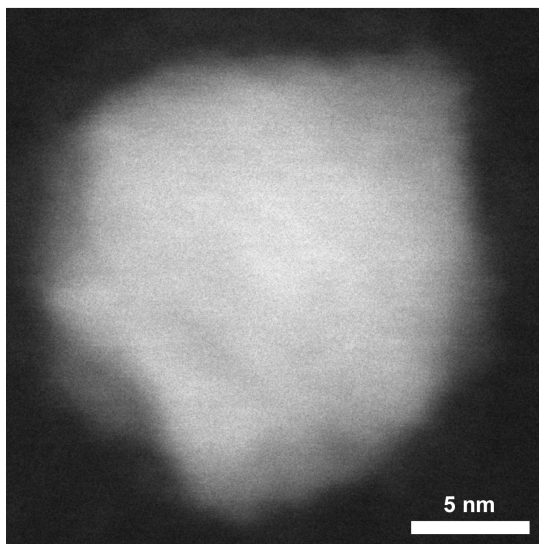


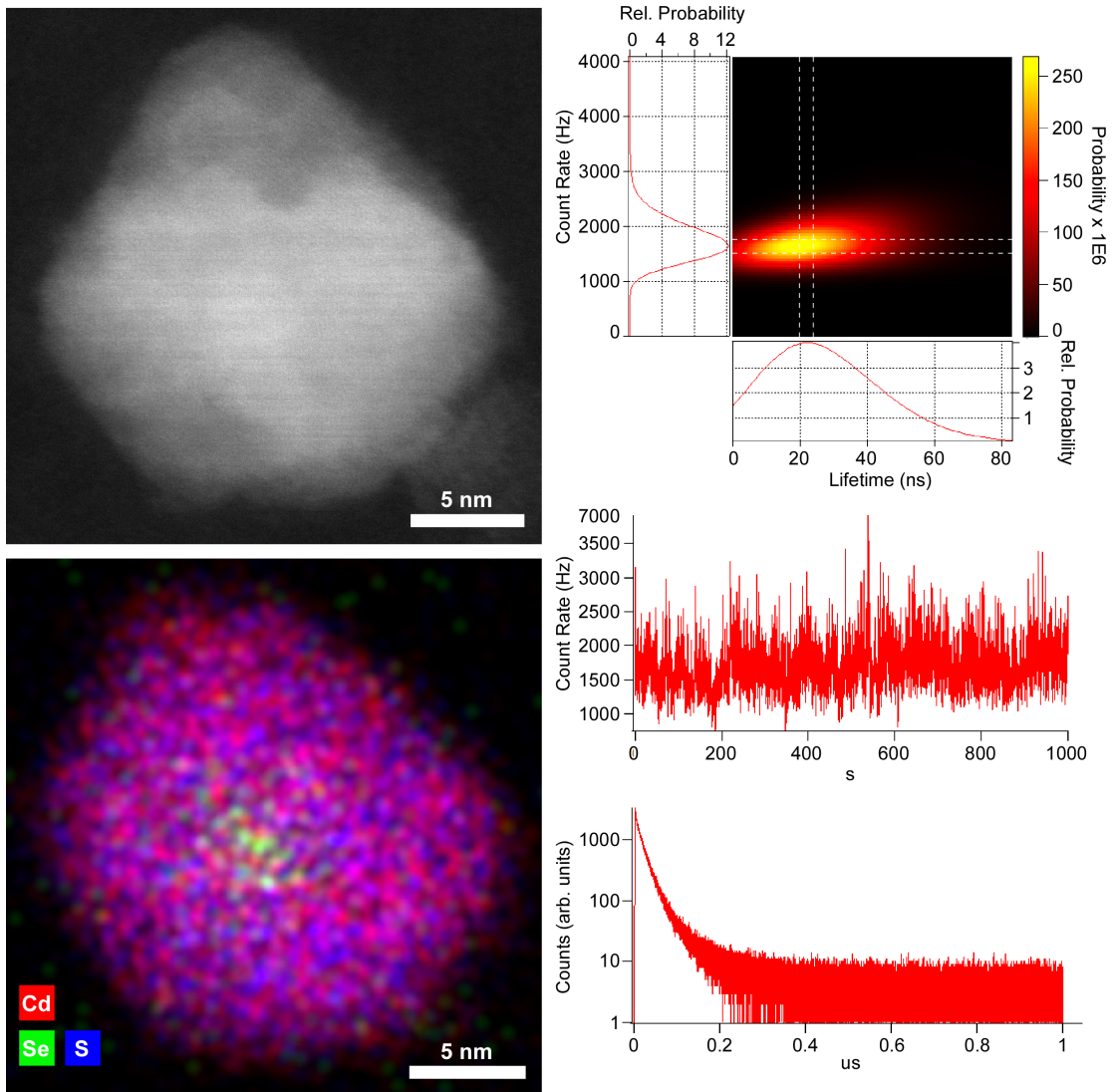


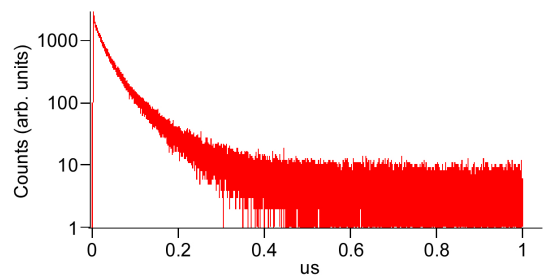
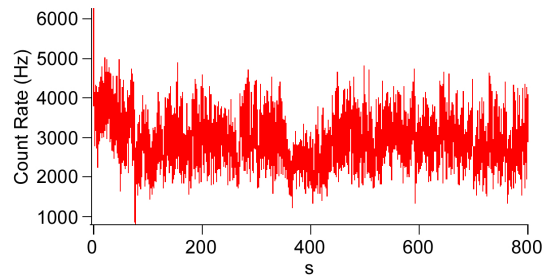
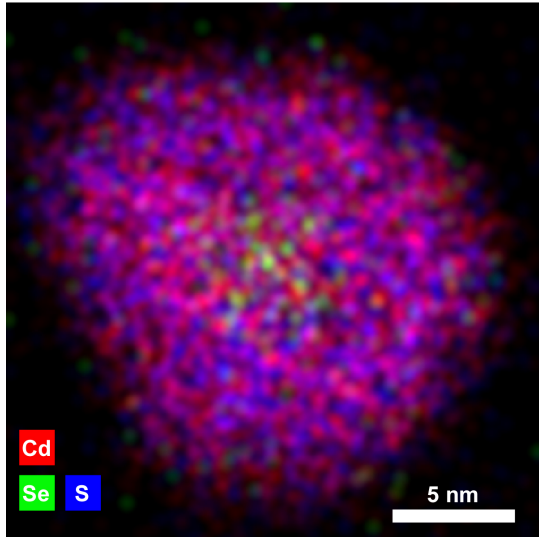
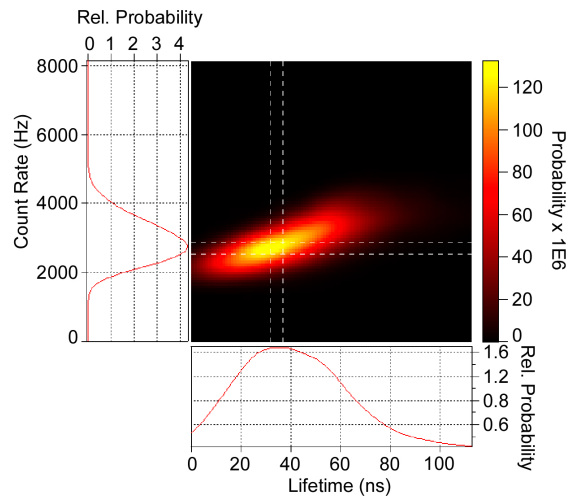
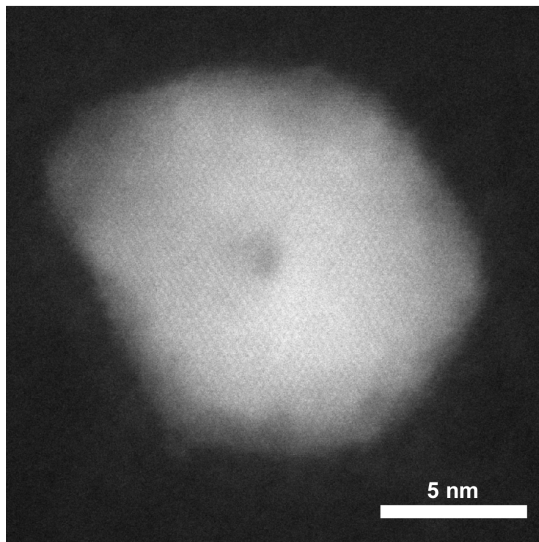


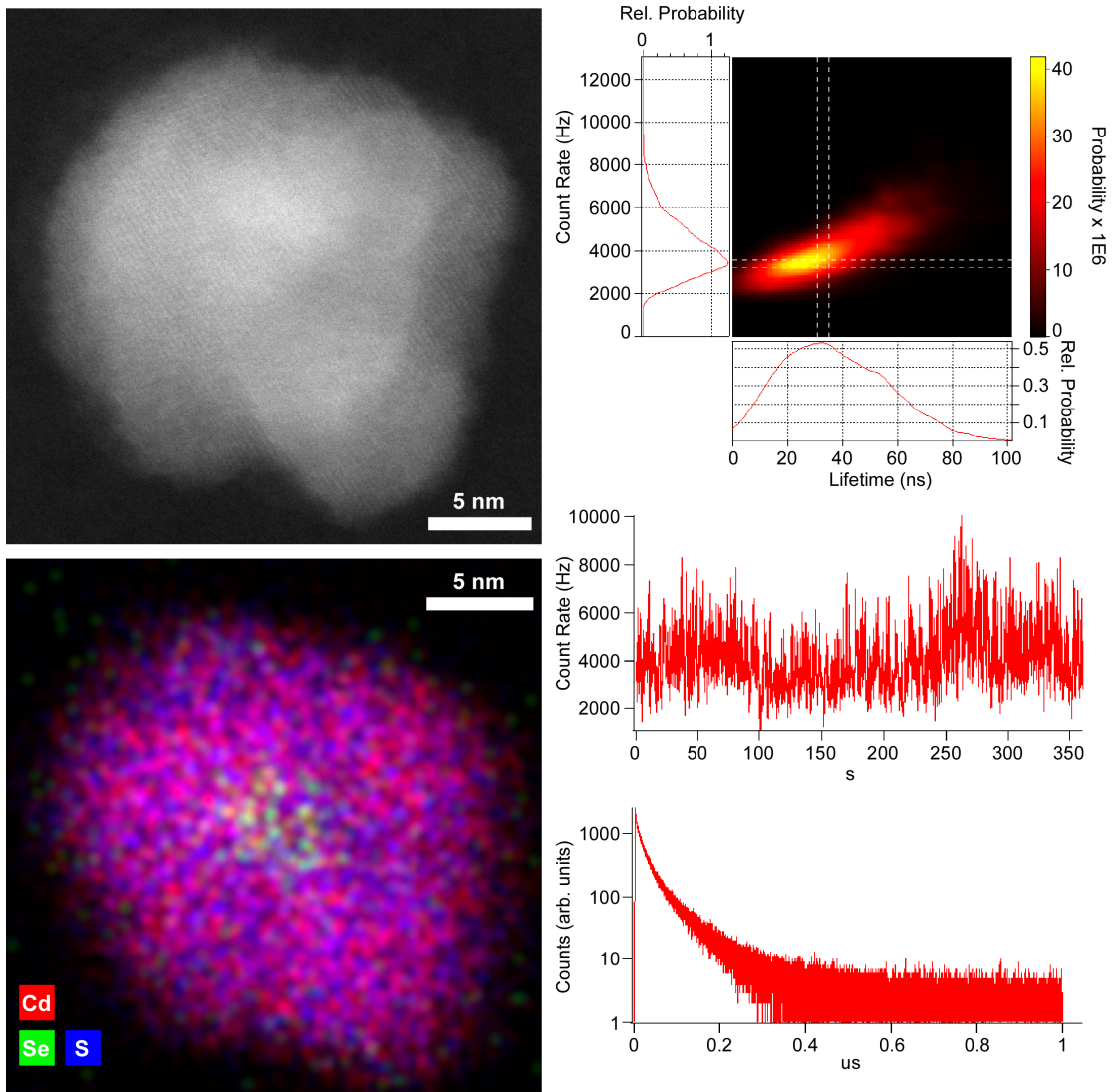


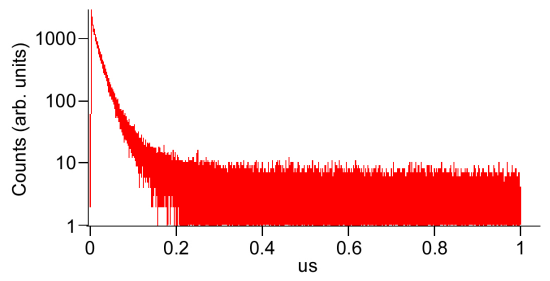
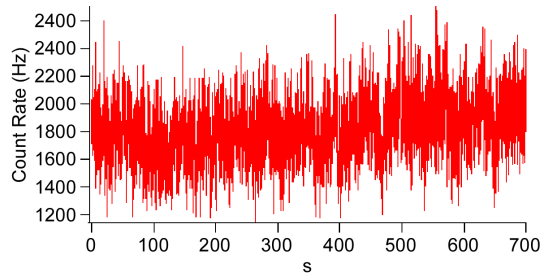
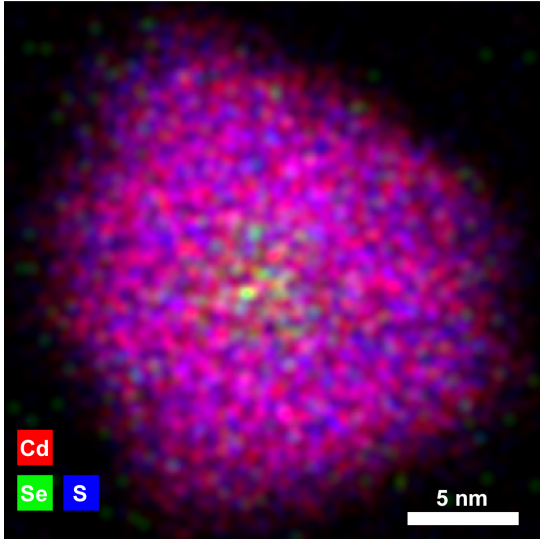
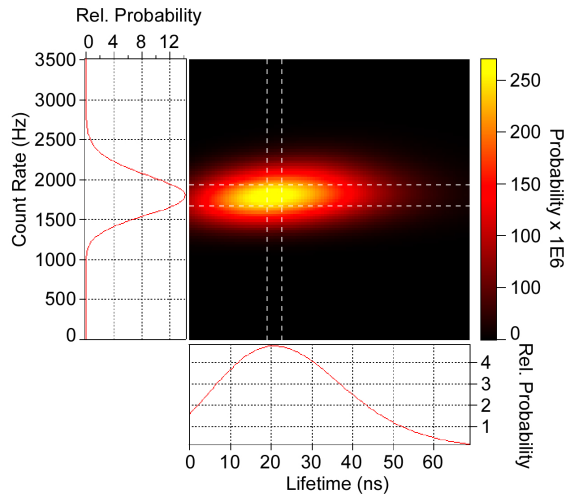
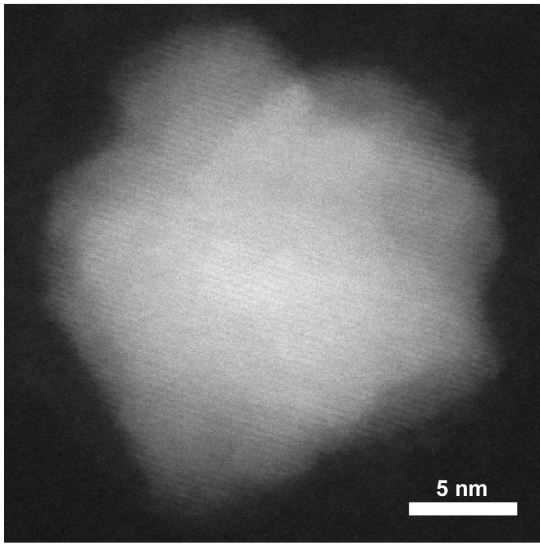












## Appendix C

### Measurement of Ensemble Quantum Dot Lifetime with the Rosenthal Lab Single Quantum Dot Microscope

Measurement of ensemble lifetime is a highly important tool used to characterize the optical and electrical properties of chemically synthesized fluorophores. Much of the time, the PLQY of a sample is not informative enough to fully describe the radiative and non-radiative fluorescence decay of the sample. Deviation of the measured fluorescence lifetime from monoexponential dynamics is an indication of a contribution from charge carrier trapping to the sample fluorescence, whether as an alternative fluorescence pathway or a process that results in nonradiative decay. When measured as a complementary analysis to PLQY measurement, decay lifetime measurements are a powerful tool that can even allow calculation of nonradiative decay rates. Further, the lifetime value can provide hints as to whether decay occurs *via* direct or indirect pathways, and can distinguish between fluorescence (short decay lifetime) and phosphorescence (long decay lifetime) in organic fluorophores.

The ensemble fluorescence decay traces presented in this appendix were collected with the time correlated single photon counting setup described in Section 1.4.

Due to possible photodegradation of samples, it is optimal to measure ensemble lifetime in deoxygenated solution, rather than in a solid thin film exposed to air. Additionally, measurement of samples in solution allows diffusion of different QDs in and out of the excitation volume, preventing excessive exposure to excitation and possible buildup of charge within the examined QDs.

Initial attempts to measure the ensemble PL of QDs in solution were hampered by the volatile nature of the organic solvents typically used to solubilize organic ligand-capped QDs. If dropping a solution of CdSe QDs in hexanes or toluene on a glass cover slide, for

example, the rapid evaporation of the solvent results in a constantly-changing concentration of QDs in the solution; also, frequently the solvent evaporates completely before the requisite collection period needed to obtain an adequate number of fluorescence counts for quantification of lifetime has passed.

For this reason, thin capillary tubes created from non-fluorescent glass were used for fluorescence collection. These capillaries can be diced to the desired size and dipped into the deoxygenated sample solution to fill. The low surface area of solution at the ends of the capillaries prevents rapid evaporation, and protects the solution from photooxidation. The width of the walls of the capillaries is 200  $\mu\text{m}$ ; the correction collar of the microscope objective can be adjusted to accommodate this width, and the excitation beam can be focused into the solution volume away from the inside surface of the capillary.

Most QD and nanocrystal fluorescence decay times are on the order of dozens to hundreds of nanoseconds. In some cases, fluorescence does not decay fully until several microseconds after excitation. For this reason, the 76 MHz frequency doubled beam from the Mira is not typically useful for accurate measurement of lifetime without emitted photons falling into a subsequent excitation period. Fortunately, the residual frequency doubled beam (400 nm) from the Coherent OPA has a repetition rate of 250 kHz, allowing for appropriate excitation of nanocrystalline emitters.

An example of fluorescence data of solution samples recorded with the 250 kHz excitation beam is shown in Figure C.1. Note that, if a 76 MHz beam had been used (one pulse per 13.6 ns), the full decay of these nanocrystalline rod samples would not have been collected. Further, rapid subsequent excitation of the same nanocrystals would result in a change of the decay dynamics of the nanocrystals.<sup>†</sup>

---

<sup>†</sup>It is important to note that in order to reduce pulse “pile-up,” the collection rate at each detector should not exceed 1 % of the excitation rate, or 2.5 kHz. This count rate is extremely low, increasing collection times of fluorescence decay traces. This count rate is certainly feasible, however, as the dark count rate on the single photon avalanche diodes is  $\sim 20$  counts per second.

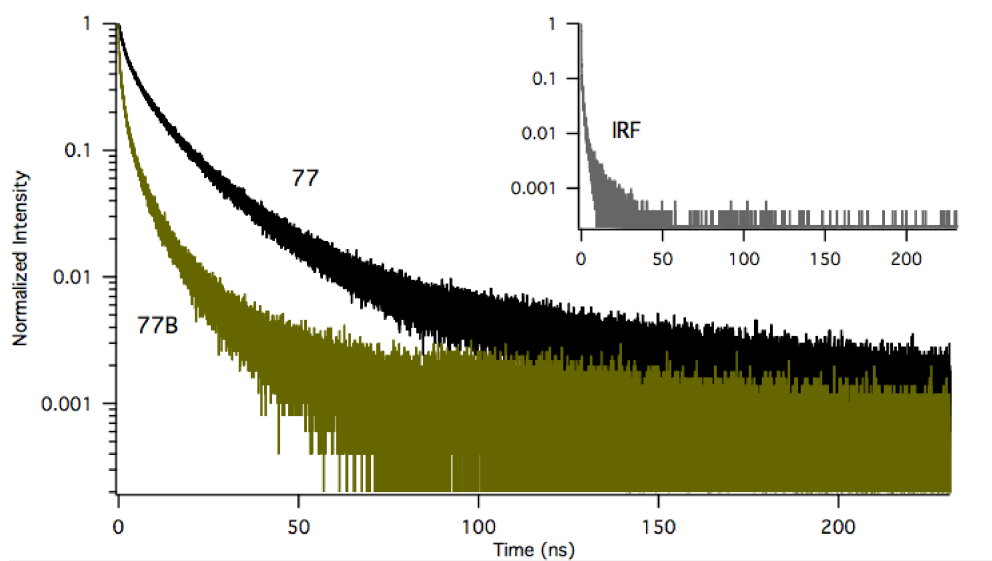


Figure C.1: **Fluorescence decay lifetime of CdSe/CdS core/shell nanorods.** Fluorescence decay of two nanorod samples with differing lifetimes in toluene. *Inset*-The instrument response function of the TCSPC system.

## Bibliography

- [1]DJ Norris, AL Efros, M Rosen, and MG Bawendi. Size Dependence of Exciton Fine Structure in CdSe Quantum Dots. *Physical Review B*, 53(24):16347–16354, 1996. DOI: <http://dx.doi.org/10.1103/PhysRevB.53.16347>.
- [2]CB Murray, DJ Norris, and Bawendi MG. Synthesis and Characterization of Nearly Monodisperse CdE (E = S, Se, Te) Semiconductor Nanocrystallites. *Journal of the American Chemical Society*, 115(19):8706–8715, 1993. DOI: 10.1021/ja00072a025.
- [3]WE Moerner and L Kador. Optical-Detection and Spectroscopy of Single Molecules. *Physical Review Letters*, 62(21):2535–2538, 1989. DOI: <http://dx.doi.org/10.1103/PhysRevLett.62.2535>.
- [4]WE Moerner and DP Fromm. Methods of Single-Molecule Fluorescence Spectroscopy and Microscopy. *Review of Scientific Instruments*, 74(8):3597–3619, 2003. DOI: <http://dx.doi.org/10.1063/1.1589587>.
- [5]SM Nie and SR Emery. Probing Single Molecules and Single Nanoparticles by Surface-Enhanced Raman Scattering. *Science*, 275(5303):1102–1106, 1997. DOI: 10.1126/science.275.5303.1102.
- [6]M N’Gom, J Ringnalda, JF Mansfield, A Agarwal, N Kotov, NJ Zaluzec, and TB Norris. Single Particle Plasmon Spectroscopy of Silver Nanowires and Gold Nanorods. *Nano Letters*, 8(10):3200–3204, 2008. DOI: 10.1021/nl801504v.
- [7]OL Muskens, N Del Fatti, F Vallee, JR Huntzinger, P Billaud, and M Broyer. Single Metal Nanoparticle Absorption Spectroscopy and Optical Characterization. *Applied Physics Letters*, 88(6), 2006. DOI: <http://dx.doi.org/10.1063/1.2172143>.
- [8]OL Muskens, G Bachelier, N Del Fatti, F Vallee, A Brioude, XC Jiang, and MP Pileni.

- Quantitative Absorption Spectroscopy of a Single Gold Nanorod. *Journal of Physical Chemistry C*, 112(24):8917–8921, 2008. DOI: 10.1021/jp8012865.
- [9]M Kuno, DP Fromm, HF Hamann, A Gallagher, and DJ Nesbitt. “On”/“Off” Fluorescence Intermittency of Single Semiconductor Quantum Dots. *Journal of Chemical Physics*, 115(2):1028–1040, 2001. DOI: <http://dx.doi.org/10.1063/1.1377883>.
- [10]LE Brus. Electron-Electron and Electron-Hole Interactions in Small Semiconductor Crystallites - The Size Dependence of the Lowest Excited Electronic State. *Journal of Chemical Physics*, 80(9):4403–4409, 1984. DOI: <http://dx.doi.org/10.1063/1.447218>.
- [11]SJ Rosenthal, A Tomlinson, EM Adkins, S Schroeter, S Adams, L Swafford, J McBride, YQ Wang, LJ DeFelice, and RD Blakely. Targeting Cell Surface Receptors with Ligand-Conjugated Nanocrystals. *Journal of the American Chemical Society*, 124(17):4586–4594, 2002. DOI: 10.1021/ja003486s.
- [12]JM Caruge, JE Halpert, V Wood, V Bulovic, and MG Bawendi. Colloidal Quantum-Dot Light-Emitting Diodes with Metal-Oxide Charge Transport Layers. *Nature Photonics*, 2(4):247–250, 2008. DOI: 10.1038/nphoton.2008.34.
- [13]VI Klimov, AA Mikhailovsky, S Xu, A Malko, JA Hollingsworth, CA Leatherdale, HJ Eisler, and MG Bawendi. Optical Gain and Stimulated Emission in Nanocrystal Quantum Dots. *Science*, 290(5490):314–317, 2000. DOI: 10.1126/science.290.5490.314.
- [14]AJ Chatten, KWJ Barnham, BF Buxton, NJ Ekins-Daukes, and MA Malik. Quantum Dot Solar Concentrators. *Semiconductors*, 38(8):909–917, 2004. DOI: 10.1134/1.1787111.
- [15]I Coropceanu and MG Bawendi. Core/Shell Quantum Dot Based Luminescent Solar Concentrators with Reduced Reabsorption and Enhanced Efficiency. *Nano Letters*, 14(7):4097–4101, 2014. DOI: 10.1021/nl501627e.

- [16] F Meinardi, A Colombo, KA Velizhanin, R Simonutti, M Lorenzon, L Beverina, R Viswanatha, VI Klimov, and S Brovelli. Large-Area Luminescent Solar Concentrators Based on ‘Stokes-Shift-Engineered’ Nanocrystals in a Mass-Polymerized PMMA Matrix. *Nature Photonics*, 8(5):392–399, 2014. DOI: 10.1038/nphoton.2014.54.
- [17] JP Clifford, G Konstantatos, KW Johnston, S Hoogland, L Levina, and EH Sargent. Fast, Sensitive and Spectrally Tuneable Colloidal Quantum-Dot Photodetectors. *Nature Nanotechnology*, 4(1):40–44, 2009. DOI: 10.1038/nnano.2008.313.
- [18] J Bao and MG Bawendi. A Colloidal Quantum Dot Spectrometer. *Nature*, 523(7558):67–70, 2015. DOI:10.1038/nature14576.
- [19] AG Pattantyus-Abraham, IJ Kramer, AR Barkhouse, XH Wang, G Konstantatos, R Debnath, L Levina, I Raabe, MK Nazeeruddin, M Gratzel, and EH Sargent. Depleted-Heterojunction Colloidal Quantum Dot Solar Cells. *ACS Nano*, 4(6):3374–3380, 2010. DOI: 10.1021/nn100335g.
- [20] M Nirmal, BO Dabbousi, MG Bawendi, JJ Macklin, JK Trautman, TD Harris, and LE Brus. Fluorescence Intermittency in Single Cadmium Selenide Nanocrystals. *Nature*, 383(6603):802–804, 1996. DOI: 10.1038/383802a0.
- [21] G Margolin, V Protasenko, M Kuno, and E Barkai. Photon Counting Statistics for Blinking CdSe-ZnS Quantum Dots: A Levy Walk Process. *Journal of Physical Chemistry B*, 110(38):19053–19060, 2006. DOI: 10.1021/jp061487m.
- [22] K Goushi, T Yamada, and A Otomo. Excitation Intensity Dependence of Power-Law Blinking Statistics in Nanocrystal Quantum Dots. *Journal of Physical Chemistry C*, 113(47):20161–20168, 2009. DOI: 10.1021/jp811448k.
- [23] M Haase, CG Hubner, E Reuther, A Herrmann, K Mullen, and T Basche. Exponential and Power-Law Kinetics in Single-Molecule Fluorescence Intermittency. *Journal of Physical Chemistry B*, 108(29):10445–10450, 2004. DOI: 10.1021/jp0313674.

- [24]PH Sher, JM Smith, PA Dalgarno, RJ Warburton, X Chen, PJ Dobson, SM Daniels, NL Pickett, and P O'Brien. Power Law Carrier Dynamics in Semiconductor Nanocrystals at Nanosecond Timescales. *Applied Physics Letters*, 92(10), 2008. DOI: <http://dx.doi.org/10.1063/1.2894193>.
- [25]KT Shimizu, RG Neuhauser, CA Leatherdale, SA Empedocles, WK Woo, and MG Bawendi. Blinking Statistics in Single Semiconductor Nanocrystal Quantum Dots. *Physical Review B*, 63(20), 2001. DOI: <http://dx.doi.org/10.1103/PhysRevB.63.205316>.
- [26]M Kuno, DP Fromm, ST Johnson, A Gallagher, and DJ Nesbitt. Modeling Distributed Kinetics in Isolated Semiconductor Quantum Dots. *Physical Review B*, 67(12), 2003. DOI: <http://dx.doi.org/10.1103/PhysRevB.67.125304>.
- [27]M Califano. Off-State Quantum Yields in the Presence of Surface Trap States in CdSe Nanocrystals: The Inadequacy of the Charging Model to Explain Blinking. *Journal of Physical Chemistry C*, 115(37):18051–18054, 2011. DOI: 10.1021/jp203736y.
- [28]FM Gomez-Campos and M Califano. Hole Surface Trapping in CdSe Nanocrystals: Dynamics, Rate Fluctuations, and Implications for Blinking. *Nano Letters*, 12(9):4508–4517, 2012. DOI: 10.1021/nl3016279.
- [29]J Zhao, O Chen, DB Strassfeld, and MG Bawendi. Biexciton Quantum Yield Heterogeneities in Single CdSe (CdS) Core (Shell) Nanocrystals and Its Correlation to Exciton Blinking. *Nano Letters*, 12(9):4477–4483, 2012. DOI: 10.1021/nl3013727.
- [30]JM Caruge, YT Chan, V Sundar, HJ Eisler, and MG Bawendi. Transient Photoluminescence and Simultaneous Amplified Spontaneous Emission from Multiexciton States in CdSe Quantum Dots. *Physical Review B*, 70(8), 2004. DOI: <http://dx.doi.org/10.1103/PhysRevB.70.085316>.
- [31]B Fisher, JM Caruge, D Zehnder, and M Bawendi. Room-Temperature Ordered Photon

- Emission from Multiexciton States in Single CdSe Core-Shell Nanocrystals. *Physical Review Letters*, 94(8), 2005. DOI: <http://dx.doi.org/10.1103/PhysRevLett.94.087403>.
- [32]G Nair, J Zhao, and MG Bawendi. Biexciton Quantum Yield of Single Semiconductor Nanocrystals from Photon Statistics. *Nano Letters*, 11(3):1136–1140, 2011. DOI: 10.1021/nl104054t.
- [33]VI Klimov, JA McGuire, RD Schaller, and VI Rupasov. Scaling of Multiexciton Lifetimes in Semiconductor Nanocrystals. *Physical Review B*, 77(19):195324, 2008. DOI: <http://dx.doi.org/10.1103/PhysRevB.77.195324>.
- [34]PA Frantsuzov, S Volkan-Kacso, and B Janko. Universality of the Fluorescence Intermittency in Nanoscale Systems: Experiment and Theory. *Nano Letters*, 13(2):402–408, 2013. DOI: 10.1021/nl3035674.
- [35]PA Frantsuzov and RA Marcus. Explanation of Quantum Dot Blinking Without the Long-Lived Trap Hypothesis. *Physical Review B*, 72(15), 2005. DOI: <http://dx.doi.org/10.1103/PhysRevB.72.155321>.
- [36]PA Frantsuzov, S Volkan-Kacso, and B Janko. Model of Fluorescence Intermittency of Single Colloidal Semiconductor Quantum Dots Using Multiple Recombination Centers. *Physical Review Letters*, 103(20), 2009. DOI: <http://dx.doi.org/10.1103/PhysRevLett.103.207402>.
- [37]P Frantsuzov, M Kuno, B Janko, and RA Marcus. Universal Emission Intermittency in Quantum Dots, Nanorods and Nanowires. *Nature Physics*, 4(7):519–522, 2008. DOI: 10.1038/nphys1001.
- [38]AA Cordones, TJ Bixby, and SR Leone. Evidence for Multiple Trapping Mechanisms in Single CdSe/ZnS Quantum Dots from Fluorescence Intermittency Measurements over a Wide Range of Excitation Intensities. *Journal of Physical Chemistry C*, 115(14):6341–6349, 2011. DOI: 10.1021/jp2001223.

- [39]AA Cordones and SR Leone. Mechanisms for Charge Trapping in Single Semiconductor Nanocrystals Probed by Fluorescence Blinking. *Chemical Society Reviews*, 42(8):3209–3221, 2013. DOI: 10.1039/C2CS35452G.
- [40]C Galland, Y Ghosh, A Steinbruck, M Sykora, JA Hollingsworth, VI Klimov, and H Htoon. Two Types of Luminescence Blinking Revealed by Spectroelectrochemistry of Single Quantum Dots. *Nature*, 479(7372):203–207, 2011. DOI: 10.1038/nature10569.
- [41]W Qin and P Guyot-Sionnest. Evidence for the Role of Holes in Blinking: Negative and Oxidized CdSe/CdS Dots. *ACS Nano*, 6(10):9125–9132, 2012. DOI: 10.1021/nn303396c.
- [42]SA Empedocles and MG Bawendi. Quantum-Confined Stark Effect in Single CdSe Nanocrystallite Quantum Dots. *Science*, 278(5346):2114–2117, 1997. DOI: 10.1126/science.278.5346.2114.
- [43]SA Empedocles and MG Bawendi. Influence of Spectral Diffusion on the Line Shapes of Single CdSe Nanocrystallite Quantum Dots. *Journal of Physical Chemistry B*, 103(11):1826–1830, 1999. DOI: 10.1021/jp983305x.
- [44]M Fox. *Quantum Optics*. Oxford University Press, 2006.
- [45]Y Ebenstein, T Mokari, and U Banin. Fluorescence Quantum Yield of Cd-Se/ZnS Nanocrystals Investigated by Correlated Atomic-Force and Single-Particle Fluorescence Microscopy. *Applied Physics Letters*, 80(21):4033–4035, 2002. DOI: <http://dx.doi.org/10.1063/1.1482785>.
- [46]S Wang, C Querner, MD Fischbein, L Willis, DS Novikov, CH Crouch, and M Drndic. Blinking Statistics Correlated with Nanoparticle Number. *Nano Letters*, 8(11):4020–4026, 2008. DOI: 10.1021/nl802696f.

- [47]P Michler, A Imamoglu, MD Mason, PJ Carson, GF Strouse, and SK Buratto. Quantum Correlation Among Photons from a Single Quantum Dot at Room Temperature. *Nature*, 406(6799):968–970, 2000. DOI: 10.1038/35023100.
- [48]HJ Kimble, M Dagenais, and L Mandel. Photon Antibunching in Resonance Fluorescence. *Physical Review Letters*, 39(11):691–695, 1977. DOI: <http://dx.doi.org/10.1103/PhysRevLett.39.691>.
- [49]G Messin, JP Hermier, E Giacobino, P Desbiolles, and M Dahan. Bunching and Antibunching in the Fluorescence of Semiconductor Nanocrystals. *Optics Letters*, 26(23):1891–1893, 2001. DOI: 10.1364/OL.26.001891.
- [50]V Zwiller, H Blom, P Jonsson, N Panev, S Jeppesen, T Tsegaye, E Goobar, ME Pistol, L Samuelson, and G Bjork. Single Quantum Dots Emit Single Photons at a Time: Antibunching Experiments. *Applied Physics Letters*, 78(17):2476–2478, 2001. DOI: <http://dx.doi.org/10.1063/1.1366367>.
- [51]F Garcia-Santamaria, YF Chen, J Vela, RD Schaller, JA Hollingsworth, and VI Klimov. Suppressed Auger Recombination in “Giant” Nanocrystals Boosts Optical Gain Performance. *Nano Letters*, 9(10):3482–3488, 2009. DOI: 10.1021/nl901681d.
- [52]JR McBride, TC Kippeny, SJ Pennycook, and SJ Rosenthal. Aberration-Corrected Z-Contrast Scanning Transmission Electron Microscopy of CdSe Nanocrystals. *Nano Letters*, 4(7):1279–1283, 2004. DOI: 10.1021/nl049406q.
- [53]J McBride, J Treadway, LC Feldman, SJ Pennycook, and SJ Rosenthal. Structural Basis for Near Unity Quantum Yield Core/Shell Nanostructures. *Nano Letters*, 6(7):1496–1501, 2006. DOI: 10.1021/nl060993k.
- [54]AD Dukes, PC Samson, JD Keene, LM Davis, JP Wikswo, and SJ Rosenthal. Single-Nanocrystal Spectroscopy of White-Light-Emitting CdSe Nanocrystals. *Journal of Physical Chemistry A*, 115(16):4076–4081, 2011. DOI: 10.1021/jp1109509.

- [55]JD Keene, JR McBride, NJ Orfield, and SJ Rosenthal. Elimination of Hole-Surface Overlap in Graded CdS<sub>x</sub>Se<sub>1-x</sub> Nanocrystals Revealed by Ultrafast Fluorescence Upconversion Spectroscopy. *ACS Nano*, 8(10):10665–10673, 2014. DOI: 10.1021/nn504235w.
- [56]Nyquist Calculator. *svi.nl/NyquistCalculator*, 2015.
- [57]CB Murray, CR Kagan, and MG Bawendi. Synthesis and Characterization of Monodisperse Nanocrystals and Close-Packed Nanocrystal Assemblies. *Annual Review of Materials Science*, 30:545–610, 2000. DOI: 10.1146/annurev.matsci.30.1.545.
- [58]M Achermann, MA Petruska, DD Koleske, MH Crawford, and VI Klimov. Nanocrystal-Based Light-Emitting Diodes Utilizing High-Efficiency Nonradiative Energy Transfer for Color Conversion. *Nano Letters*, 6(7):1396–1400, 2006. DOI: 10.1021/nl060392t.
- [59]PO Anikeeva, JE Halpert, MG Bawendi, and V Bulovic. Quantum Dot Light-Emitting Devices with Electroluminescence Tunable over the Entire Visible Spectrum. *Nano Letters*, 9(7):2532–2536, 2009. DOI: 10.1021/nl9002969.
- [60]TH Kim, KS Cho, EK Lee, SJ Lee, J Chae, JW Kim, DH Kim, JY Kwon, G Amaratunga, SY Lee, BL Choi, Y Kuk, JM Kim, and K Kim. Full-Colour Quantum Dot Displays Fabricated by Transfer Printing. *Nature Photonics*, 5(3):176–182, 2011. DOI: 10.1038/nphoton.2011.12.
- [61]VI Klimov, AA Mikhailovsky, DW McBranch, CA Leatherdale, and MG Bawendi. Quantization of Multiparticle Auger Rates in Semiconductor Quantum Dots. *Science*, 287(5455):1011–1013, 2000. DOI: 10.1126/science.287.5455.1011.
- [62]JC Chang and SJ Rosenthal. A Bright Light to Reveal Mobility: Single Quantum Dot Tracking Reveals Membrane Dynamics and Cellular Mechanisms. *Journal of Physical Chemistry Letters*, 4(17):2858–2866, 2013. DOI: 10.1021/jz401071g.

- [63]AL Efros and M Rosen. Random Telegraph Signal in the Photoluminescence Intensity of a Single Quantum Dot. *Physical Review Letters*, 78(6):1110–1113, 1997. DOI: <http://dx.doi.org/10.1103/PhysRevLett.78.1110>.
- [64]M Kuno, DP Fromm, HF Hamann, A Gallagher, and DJ Nesbitt. Nonexponential “Blinking” Kinetics of Single CdSe Quantum Dots: A Universal Power Law Behavior. *Journal of Chemical Physics*, 112(7):3117–3120, 2000. DOI: <http://dx.doi.org/10.1063/1.480896>.
- [65]PP Jha and P Guyot-Sionnest. Trion Decay in Colloidal Quantum Dots. *ACS Nano*, 3(4):1011–1015, 2009. DOI: 10.1021/nn9001177.
- [66]M Ye and PC Searson. Blinking in Quantum Dots: The Origin of the Grey State and Power Law Statistics. *Physical Review B*, 84(12), 2011. DOI: <http://dx.doi.org/10.1103/PhysRevB.84.125317>.
- [67]MA Hines and P Guyot-Sionnest. Synthesis and Characterization of Strongly Luminescing ZnS-Capped CdSe Nanocrystals. *Journal of Physical Chemistry*, 100(2):468–471, 1996. DOI: 10.1021/jp9530562.
- [68]Y Chen, J Vela, H Htoon, JL Casson, DJ Werder, DA Bussian, VI Klimov, and JA Hollingsworth. “Giant” Multishell CdSe Nanocrystal Quantum Dots with Suppressed Blinking. *Journal of the American Chemical Society*, 130(15):5026–5027, 2008. DOI: 10.1021/ja711379k.
- [69]XY Wang, XF Ren, K Kahen, MA Hahn, M Rajeswaran, S Maccagnano-Zacher, J Silcox, GE Cragg, AL Efros, and TD Krauss. Non-blinking Semiconductor Nanocrystals. *Nature*, 459(7247):686–689, 2009. DOI: 10.1038/nature08072.
- [70]YS Park, WK Bae, LA Padilha, JM Pietryga, and VI Klimov. Effect of the Core/Shell Interface on Auger Recombination Evaluated by Single-Quantum-Dot Spectroscopy. *Nano Letters*, 14(2):396–402, 2014. DOI: 10.1021/nl403289w.

- [71]Y Ghosh, BD Mangum, JL Casson, DJ Williams, H Htoon, and JA Hollingsworth. New Insights into the Complexities of Shell Growth and the Strong Influence of Particle Volume in Nonblinking “Giant” Core/Shell Nanocrystal Quantum Dots. *Journal of the American Chemical Society*, 134(23):9634–9643, 2012. DOI: 10.1021/ja212032q.
- [72]KA Lidke, B Rieger, TM Jovin, and R Heintzmann. Superresolution by Localization of Quantum Dots Using Blinking Statistics. *Optics Express*, 13(18):7052–7062, 2005. DOI: 10.1364/OPEX.13.007052.
- [73]Y Wang, G Fruhwirth, E Cai, T Ng, and PR Selvin. 3D Super-Resolution Imaging with Blinking Quantum Dots. *Nano Letters*, 13(11):5233–5241, 2013. DOI: 10.1021/nl4026665.
- [74]AP Alivisatos. Perspectives on the Physical Chemistry of Semiconductor Nanocrystals. *Journal of Physical Chemistry*, 100(31):13226–13239, 1996. DOI: 10.1021/jp9535506.
- [75]SA Empedocles, R Neuhauser, K Shimizu, and MG Bawendi. Photoluminescence from Single Semiconductor Nanostructures. *Advanced Materials*, 11(15):1243–1256, 1999. DOI: 10.1002/(SICI)1521-4095(199910)11:15<1243::AID-ADMA1243>3.0.CO;2-2.
- [76]D Vanmaekelbergh and M Casavola. Single-Dot Microscopy and Spectroscopy for Comprehensive Study of Colloidal Nanocrystals. *Journal of Physical Chemistry Letters*, 2(16):2024–2031, 2011. DOI: 10.1021/jz200713j.
- [77]S Mangel, E Aronovitch, AN Enyashin, L Houben, and M Bar-Sadan. Atomic-Scale Evolution of a Growing Core-Shell Nanoparticle. *Journal of the American Chemical Society*, 136(36):12564–12567, 2014. DOI: 10.1021/ja506323s.
- [78]RM Dickson. Structure Determines Function in Nanoparticles, Their Interfaces, and Their Assemblies. *Journal of Physical Chemistry Letters*, 2(16):2044–2045, 2011. DOI: 10.1021/jz200981k.

- [79]MJ Fernee, T Plakhotnik, Y Louyer, BN Littleton, C Potzner, P Tamarat, P Mulvaney, and B Lounis. Spontaneous Spectral Diffusion in CdSe Quantum Dots. *Journal of Physical Chemistry Letters*, 3(12):1716–1720, 2012. DOI: 10.1021/jz300456h.
- [80]F Koberling, A Mews, G Philipp, U Kolb, I Potapova, M Burghard, and T Basche. Fluorescence Spectroscopy and Transmission Electron Microscopy of the Same Isolated Semiconductor Nanocrystals. *Applied Physics Letters*, 81(6):1116–1118, 2002. DOI: <http://dx.doi.org/10.1063/1.1499221>.
- [81]F Koberling, U Kolb, G Philipp, I Potapova, T Basche, and A Mews. Fluorescence Anisotropy and Crystal Structure of Individual Semiconductor Nanocrystals. *Journal of Physical Chemistry B*, 107(30):7463–7471, 2003. DOI: 10.1021/jp027800b.
- [82]ZY Chen, S Berciaud, C Nuckolls, TF Heinz, and LE Brus. Energy Transfer from Individual Semiconductor Nanocrystals to Graphene. *ACS Nano*, 4(5):2964–2968, 2010. DOI: 10.1021/nn1005107.
- [83]SY Wang, C Querner, T Dadosh, CH Crouch, DS Novikov, and M Drndic. Collective Fluorescence Enhancement in Nanoparticle Clusters. *Nature Communications*, 2, 2011. DOI: 10.1038/ncomms1357.
- [84]S Volkan-Kacso, PA Frantsuzov, and B Janko. Correlations between Subsequent Blinking Events in Single Quantum Dots. *Nano Letters*, 10(8):2761–2765, 2010. DOI: 10.1021/nl100253r.
- [85]D Prasai, AR Klots, AKM Newaz, JS Niezgoda, NJ Orfield, CA Escobar, A Wynn, A Efimov, GK Jennings, SJ Rosenthal, and KI Bolotin. Electrical Control of near-Field Energy Transfer between Quantum Dots and Two-Dimensional Semiconductors. *Nano Letters*, 15(7):4374–4380, 2015. DOI: 10.1021/acs.nanolett.5b00514.
- [86]C Krasselt, J Schuster, and C von Borczyskowski. Photoinduced Hole Trapping in Single

- Semiconductor Quantum Dots at Specific Sites at Silicon Oxide Interfaces. *Physical Chemistry Chemical Physics*, 13(38):17084–17092, 2011. DOI: 10.1039/C1CP22040C.
- [87]JR McBride, TJ Pennycook, SJ Pennycook, and SJ Rosenthal. The Possibility and Implications of Dynamic Nanoparticle Surfaces. *ACS Nano*, 7(10):8358–8365, 2013. DOI: 10.1021/nn403478h.
- [88]J Taylor, T Kippeny, and SJ Rosenthal. Surface Stoichiometry of CdSe Nanocrystals Determined by Rutherford Backscattering Spectroscopy. *Journal of Cluster Science*, 12(4):571–582, 2001. DOI: 10.1023/A:1014246315331.
- [89]P Guyot-Sionnest and MA Hines. Intraband Transitions in Semiconductor Nanocrystals. *Applied Physics Letters*, 72(6):686–688, 1998. DOI: <http://dx.doi.org/10.1063/1.120846>.
- [90]O Voznyy and EH Sargent. Atomistic Model of Fluorescence Intermittency of Colloidal Quantum Dots. *Physical Review Letters*, 112(15), 2014. DOI: <http://dx.doi.org/10.1103/PhysRevLett.112.157401>.
- [91]E Lifshitz, I Dag, ID Litvitn, and G Hodes. Optically Detected Magnetic Resonance Study of Electron/Hole Traps on CdSe Quantum Dot Surfaces. *Journal of Physical Chemistry B*, 102(46):9245–9250, 1998. DOI: 10.1021/jp981880v.
- [92]O Voznyy, SM Thon, AH Ip, and EH Sargent. Dynamic Trap Formation and Elimination in Colloidal Quantum Dots. *Journal of Physical Chemistry Letters*, 4(6):987–992, 2013. DOI: 10.1021/jz400125r.
- [93]TJ Pennycook, JR McBride, SJ Rosenthal, SJ Pennycook, and ST Pantelides. Dynamic Fluctuations in Ultrasmall Nanocrystals Induce White Light Emission. *Nano Letters*, 12(6):3038–3042, 2012. DOI: 10.1021/nl3008727.

- [94]SJ Rosenthal, J McBride, SJ Pennycook, and LC Feldman. Synthesis, Surface Studies, Composition and Structural Characterization of CdSe, Core/Shell and Biologically Active Nanocrystals. *Surface Science Reports*, 62(4):111–157, 2007. DOI: 10.1016/j.surfrep.2007.02.001.
- [95]T Pons, IL Medintz, D Farrell, X Wang, AF Grimes, DS English, L Berti, and H Mattoussi. Single-Molecule Colocalization Studies Shed Light on the Idea of Fully Emitting versus Dark Single Quantum Dots. *Small*, 7(14):2101–2108, 2011. DOI: 10.1002/smll.201100802.
- [96]DV Talapin, R Koeppel, S Gotzinger, A Kornowski, JM Lupton, AL Rogach, O Benson, J Feldmann, and H Weller. Highly Emissive Colloidal CdSe/CdS Heterostructures of Mixed Dimensionality. *Nano Letters*, 3(12):1677–1681, 2003. DOI: 10.1021/nl034815s.
- [97]RG Neuhauser, KT Shimizu, WK Woo, SA Empedocles, and MG Bawendi. Correlation Between Fluorescence Intermittency and Spectral Diffusion in Single Semiconductor Quantum Dots. *Physical Review Letters*, 85(15):3301–3304, 2000. DOI: <http://dx.doi.org/10.1103/PhysRevLett.85.3301>.
- [98]A. Castelli, F. Meinardi, M. Pasini, F. Galeotti, V. Pinchetti, M. Lorenzon, L. Manna, U. Giovanella, I. Moreels, and S. Brovelli. High Efficiency All-Solution-Processed LEDs Based on Anisotropic Colloidal Heterostructures with Polar Polymer Injecting Layers. *Nano Letters*, 15(8):5455–5464, 2015. DOI: 10.1021/acs.nanolett.5b01849.
- [99]C Foucher, B Guilhabert, N Laurand, and MD Dawson. Wavelength-Tunable Colloidal Quantum Dot Laser on Ultra-Thin Flexible Glass. *Applied Physics Letters*, 104(14):141108, 2014. DOI: <http://dx.doi.org/10.1063/1.4871372>.
- [100]YS Park, AV Malko, J Vela, Y Chen, Y Ghosh, F Garcia-Santamaria, JA Hollingsworth, VI Klimov, and H Htoon. Near-Unity Quantum Yields

- of Biexciton Emission from CdSe/CdS Nanocrystals Measured Using Single-Particle Spectroscopy. *Physical Review Letters*, 106(18):187401, 2011. DOI: <http://dx.doi.org/10.1103/PhysRevLett.106.187401>.
- [101]S. J. Rosenthal, J. C. Chang, O. Kovtun, J. R. McBride, and I. D. Tomlinson. Bio-compatible Quantum Dots for Biological Applications. *Chemical Biology*, 18(1):10–24, 2011. DOI: 10.1016/j.chembiol.2010.11.013.
- [102]NJ Orfield, JR McBride, JD Keene, LM Davis, and SJ Rosenthal. Correlation of Atomic Structure and Photoluminescence of the Same Quantum Dot: Pinpointing Surface and Internal Defects That Inhibit Photoluminescence. *ACS Nano*, 9(1):831–839, 2015. DOI: 10.1021/nn506420w.
- [103]B Mahler, P Spinicelli, S Buil, X Quelin, JP Hermier, and B Dubertret. Towards Non-Blinking Colloidal Quantum Dots. *Nature Materials*, 7(8):659–664, 2008. DOI: 10.1038/nmat2222.
- [104]J Vela, H Htoon, YF Chen, YS Park, Y Ghosh, PM Goodwin, JH Werner, NP Wells, JL Casson, and JA Hollingsworth. Effect of Shell Thickness and Composition on Blinking Suppression and the Blinking Mechanism in ‘Giant’ CdSe/CdS Nanocrystal Quantum Dots. *Journal of Biophotonics*, 3(10-11):706–717, 2010. DOI: 10.1002/jbio.201000058.
- [105]C Galland, Y Ghosh, A Steinbruck, JA Hollingsworth, H Htoon, and VI Klimov. Lifetime Blinking in Nonblinking Nanocrystal Quantum Dots. *Nature Communications*, 3(908), 2012. DOI: 10.1038/ncomms1916.
- [106]CA Leatherdale, WK Woo, FV Mikulec, and MG Bawendi. On the Absorption Cross Section of CdSe Nanocrystal Quantum Dots. *Journal of Physical Chemistry B*, 106(31):7619–7622, 2002. DOI: 10.1021/jp025698c.

- [107]ZW Wang, ZY Li, SJ Park, A Abdela, D Tang, and RE Palmer. Quantitative Z-Contrast Imaging in the Scanning Transmission Electron Microscope with Size-Selected Clusters. *Physical Review B*, 84(7):073408, 2011. DOI: <http://dx.doi.org/10.1103/PhysRevB.84.073408>.
- [108]J. M. LeBeau, S. D. Findlay, L. J. Allen, and S. Stemmer. Quantitative Atomic Resolution Scanning Transmission Electron Microscopy. *Physical Review Letters*, 100(20):206101, 2008. DOI: <http://dx.doi.org/10.1103/PhysRevLett.100.206101>.
- [109]M Paulite, KP Acharya, HM Nguyen, JA Hollingsworth, and H Htoon. Inverting Asymmetric Confinement Potentials in Core/Thick-Shell Nanocrystals. *Journal of Physical Chemistry Letters*, 6(4):706–711, 2015. DOI: 10.1021/jz5027163.
- [110]DF Underwood, T Kippeny, and SJ Rosenthal. Ultrafast Carrier Dynamics in CdSe Nanocrystals Determined by Femtosecond Fluorescence Upconversion Spectroscopy. *Journal of Physical Chemistry B*, 105(2):436–443, 2001. DOI: 10.1021/jp003088b.
- [111]AH Ip, SM Thon, S Hoogland, O Voznyy, D Zhitomirsky, R Debnath, L Levina, LR Rollny, GH Carey, A Fischer, KW Kemp, IJ Kramer, ZJ Ning, AJ Labelle, KW Chou, A Amassian, and EH Sargent. Hybrid Passivated Colloidal Quantum Dot Solids. *Nature Nanotechnology*, 7(9):577–582, 2012. DOI: 10.1038/nnano.2012.127.
- [112]DE Chang, AS Sorensen, EA Demler, and MD Lukin. A Single-Photon Transistor Using Nanoscale Surface Plasmons. *Nature Physics*, 3(11):807–812, 2007. DOI: 10.1038/nphys708.
- [113]IC Hoi, CM Wilson, G Johansson, T Palomaki, B Peropadre, and P Delsing. Demonstration of a Single-Photon Router in the Microwave Regime. *Physical Review Letters*, 107(7), 2011. DOI: <http://dx.doi.org/10.1103/PhysRevLett.107.073601>.
- [114]M Bayer, P Hawrylak, K Hinzer, S Fafard, M Korkusinski, ZR Wasilewski, O Stern,

- and A Forchel. Coupling and Entangling of Quantum States in Quantum Dot Molecules. *Science*, 291(5503):451–453, 2001. DOI: 10.1126/science.291.5503.451.
- [115]O Chen, J Zhao, VP Chauhan, J Cui, C Wong, DK Harris, H Wei, HS Han, D Fukumura, RK Jain, and MG Bawendi. Compact High-Quality CdSe-CdS Core-Shell Nanocrystals with Narrow Emission Linewidths and Suppressed Blinking. *Nature Materials*, 12(5):445–451, 2013. DOI: 10.1038/nmat3539.
- [116]MA Harrison, A Ng, AB Hmelo, and SJ Rosenthal. CdSSe Nanocrystals with Induced Chemical Composition Gradients. *Israeli Journal of Chemistry*, 52(11-12):1063–1072, 2012. DOI: 10.1002/ijch.201200040.
- [117]B Mahler, N Lequeux, and B Dubertret. Ligand-Controlled Polytypism of Thick-Shell CdSe/CdS Nanocrystals. *Journal of the American Chemical Society*, 132(3):953–959, 2010. DOI: 10.1021/ja9034973.
- [118]WW Yu, LH Qu, WZ Guo, and XG Peng. Experimental Determination of the Extinction Coefficient of CdTe, CdSe, and CdS Nanocrystals. *Chemistry of Materials*, 15(14):2854–2860, 2003. DOI: 10.1021/cm034081k.
- [119]M Nasilowski, P Spinicelli, G Patriarche, and B Dubertret. Gradient CdSe/CdS Quantum Dots with Room Temperature Biexciton Unity Quantum Yield. *Nano Letters*, 15(6):3953–3958, 2015. DOI: 10.1021/acs.nanolett.5b00838.
- [120]M Yorulmaz, S Nizzero, A Hoggard, LY Wang, YY Cai, MN Su, WS Chang, and S Link. Single-Particle Absorption Spectroscopy by Photothermal Contrast. *Nano Letters*, 15(5):3041–3047, 2015. DOI: 10.1021/nl504992h.
- [121]DV Talapin, JS Lee, MV Kovalenko, and EV Shevchenko. Prospects of Colloidal Nanocrystals for Electronic and Optoelectronic Applications. *Chemical Reviews*, 110(1):389–458, 2010. DOI: 10.1021/cr900137k.